Semiconductor Laser Wind Lidar for Turbine Control

Hu, Qi

Publication date:
2016

Document Version
Publisher's PDF, also known as Version of record

Technical University of Denmark

DTU Fotonik
Department of Photonics Engineering

Semiconductor Laser Wind Lidar for Turbine Control

Qi Hu

Ph.D. Thesis, March 2016

WINDAR PHOTONICS

Summary

This thesis describes an experimentally oriented study of continuous wave (CW) coherent Doppler lidar system design. The main application is remote wind sensing for active wind turbine control using nacelle mounted lidar systems; and the primary focus is to devise an industrial instrument that can improve the efficiency of harvesting wind energy in commercial wind farms. This work attempts to provide a complete investigation of all the necessary building blocks in a CW wind lidar, from the light source to the optical transceiver.

The basic concept of Doppler lidar is introduced along with a brief historical overview within the topic of wind lidar systems. Both the potential and the challenges of an industrialized wind lidar has been addressed here. Furthermore, the basic concept behind the heterodyne detection and a brief overview of the lidar signal processing is explained; and a simple representation of the system signal-to-noise ratio (SNR), including the most common and relevant noise sources, is formulated.

The impact of various system parameters, such as insertion loss, backscatter coefficient and transceiver telescope design, on the total signal power is discussed and analysed. A thorough investigation of the telescope truncation and lens aberrations is conducted, both numerically and experimentally. It is shown that these parameters dictate the spatial resolution of the lidar system, and have profound impact on the SNR.

In this work, an all-semiconductor light source is used in the lidar design instead of the conventional fiber-lasers. Besides its advantage of lower cost, the relative intensity noise, which peaks around 1 MHz for fiber lasers, is inherently avoided by using a semiconductor light source. The impact of the linewidth increment on the SNR in the application of wind measurement has been investigated. The result shows a much less SNR penalty than expected, due to a finite signal bandwidth of the wind signal.

For applications such as active yaw or pitch control, multiple lines of sight are required of the lidar system. Thus, two different beam steering methods have been investigated and demonstrated in this work. The challenge, aside from cost and compactness, is to ensure a long lifetime without regular maintenance, since the wind turbines are designed to last for 20 years.

Finally, field test results of various measurement campaigns, designed to evaluate our lidar design, are presented here. Our design has been compared with both sonic anemometers and a conventional fiber laser based CW wind lidar. The results show no significant performance difference between the systems in terms of determining the wind speed of the measurement volume.

Resume(Dansk)

Denne eksperimentelt orienterede afhandling beskriver en undersøgelse af et CW kohærent Doppler lidar design. Hovedapplikationen er fjernmålinger af vind til aktiv krøjningskontrol af vindmøller ved hjælp af nacelle monteret lidarsystemer. Det primære fokus er at designe et industrielt instrument til at forbedre udnyttelsesgraden af vindressourcer i kommercielle vindmølleparker. Denne rapport forsøger at levere en komplet beskrivelse af alle de nødvendige byggesten, fra lyskilden til den optiske transceiver, af en CW vind lidar.

Det grundlæggende koncept for en Doppler lidar introduceres sammen med en kort historisk oversigt inden for udviklingen af vind-lidar-systemer. Endvidere bliver det grundlæggende koncept bag heterodyn detektion og en kort oversigt over lidar signalbehandling forklaret. En simpel matematisk repræsentation af systemets signal-støj forhold (SNR) formuleres, og den inkluderer alle de relevante støjkilder i vores system.

Påvirkningen af den samlede signal styrke grundet optisk tab, tilbagespredningen og transceiver teleskop design, er blevet diskuteret og analyseret. En grundig undersøgelse af teleskop afskæring af den udadgående lys og linseaberrationer, blev foretaget både numerisk og eksperimentelt. Det er påvist, at de afgør den rumlige opløsning af lidar systemet, og dermed har en signifikant påvirkning på SNR.

I dette projekt, anvendes en halvleder lyskilde i stedet for de konventionelle fiber-lasere. Udover dens lavere pris, bliver en halvleder lyskilde heller ikke udsat for relative intensitet støj, som i fiber lasere. Påvirkningen af SNR pga. en øget laser linjebredde er blevet grundigt undersøgt mht. applikationen for vindmølle krøjningskontrol. Resultatet viser en væsentlig mildere forværring af SNR end ventet pga. vindsignal båndbredde.

Vi har demonstreret hvordan vores lidar design kan have flere måle retninger for at identificere vindvektoren i flere dimensioner. Den største udfordring er at sikre en lang levetid uden behov for regelmæssig vedligeholdelser, da lidar systemet skal være monteret på vindmøller, der har en livstid på 20 år. Vores lidar design er blevet evalueret i forskellige målekampagner, hvor den bliver sammenlignet med bl.a. soniske anemometre og en fiber-laser baseret CW vind lidar. Resultaterne viser ingen signifikant forskel mellem disse systemer og vores design, når det gælder bestemmelser af vindhastigheder.

Preface

This thesis presents the results of an industrial Ph.D study from March 2013 to March 2016. The Ph.D project was a collaboration between the Department of Photonics Engineering (DTU Fotonik) of the Technical University at Denmark and my host company Windar Photonics A/S. The project was funded by Windar Photonics A/S and the Danish Innovation Foundation (InnovationsFonden). The experimental work was carried out in the laboratory facilities of the Optical Sensor Technology Group and outdoor facilities of the Department of Wind Energy (DTU Wind Energy) sited at DTU Risoe Campus. DTU Wind Energy is a third part collaborator that evaluates our lidar system based on wind measurements.

This thesis represents my original work unless other is stated, and the content consists of a mixture of published and unpublished work. The Ph.d project is continuation of the research of my supervisors Christian Pedersen and Peter John Rodrigo in the topic of *all semiconductor laser coherent lidar system*. Some specific design parameters and detailed system descriptions have been omitted in this thesis, since they are considered as sensitive materials for Windar Phtotonics.

An external research stay took place at National Oceanic and Atmospheric Administration (NOAA), Boulder, Colorado, US, from October 21st to December 21st, 2014.

Acknowledgements

First of all, I would like to thank both my university supervisors, Christian Pedersen and Peter John Rodrigo, for their great support and guidance. I have never made this far without Christians strategic overview and Peters great expertise; discussions with them often led to great breakthroughs in the project. From the Optical Sensor Technology Group, I will like to thank my friend and colleague, Lasse Høgstedt, for many useful discussions throughout the project and a thorough proofreading; Finn A. C. Pedersen for his technical support; and Peter Tidemand-Lichtenberg for our discussions in fundamental laser physics.

From Windar Photonics, I will like to thank my CTO and company supervisor Jørgen Korsgaard Jensen for providing me with the necessary support and guidance, and Antoine Larval for his support in some of the measurement campaigns. Furthermore, I will like to thank Ebba Dellwik, Jakob Mann, and Mikael Sjöholm from the Department of Wind Energy for granting me the access to their outdoor measurement facilities and for their collaboration in some of the measurement campaigns. From NOAA, I will like to thank Alan Brewer and his team for hosting my stay at NOAA; it was a very unique experience. Finally, I will like to thank Windar Photonics A/S and Innovationsfonden for the financial support.

Qi Hu, March 2016

List of Publications

Journal Papers

1. **Investigation of spherical aberration effects on coherent lidar performance**
   Q. Hu, P. J. Rodrigo, T. F. Q. Iversen, and C. Pedersen
   Optics Express **21**, 22, pages: 25670-25676 (2013)

2. **Diode laser lidar wind velocity sensor using a liquid-crystal retarder for non-mechanical beam-steering**
   P. J. Rodrigo, T. F. Q. Iversen, Q. Hu, and C. Pedersen
   Optics Express, **22**, 22, 26674-26679 (2014)

3. **Remote wind sensing with a CW diode laser lidar beyond the coherence regime**
   Q. Hu, P. J. Rodrigo, and C, Pedersen
   Optics Letters, **39**, 16, 4875-4878 (2014)

4. **Eye-safe diode laser Doppler lidar with a MEMS beam-scanner**
   Q. Hu, C. Pedersen and P. J. Rodrigo
   Optics Express, **24**, 3, 1934-1942 (2016)

Conference Proceedings

1. **Field test of an all-semiconductor laser-based coherent continuous-wave Doppler lidar for wind energy applications**
   M. Sjöholm, E. Dellwik, Q. Hu, J. Mann, C Pedersen, and P. J. Rodrigo
   17th International Symposium for the Advancement of Boundary-Layer Remote Sensing (ISARS), (2014)

2. **Semiconductor Laser Lidar Wind Velocity Sensor for Turbine Control**
   P. J. Rodrigo, Q. Hu, and C. Pedersen
   Proceedings of Optical Instrumentation for Energy and Environmental Applications. ISBN: 978-1-55752-756-1 (2014)

3. **Impact of primary aberrations on coherent lidar performance**
   Q. Hu, P. J. Rodrigo, T. F. Q. Iversen, and C. Pedersen
   Proceedings of SPIE, the International Society for Optical Engineering, **8992**, 89920T (2014)

4. **Effects of 1/f frequency noise in self-heterodyne linewidth measurement system with various delay lengths**
   Q. Hu, P. J. Rodrigo, and C. Pedersen
   The European Conference on Lasers and Electro-Optics, CH_P_34 (2015)

5. **Development of semiconductor laser based Doppler lidars for wind-sensing applications**
   P. J. Rodrigo, Q. HU, and C. Pedersen
   Proceedings of 2015 IEEE Region 10 Humanitarian Technology Conference, IEEE, pp. 1-4 (2015)

Patents

1. **LIDAR based on MEMS**
   J. K. Jensen, Q. Hu, P. J. Rodrigo, and C, Pedersen

2. **Eye-safe LIDAR system based on MEMS**
   J. K. Jensen, Q. Hu, P. J. Rodrigo, and C, Pedersen

Unrelated Publications

1. **High resolution mid-infrared spectroscopy based on frequency up-conversion**
   J. S. Dam, Q. Hu, P. Tidemand-Lichtenberg, and C. Pedersen
   Proceedings of SPIE, the International Society for Optical Engineering. **8604**, 86040S (2013).

2. **Non-collinear upconversion of infrared light**
   C. Pedersen, Q. Hu, L. Høgstedt, P. Tidemand-Lichtenberg, and J. S. Dam
   Optics Express, **22**, 23, 28027-28036 (2014)

3. **Non-collinear upconversion of incoherent light: designing infrared spectrometers and imaging systems**
   J, S. Dam, Q. Hu, C. Pedersen, and P. Tidemand-Lichtenberg
   Proceedings of SPIE, the International Society for Optical Engineering, **8964**, 89640F (2014)

Contents

List of Publications **i**
Journal Papers i
Conference Proceedings i
Patents ii
Unrelated Publications ii

1 Introduction **1**
1.1 Motivation 1
1.2 Historical Overview 2
1.3 Doppler Lidar Operation Concept 2
1.4 Project Scope 5
1.5 Thesis Structure 6

2 Detection Concept and Noise Sources **7**
2.1 Heterodyne Detection 7
2.2 Noise Sources in CDL 8
2.2.1 Shot Noise Limited Detection 8
2.2.2 Relative Intensity Noise 9
2.2.3 Phase Noise from Stray Light 12

3 Lidar Signal **15**
3.1 Lidar Signal Power 15
3.2 Probing Volume Confinement 17
3.3 Investigation of Spherical Aberration Effects on Coherent Lidar Performance 18
3.4 Astigmatism and Monostatic Condition 25

4 Light source **27**
4.1 PIIN Suppression 27
4.2 Linewidth Measurement 28
4.3 Remote Wind Sensing With a CW Diode Laser Lidar Beyond the Coherence Regime 30
4.4 Spectral Content of Lidar Signal 38

5 Multi-Beam Steering **41**
5.1 Liquid Crystal Retarder 41
5.2 MEMS Scanning Mirror 44

5.3 Eye-safe Diode Laser Doppler Lidar With a MEMS Beam-scanner . . 45
5.4 Wind Signal during Dithering 54

6 Field Tests **57**
6.1 Sonic Anemometers vs. WindEye 57
6.2 WindEye vs. Windscanner R2D1 60
6.3 SNR as Function of Focus Distance 62
6.4 Yaw Misalignment Correction Using WindEye 65

7 Conclusion **67**

Bibliography **69**

A List of Abbreviations **75**

B WindEye Description **77**

C Conference Slides from ISARS 2014 **95**

1 Introduction

1.1 Motivation

In the past decades, it became apparent that the increasing power consumption on the globe makes it unviable to rely solely on the traditional fossil fuels. Thus, a wide range of initiatives were undertaken in the pursuit of more sustainable energy sources. Wind energy stood out as one of the most promising renewable energy sources. As a result, massive investments in this research topic were made across the globe.

In the recent years, the wind industry has expanded rapidly despite its technological immaturity, e.g., the wind farm operations are far from perfect. According to Global Wind Energy Council (GWEC) 3.0% of the world power production comes from wind energy in 2014, and this number can grow up to $17\% - 19\%$ in 2030 [1]. This shows the great potential of research and optimization within the field.

So far 90% of the research within the wind industry are focused on the power electronics engineering [2], but as part of the technological maturation, more focus is now turned to the mechanical/aerodynamic part to havest the wind energy more efficiently, which involves both proper siting for wind farms and active turbine control (yaw and pitch). Both initiatives require extensive knowledge of the ambient wind profile on the site. Every turbine is equipped with either cup or sonic anemometer (some times both) on top of the nacelle to provide the speed and direction of the ambient wind. However, these sensors are mounted in the turbulent zone right behind the rotor blades, making the measurement inaccurate [3]. Thus, for accurate wind profiling meteorological masts (commonly known as *met-masts*) at hub height are often used. For active turbine control, one or more met-masts are placed in front of the intended turbine. While this method is quite reliable, it becomes extremely costly for individual turbine control in a wind farm, since a plurality of met-masts are likely required. And even for research purposes, many fear that the mast height will exceed the mechanical and cost limits in the future, as the size of new turbine models grows every year. As a result, the wind industry shows a growing interest towards laser radar (lidar) system. Traditionally, this technique was only used in military applications and atmospheric research due to its high cost and complexity. But in recent years, the maturation of the wind lidar technology has made it feasible for even industrial use.

1.2 Historical Overview

Historically, the concept of coherent Doppler lidar (CDL) was already described by Biernson and Lucy [4] shortly after the invention of laser. The earliest works on lidar technology uses either HeNe laser or ruby laser as the light source [5–7] and these experiments were usually conducted in controlled flow pipes. Since the invention of CO_2 laser in 1964 [8], it became the preferred light source for coherent lidar applications. The CO_2 laser provides a stable high-power single frequency output with reasonable efficiency, operations in both CW and pulsed regime, reasonable atmospheric transmission, and eye safety. The first atmospheric wind measurement using a CO_2 laser was reported by Huffaker [9].

As a result of the availability of high-power diode lasers in the mid-80's, diode-pumped solid state lidar systems became a viable alternative to CO_2 lidars. These systems offered great improvements in efficiency, compactness and lifetime compared to CO_2 light sources. The first description of a 1.06 μm CDL using Nd:YAG laser was reported by Kane et al. [10] in 1985. However, the widespread use of 1.06 μm was hampered due to eye-safety issues. As a result, diode-pumped 2.01 μm CDL systems, firstly reported by Suni and Henderson [11] in 1991, were deployed much more frequently.

More recently, CDL system operating at 1.5 μm was demonstrated. The light source can either be of bulk design or erbium doped glass fiber laser. While the fiber design limits its power output due to Brillouin scattering and material damage, it holds the advantage of simple assembly, easy alignment and high compactness. The main motivation for switching to 1.5 μm systems was to increase the efficiency and reduce the cost by accessing the well-developed components in the telecom industry. The first all-fiber CDL was demonstrated by Karlsson et al. [12], where the light source was a combination of a semiconductor laser seed, and an Erbium doped fiber amplifier (EDFA). However, the excess noise was too high due to the relatively large linewidth of the semi-conductor laser seed. As a consequence, most all-fiber CDL systems rely on fiber lasers as the seed today [13, 14], since they have superior linewidth performance compared to semiconductor lasers. (For a more complete historical overview up to year 2005, see [15] pp.475-479)

1.3 Doppler Lidar Operation Concept

The wind lidar technology relies on detecting backscattered light from moving aerosols in the atmosphere, when illuminated by laser radiation. By measuring the Doppler frequency shift of the backscattered light, the wind speed can determined remotely. The basic concept can be illustrated as in Fig. 1.1. The radial speed component of the target, V_{LOS} can be determined from the Doppler shift of the back scattered light using the expression

$$\nu_d = \frac{2V_{\mathrm{LOS}}}{\lambda} \tag{1.1}$$

where ν_d is the Doppler shift, and λ is the laser wavelength. Figure 1.1 sketches a CDL system, where the local oscillator (LO) is essential for sensitive operation. Firstly, it provides a stable frequency reference, allowing precise velocity measurement; as a result, CDL systems are inherently calibrated. The LO also amplifies the Doppler signal through parametric down conversion, increasing the sensitivity significantly. Finally, the coherent property of a laser light source makes the CDL completely immune to background noise from ambient lights (e.g., sunlight). These useful properties will be described in details in Chapter 2.

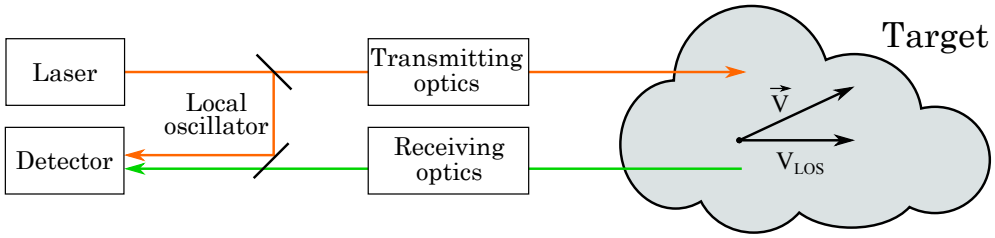

Figure 1.1: *Generic Doppler lidar concept where* $\boldsymbol{V}$ *is the mean velocity of the target, and* V_{LOS} *is projected radial wind speed.*

The generic set-up shown in figure 1.1 is a *bistatic* system defined by having separated transmitter/receiver optics. In this configuration, the measurement volume is confined by the spatial overlap between the intersecting field-of-view. While it is an excellent method to improve the spatial resolution, the total signal return from the aerosols is reduced, since the backscattered light outside the field-of-view overlap are not detected. This trade-off has to be taken into consideration when designing a bistatic system.

When the receiver and transmitter share the same telescope, the system is called *monostatic*. Due to its simplicity and good performance over extended ranges, it is often chosen over the bistatic design, except in applications where unwanted transmitter feedback and interference pose a serious problem, or a particularly high spatial resolution at relatively long probe distance is needed.

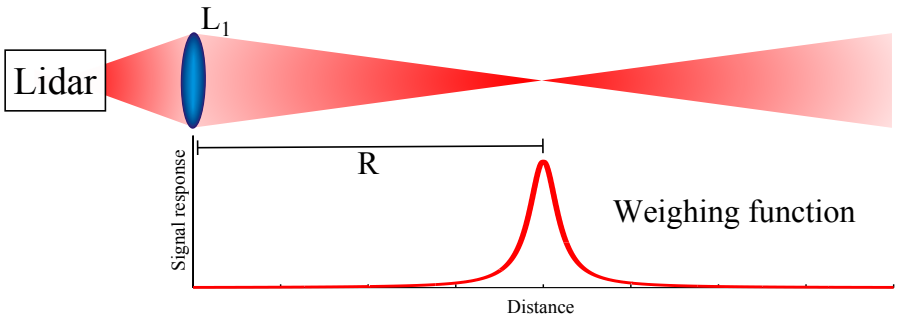

Figure 1.2: *The relation between the weighting function and the lidar output beam, assuming a perfect Gaussian beam and monostatic condition.* L_1 *is the last lens in the transmitting telescope.*

The CDL system can either be of pulsed or CW type. In a CW system, the probe volume is determined by its focusing optics. The signal response is distance dependent along the beam propagation. Assuming a perfect Gaussian beam and monostatic condition, the *(spatial) weighting function* of the system, has a Lorentzian shape and peaks at the beam waist [16]. The spatial resolution of such a system, *the probe length*, is defined as the full width half maximum (FWHM) of the weighting function and corresponds usually to twice the Rayleigh length. The probe range, R is defined as the distance between the instrument and the peak of the weighting function, see Fig. 1.2. CW systems have an inherent maximum probe range due to diffraction and finite telescope exit lens diameter. Typically, the probe range cannot exceed a few hundred meters.

In pulsed lidars, even though radiation is emitted in short bursts (typically in the order of 100 ns), the LO remains CW. This permits range measurement based on time of flight. Thus, different range bins can be obtain in parallel, while active focus adjustment is necessary for probing different ranges in CW systems. Instead of being defined by the focusing geometry, pulsed systems use the pulse width to control the spatial resolution; hence the transmitted beam is usually collimated, allowing a measurement range up to several kms. In general, CW systems have superior spatial resolution for short range applications (e.g., <100 m), but as the probing range increases, pulsed systems are preferable despite its slightly more complicated design.

Direct Detection

There is also a wind lidar technique called direct detection where the LO is not needed. Without the enhanced sensitivity resulting from the signal amplification by the LO, direct detection systems have to rely on low noise, high quantum efficiency detectors. Thus, they often operate in the visible or UV wavelength region. Direct detection systems can be either monostatic or bistatic, and the light source can be CW or pulsed. In the visible or in the even UV wavelength regime, atmospheric backscattering from aerosol (Mie) and air molecules (Rayleigh) becomes comparable. As a results, the direct detection technique is usually used in applications where the aerosol concentration is very low, for instances when measuring in the stratosphere.

CDL Signal Processing

The basic concept of Doppler lidar signal processing is illustrated in Fig. 1.3. Physically, the detector measures the optical power fluctuations as a function of time. Due to the high DC power level (LO), the detector is usually AC coupled – the detector signal output only contains the AC components. The power spectral density (PSD), containing the Doppler information, is acquired through *Fast Fourier Transform* (FFT) of the detector signal. Averaging of multiple spectra is often needed before the Doppler peak appears distinguishable from noise. The radial speed can now be determined via for instance a peak finding algorithm.

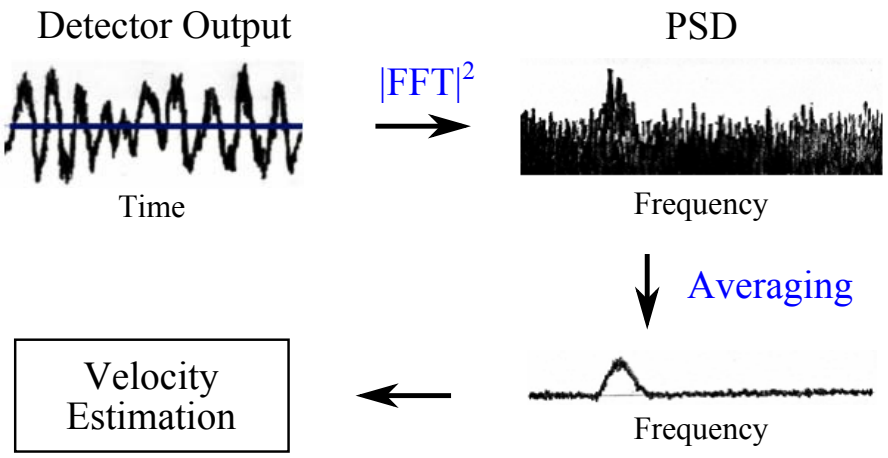

Figure 1.3: *Outline of lidar wind signal process, the detector output is in voltage, $v(t)$, which is proportional to the detector current, $i(t)$. This figure is adapted from [17].*

1.4 Project Scope

In an effort to make wind lidars more applicable for mass-production and broad industrial use, collaboration between Windar Photonics A/S and DTU Fotonik in 2008 led to the first demonstration of a low-cost, compact wind lidar based on an all semiconductor laser source [18]. The first successful field deployment of such system was demonstrated by the same group in 2012 [19]. This project can be considered as a continuation of the work presented in [18, 19], and is dedicated to investigate different possibilities when designing a low-cost nacelle mounted wind lidar. The instrument is intended for individual turbine yaw control (maybe even blade pitch control) in the wind industry.

The active yaw control of the turbine rotor ensures its alignment with the wind. Usually, the yaw control relies on a nacelle mounted wind vane as feedback sensor, and is of a "on-off" nature with discrete motions. It occurs that the wind direction change happens more frequent than the yaw control response time (10 min). Theoretically, the performance could be improved by a faster yaw control, but it will cause significant wear on the system, making the solution rather impractical. A second source of yaw errors is caused by the inaccuracy of the nacelle mounted wind vane. This problem can, however, be addressed using a more accurate wind sensor. Different studies suggest that a nacelle mounted lidar could be a good alternative [20]. In a recent study, Wan et al. [21] (2015) claims that 13.3% of wind turbines down time are caused by the yaw failures, while the failure rate of the yaw system itself is 12.5%. This shows the potential of a proper lidar assisted yaw control.

In wind turbine control applications, the probe distance is fixed and is expected to be less than 100 m. In this case, it is most advantageous to use a monostatic CW CDL; since it can obtain a relatively high spatial resolution under these conditions and has a far simpler design than a bistatic and/or pulsed system. Thus, the inves-

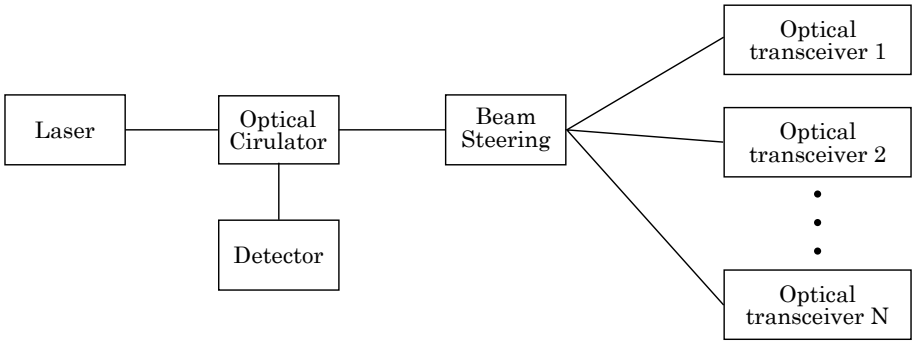

Figure 1.4: *A generic lidar design layout with multiple optical transceivers.*

tigations in this work focus on the monostatic CW configuration. The basic layout of such a system is shown in Fig. 1.4, where the optical circulator combines the LO and the backscatter signal, and the transceivers provide multiple measurement points to produce a 3D wind vector necessary for yaw and pitch control.

1.5 Thesis Structure

In Chapter 2, the heterodyne detection concept is explained, and a simple formulation of the signal to noise ratio (SNR) including the most relevant noise sources is described. Chapter 3 addresses the lidar signal dependence of different system parameters, and relate them directly to the SNR. In Chapter 4, the performance impact of the light source linewidth and stability is investigated. Application and design requirements of the beam steering section – one based on a liquid-crystal (LC) device and the other based on micro-electromechanical systems (MEMS) device – used for active yaw and pitch control are discussed in Chapter 5. Field tests of our lidar designs including system comparison with other anemometers and actual turbine control applications are presented in Chapter 6. Finally, the obtained results in this work is summarized and discussed in Chapter 7.

2 Detection Concept and Noise Sources

In this chapter, the basic concept of heterodyne detection is described and a mathematical representation of the sensitivity of CW CDL system is established. For optimum sensitivity, the noise level should be dominated by the shot noise originated from the LO. This can be hampered by the presence of both the excess intensity noise and the phase noise. The main cause and impact of these unwanted noises will be presented here, along with the expression of the SNR including all these noise source terms.

2.1 Heterodyne Detection

As mentioned in the previous chapter, the coherent Doppler lidar concept relies on the heterodyne beating between the LO and the atmospheric return. In this section, a simple mathematical representation is used to illustrate the physical principle behind the heterodyne detection. Two optical fields E_1 and E_2 can represented as

$$E_1 = A_1 \cos(\omega_1 t), \qquad E_2 = A_2 \cos(\omega_2 t + \phi(t)) \tag{2.1}$$

where A_i is the field amplitude, ω_i is the angular frequency, ϕ is the relative phase difference and t is time. Assuming complete spatial overlap between E_1 and E_2. The resulting intensity of the combined fields are given by:

$$\begin{aligned} I &= \tfrac{1}{2} n c \epsilon_0 (E_1 + E_2)(E_1 + E_2)^* \qquad \Rightarrow \\ I &\propto \left[A_1 \cos(\omega_1 t) + A_2 \cos(\omega_2 t + \phi(t))\right]^2 \\ &= \tfrac{1}{2}\left[A_1^2 + A_2^2\right] + A_1 A_2 \cos\left[(\omega_2 - \omega_1)t + \phi(t)\right] \\ &+ \underbrace{A_1 A_2 \cos\left[(\omega_1 + \omega_2)t + \phi(t)\right] + \tfrac{1}{2} A_2^2 \cos(2\omega_2 t + 2\phi(t)) + \tfrac{1}{2} A_1^2 \cos(2\omega_1 t)}_{\text{high frequency component}} \end{aligned} \tag{2.2}$$

In the expression above, the first term is the DC signal, the second term is the beating signal between the two fields, while the remaining terms are the high frequency components that can be disregarded. In real detection systems, these (optical) frequency components are not detectable due to limited detector bandwidth. Hence, the detector output current, i(t), generated by an incident intensity given by Eq. (2.2) is

$$i(t) \propto \tfrac{1}{2}\left[A_1^2 + A_2^2\right] + A_1 A_2 \cos\left[(\omega_2 - \omega_1)t + \phi(t)\right]. \tag{2.3}$$

It is apparent from eq. (2.3) that if the phase difference, $\phi(t)$, is constant in time (coherent case), the beating term will have a finite amplitude $A_1 A_2$, and a parametric amplification of either A_1 or A_2 occurs. In the incoherent case, the phase difference, $\phi(t)$, varies rapidly between 0 and 2π in a random fashion. In this limit, PSD of the beating signal are extremely broadband and becomes part of the noise floor.

2.2 Noise Sources in CDL

In the context of a Doppler lidar, E_1 and E_2 can be considered as the local oscillator field, E_{LO}, and the atmospheric signal field, E_s, respectively, and $|E_{\mathrm{LO}}| \gg |E_s|$. In this case, the beating frequency $\omega_2 - \omega_1$ corresponds exactly to the Doppler shift from the aerosols. The fact, that the LO is incoherent with the ambient light sources, their beating signal is broad-banded and will be part of the system noise floor. However, due to the narrow signal bandwidth, the noise contribution from the ambient light is usually many orders of magnitude lower than the LO shot noise, hence it can ignored. In this section, a mathematical representation of the SNR in a CDL system will be formulated, and all the primary noise terms are included here. This formulation illustrates why CDL systems can obtain near shot noised limited sensitivity due to the presence of the LO.

2.2.1 Shot Noise Limited Detection

Assuming square law detection, which is true for all optical detectors when operating in the linear response regime of the detector, the signal power in units of [V^2] is [22]

$$\text{signal} = 2\rho_0^2 P_{\mathrm{LO}} P_s R_e^2 \tag{2.4}$$

where ρ_0 is the responsivity, R_e is the effective detector resistance, P_{LO} is the optical power of the LO, and P_s is the optical power of the backscatter signal. Note the signal only contains the beating term from eq. (2.3), since only the AC coupled detector signal is relevant here.

The noise contributions can be divided in two independent terms: shot noise from LO, N_{LO} and the dark noise N_{dark}. The dark noise includes both the Johnson noise and the electronic noise from the detector circuit. The total noise is then

$$N = N_{\mathrm{LO}} + N_{dark}, \quad N_{\mathrm{LO}} = 2eB\rho_0 P_{\mathrm{LO}} R_e^2 \tag{2.5}$$

where B is the signal bandwidth, and e is the electron charge (the expression of N_{LO} is from [22]). The SNR is then

$$\mathrm{SNR} = \frac{\rho_0^2 P_{\mathrm{LO}} P_s}{eB\rho_0 P_{\mathrm{LO}} + S_{dark}\frac{B}{2R_e^2}} \tag{2.6}$$

where S_{dark} is the PSD of the dark noise in unit of [V^2/Hz], and usually is a constant. Thus, the SNR increases with P_{LO} and when the LO shot noise becomes much larger

than the dark noise, the SNR becomes:

$$\mathrm{SNR} = \frac{\rho_0 P_s}{eB}, \qquad \text{for} \quad eB\rho_0 P_{\mathrm{LO}} \gg S_{dark}\frac{B}{2R_e^2} \tag{2.7}$$

Expression (2.6) is a highly idealized description. In practice, the detector response deviates from linearity or saturates as the LO power increases, creating an optimum operation point of LO power unique for each individual detector. A detailed mathematical description of the effective heterodyne responsivity was presented by Holmes and Rask [22], which is an excellent guideline for detector selection, once the optical layout is decided. Instead of measuring the detector responsivity, ρ_0 and apply it in the model, as carried out in [22], it is more advantageous to measure the SNR directly. Figure 2.1 sketches the set-up to measure the optimal operation point of the LO power. By measuring the SNR as function of the LO power, this method also includes noise terms that are not included in [22], e.g., electronic noise from any control circuits or an impure LO that carries some excess noise.

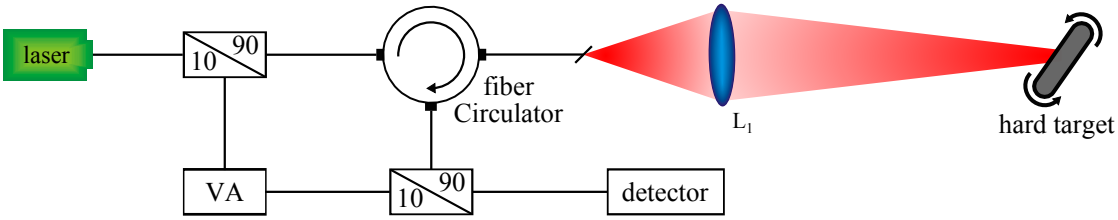

Figure 2.1: *Measurement set-up for optimal LO power, unique for each individual detector, in heterodyne detection. The two 90/10 couplers are configured such that max 1% of the laser light can reach the detector as the LO, and its strength can be further suppressed by the variable attenuator (VA).*

The optimum LO power level is usually around 1 mW, but the SNR value is highly dependent on the non-linearity of the detector response. The optimum P_{LO} of our detector was characterized using the set-up shown in Fig. 2.1, and the result is presented in Fig. 2.2. The SNR peaks around a LO power of 0.4 mW, but the curve stays relatively flat afterwards. This suggests a nearly linear detector response in the measured LO power range; and it allows a relatively large operational interval of the LO power ($0.4 - 1.2$ mW). This allowance is very convenient in real system design, since accurately tapping the LO in these power levels could be a challenge.

2.2.2 Relative Intensity Noise

Every light source suffers from output power fluctuations due to gain fluctuation, cavity instability, and/or noise transfer from the pump source, and the oscillation frequency of steady state power fluctuation is called the *relaxation oscillation frequency*, ν_R. The relative intensity noise (RIN) is defined as the power of intensity

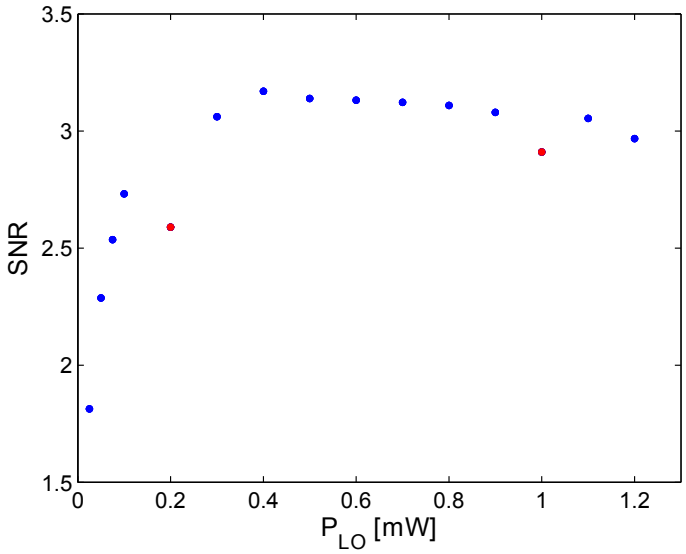

Figure 2.2: *The measured SNR as a function of the LO power of our detector using the set-up shown in Fig. 2.1. The two outliers in the data series are marked as the red dots.*

fluctuations relative to the power of the average intensity. This noise term is important in the context of CDL, since the frequency contents of RIN often overlaps with the radio frequency (RF) of interest. Although most of the RIN sources can be suppressed down to the shot noise limit through careful system design, a RIN spectrum peak at the relaxation oscillation frequency ν_R of the light source is inevitable. Usually, the light sources in CDL system have a relatively narrow bandwidth. Thus, the RIN spectrum is dominated by the relaxation oscillation peak and is shot-noise limited otherwise. The excess intensity noise, N_{ex} due to RIN can be expressed as:

$$N_{ex} = \int_{\nu - B/2}^{\nu + B/2} \rho_0^2 P_{\mathrm{LO}}^2 S_{rin}(\nu') R_e^2 \, \mathrm{d}\nu' \tag{2.8}$$

where ν is the frequency, and $S_{rin}(\nu)$ is the PSD of the RIN in the frequency domain. For relatively narrow signal bandwidth, B, the expression can be reduced to $N_{ex} = B\rho_0^2 P_{\mathrm{LO}}^2 S_{rin}(\nu) R_e^2$ [23]. Recalling Eq. (2.4) and (2.5), SNR now becomes:

$$\mathrm{SNR} = \frac{2\rho_0^2 P_{\mathrm{LO}} P_s}{2eB\rho_0 P_{\mathrm{LO}} + \frac{B}{R_e^2} S_{dark} + B\rho_0^2 P_{\mathrm{LO}}^2 S_{rin}(\nu)} \tag{2.9}$$

As mentioned in Section 1.2, fiber laser based CLD was widely used in mid 2000s. However, Erbium-doped fiber lasers have a ν_R around 1 MHz [24], and the peak of the relaxation oscillation can be as high as ∼40 dB above shot-noise [25]. It results in significantly elevated noise floor in frequencies extending to a few MHz, reducing the sensitivity at low wind speeds (0-5 m/s) in fiber-laser-based CDLs. It is common practice to avoid this issue by frequency shifting the LO away from the ν_R using an acousto-optic modulator(AOM) [26]. This technique also allows the CDL

to determine the sign of the radial wind speed. Another approach is the balanced heterodyne detection, first reported by Carleton and Maloney [27] in 1968. Both methods circumvent the effects of laser relaxation oscillation noise, but they require more components resulting in further insertion losses and increased cost. An active reduction of the relaxation oscillation peak with an electronic circuit has also been demonstrated to lower the RIN peak by ~ 20 dB [25], but this suppression might not be enough in some cases.

One of the advantages of semiconductor laser source is its high relaxation oscillation frequency, typically 1-10 GHz [24]. It is far beyond the Doppler bandwidth of interest (0.1-100 MHz) in turbine control applications. Thus, the RIN in semiconductor CDL system can be much smaller than the LO shot noise without further complications such as balanced detection or AOM shifted reference, reducing the cost further compared to the fiber-laser-based CDLs. Comparison of intensity noise spectra between a distributed feedback fiber laser (DFB-FL) and a master-oscillator power-amplifier semiconductor laser (MOPA-SL) was conducted in [28] (see Fig. 2.3). The result confirms, that semiconductor light sources can achieve a much better performance with respect to the RIN.

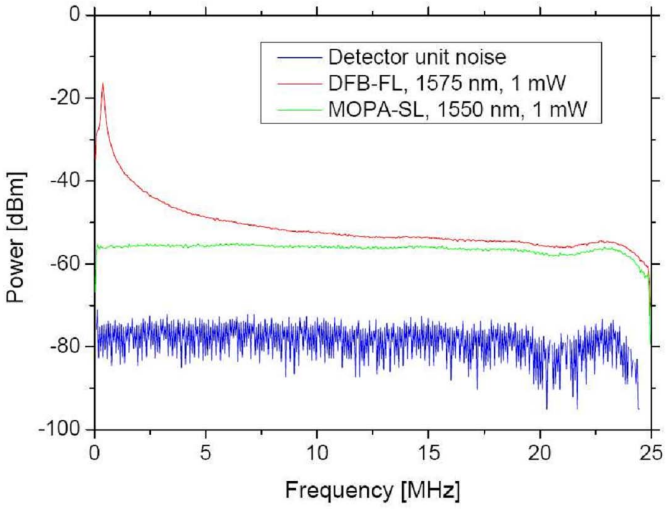

Figure 2.3: *Comparison of intensity noise spectra. The lowest (blue curve) is the noise spectrum of the detection unit, i.e., no laser light incident on the photo-detector. The green curve is obtained when ∼1 mW of optical power from the MOPA is incident onto the detector. The red curve is for the case when ∼1 mW beam from a fiber-laser is detected. The cut-off frequencies for the high-pass and low-pass filters of the detection unit are ∼100 kHz and ∼25 MHz, respectively. The plot is reproduced from [28].*

2.2.3 Phase Noise from Stray Light

While the mono-static design has the advantage of simplicity, unavoidable stray light (reflections) from the transmitting optics can reduce the sensitivity by interfering with the LO and produce a broad band noise spectrum. The noise level depends on the stray light strength, the laser linewidth, and the optical path difference between the stray light and the LO. The intensity of the mixing fields and the corresponding detector current can be expressed as:

$$\begin{aligned} I &= \tfrac{1}{2} nc\epsilon_0 (E_s + E_{\mathrm{LO}} + E_{stray})(E_s + E_{\mathrm{LO}} + E_{stray})^* \quad \Rightarrow \\ i(t) &\propto \tfrac{1}{2}\left[A_s^2 + A_{\mathrm{LO}}^2 + A_{stray}^2\right] + A_{\mathrm{LO}} A_s \cos\left[(\omega_s - \omega_0)t + \phi(t)\right] \\ &\quad + A_{\mathrm{LO}} A_{stray} \cos[\varphi(t)] \end{aligned} \tag{2.10}$$

where $\varphi(t)$ is the phase difference between the LO and the stray light. In the expression, the beating signal between the signal and the stray light have been neglected, since the LO is much stronger than both the lidar signal and the stray light. All the high frequency terms have been dropped as well. The frequency component of the beating between the LO and the stray light only contains the phase variation in time, since the frequency difference between them is zero. It is obvious from expression (2.10) that the interference is dependent on the stray light strength, while the impact from the light source linewidth is more subtle and is hidden within the phase difference, φ.

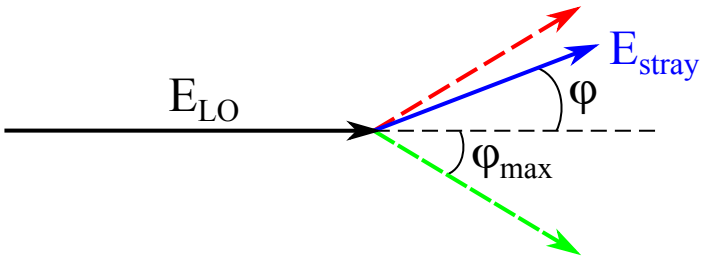

Figure 2.4: *A phasor diagram that illustrates the relative phase different variation between two optical fields tapped from the same light source with a time delay τ_d between them.*

Assume two optical fields originate from the same light source with a time delay, τ_d, between them – a refection from the optics in the lidar system and the LO. The phase difference between them will not be fixed, but varies randomly in time. The maximum phase difference, φ_{max} and phase variation speed increases with quantity $\frac{\tau_d}{\tau_{coh}}$, where $\tau_{coh} = (\pi\Delta\nu)^{-1}$ is the coherence time of the light source and $\Delta\nu$ is the light source linewidth. Figure 2.4 illustrates the phase variation between the two fields in the time domain. At any given time, the actually phase difference φ can have any values between the red and green phasor, defining the maximum phase deviation between the fields. Due to this variation of the phase difference, the power spectral density of the last beating term in expression (2.10) not only adds

additional intensity noise but it may also be dynamic; e.g., changes over time due to temperature dependence of the average phase difference φ.

This phase induced intensity noise (PIIN), N_p between the stray light and the LO can be expressed as [12]

$$N_p \cong \rho_0^2 B \frac{2P_{\mathrm{LO}}P_{stray}}{\pi}\frac{\tau_d^2}{\tau_{coh}}R_e^2 = 2B\rho_0^2 P_{\mathrm{LO}}P_{stray}R_e^2\tau_d^2\Delta\nu \tag{2.11}$$

for small delay times relative to the coherent time. This assumption is usually met in real CDL designs to keep PIIN negligibly small, since PIIN scales with τ_d^2. It is also clear from Eq. (2.11) that PIIN increases with the light source linewidth. Its impact on light source requirement in CDL design will be discussed in detail in Chapter 4. Finally, the complete SNR for a coherent lidar becomes:

$$\mathrm{SNR} = \frac{2\rho_0^2 P_{\mathrm{LO}}P_s}{2eB\rho_0 P_{\mathrm{LO}} + \frac{B}{R_e^2}S_{dark} + B\rho_0^2 P_{\mathrm{LO}}^2 S_{rin}(\nu) + 2B\rho_0^2 P_{\mathrm{LO}}P_{stray}\tau_d^2\Delta\nu} \tag{2.12}$$

Note the saturation effect of the detector response due to the LO power is not included in the expression above. The stray light power caused by the reflections within the system will typically be much stronger than P_s. Thus to suppress PIIN, a very narrow laser linewidth $\Delta\nu$ (in the kHz regime) is required; or the delay time τ_d between the source of the stray lights and the LO has to be very small. Note PIIN scales with the delay time squared, so the gain from the delay time reduction is more efficient than the linewidth restriction. As mentioned earlier, RIN can be avoided by choosing a light source with a ν_r far away from the Doppler RF band of interest, or by frequency shifting the LO using an AOM. Suppose both PIIN and RIN are successfully suppressed, the discussions in Section 2.2.1 and Eq. (2.7) will still be valid.

3 Lidar Signal

As discussed in the previous chapter, the SNR solely depends on the signal power, P_s, if the system noise is dominated by the LO shot noise. In this chapter, we will investigate how the lidar signal is affected by different system parameters such as insertion loss, backscatter coefficient of the target, telescope truncation, optical aberrations, and measurement volume.

3.1 Lidar Signal Power

Assuming the backscatters are evenly distributed in the atmosphere, and a monostatic CW lidar system with a finite foucs; the time-averaged signal power can be expressed as [29]

$$P_s = P_T \beta \lambda \left[\frac{\pi}{2} + \tan^{-1}\left(\frac{\pi r^2}{\lambda F} \right) \right], \quad P_T = \eta_o P_0 \tag{3.1}$$

where P_T is the transmitted power through the transceiver, β is the backscatter coefficient from the atmosphere, r is radius of the last lens of the transceiver, F is the focus distance from the transceiver, η_o is the optical insertion loss in the transmitting optics, and P_0 is the laser power. In most cases, the area of the aperture size will be much greater than the product of the wavelength and the focus location, $\pi r^2 \gg \lambda F$, hence $\tan^{-1}\left(\frac{\pi r^2}{\lambda F}\right) \simeq \pi/2$ and expression (3.1) becomes

$$P_s \simeq \pi P_T \beta \lambda \tag{3.2}$$

Interestingly, the total signal power of a CW CDL has nearly no dependency of the aperture size or the focusing range. But they do play a significant role in spatial confinement of the measurement volume that is highly important for turbine control. This subject will be treated later in this chapter.

Generally, there are two type of backscatters in the atmosphere, the air molecules and the aerosols. The molecules are much smaller than the wavelength, hence the scattering is characterized by a λ^{-4} dependence (Rayleigh scattering); while the aerosols are much larger particles, which have comparable size as the laser wavelength, resulting in Mie scattering. The wavelength dependence of the Mie backscatter coefficient is between λ^{-2} and λ^{-1} (from UV to IR) [30]. Thus in general, the

backscattering is dominated by aerosols in IR wavelength, while the situation is reversed in the cases of using UV light sources. Figure 3.1 shows the backscatter coefficients at 355 nm and 2.06 μm based on models derived from measurements during the GLObal Backscatter Experiment, GLOBE (1991). It is apparent that the scattering strength depends on the density of molecules and aerosols in the measurement volume, hence it drops with increasing altitude. For wind measurement applications in the wind industry, the impact from altitude difference between different turbine types is negligible. In this case, the air pollution and humility affect the backscatter coefficient much more. A 10 dB variation in the backscatter coefficient can easily be observed due to these effects.

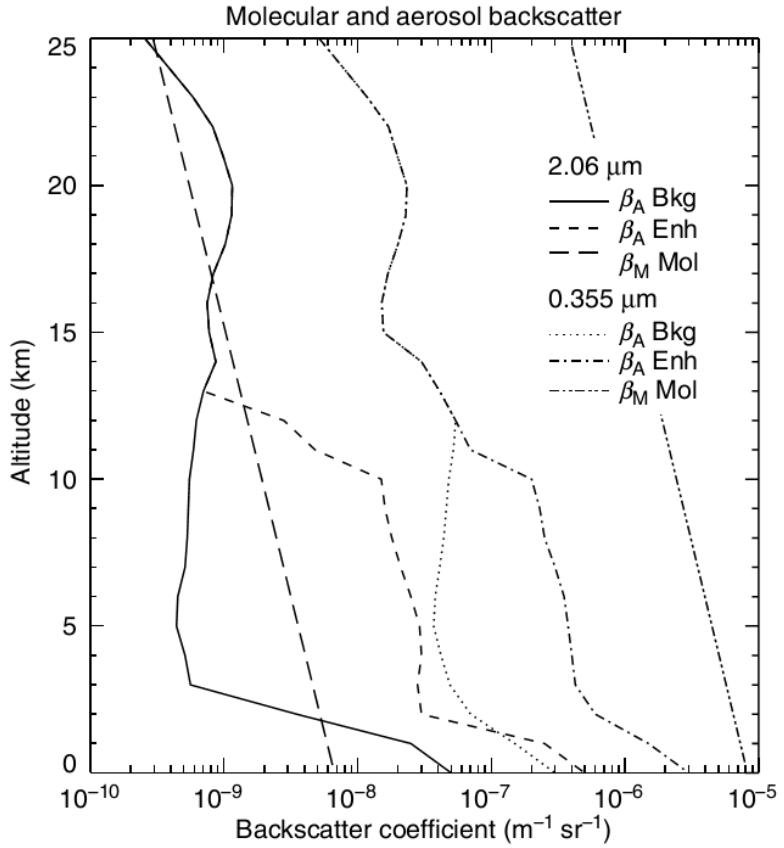

Figure 3.1: *Median aerosol and molecular backscatter coefficient models at 355 nm and 2.06μm, where β_A Bkg is the background aerosol backscatter coefficient based on the GLOBE measurement and β_M is the molecular backscatter coefficient. From [15] pp. 490.*

Based on Fig. 3.1, the backscatter coefficient of 2.06 μm light at zero altitude is between $5 \cdot 10^{-8}$ and $5 \cdot 10^{-7}$; and the wavelength dependence of aerosol backscattering is between λ^{-2} and λ^{-1}. Then, the backscatter coefficient at 1.5 μm at altitudes between 0 to 1 km should be around 10^{-7} as well. Recalling expression (3.2) the ratio between the optical signal power and the transmitted power, P_s/P_T, becomes around $5 \cdot 10^{-13}$. This explains why a relative high output power is needed for re-

liable signal detection, and emphasizes how sensitive coherent Doppler detection is. Another feature when including the wavelength dependence of β (between λ^{-4} and λ^{-1}) in expression 3.1 is, that the total signal power should benefit from going towards shorter wavelengths.

3.2 Probing Volume Confinement

As discussed in the previous section, the total signal power depends very little on the transceiver telescope design, but the transceiver does dictate the measurement volume of a CW CDL system. In the ideal case, the wind field is assumed to be completely laminar, hence all the energy from the Doppler wind signal is in the same frequency bin. In this case, the transceiver size and focusing range, truly, does not matter. However, the real wind profile in front of a turbine is often far from ideal, especially when the length of the measurement volume gets too large. In this case, the SNR will diminish as the signal bandwidth, B increases with the measurement volume, see Eq. (2.12).

As mentioned in Chapter 1, the measurement volume is defined by the weighting function. It describes how the lidar sees the contribution of the scatterer to the received the signal as a function of its position, z, along the lidar line of sight (LOS), and the FWHM of the weighting function defines the spatial resolution, also called the probe length, of the system. The measurement volume of a lidar is often defined as the probe length times the area of the beam waist in the target plane. To the first order, half the probe length, Γ in a CW lidar system scales with the probing range, R and the aperture size in following relation:

$$\Gamma \simeq \frac{\lambda}{\pi} \frac{R^2}{\omega^2} \tag{3.3}$$

where ω is the e^{-2} beam radius at the transceiver exit aperture. Since the probing range is usually fixed in turbine control applications, the limiting factor of the spatial resolution is often the exit transceiver lens size due to production cost.

Weighting Function Distortion

The shape of the weighting function in a CW CDL is defined by the spatial overlap between the output beam and the virtual back propagated local oscillator (BPLO) from the detector plane. Assuming perfect monostatic condition and ideal Gaussian output, the weighting function can be described by a Lorentzian distribution. For CW monostatic CDL system, the optimal truncation ratio, ρ between the laser beam and the transceiver is around 0.8 due to the trade-off between total transmitted power and the lidar antenna efficiency [15, 31]. In this case, the assumption of an ideal Guassian output is no longer valid. The optical power loss due to the truncation can be easily absorbed in η_o in Eq. (3.1), but the beam difraction by the beam truncation has to be treated. In this project, a thorough study of how the phase front distortion from the transceiver affects the weighting function profile was

conducted. The results are published in Optics Express in 2013 [**?**]. The content does not only consider the beam truncation, resulting in a Bessel beam output rather than a Gaussian beam, but the impact of aberrations in the transceiver optics was also treated. The published paper has been reformatted and is presented in the next section.

3.3 Investigation of Spherical Aberration Effects on Coherent Lidar Performance

In this paper we demonstrate experimentally the performance of a monostatic coherent lidar system under the influence of phase aberrations, especially the typically predominant spherical aberration (SA). The performance is evaluated by probing the spatial weighting function of the lidar system with different telescope configurations using a hard target. It is experimentally and numerically proven that the SA has a significant impact on lidar antenna efficiency and optimal beam truncation ratio. Furthermore, we demonstrate that both effective probing range and spatial resolution of the system are substantially influenced by SA and beam truncation.

Introduction

One of the main considerations in the development of the wind industry is the metrology issues. Essentially, more cost efficient and accurate wind velocity and turbulence mapping systems are highly desired [32]. Since the traditional cup and sonic anemometers require meteorological masts, a detailed turbulence mapping will require a tremendous amount of masts at different locations and heights. For this particular task the laser remote sensing (lidar) technology offers an attractive alternative [33]. In these systems, precise control of multiple lidar units are required in order to acquire the full 3D wind vectors with high a spatial resolution, which is determined by the overlap between the individual lidar weighting function that describes the spatial sensitivity and confinement along each beam direction.

Descriptions of various lidar system designs are well documented in the literature [15, 31, 34–36]. However, those are all theoretical treatments and focus mainly on diffraction limited system designs. A previous theoretical analysis did include the aberration effects [37], but only for a fixed degree of beam truncation at the exit aperture that is optimal for an aberration-free system. This work is dedicated to investigating the weighting function change under the influence of SA to provide an experimental counterpart of the theory proposed by Rye [37], and we will expand the analysis to include optimization of the beam truncation in the presence of SA. In practice, most lidar designs involve lens selection for the telescope or optical transceiver, which predominantly suffers from SA due to the difficulty in manufacturing lenses with SA-corrected surfaces especially for larger aperture sizes with short focal lengths. Furthermore, Rye showed numerically [37] that for equal degrees of coma, SA and astigmatism, the SA is found as the dominant contributor

to the lidar signal reduction.

Experimental setup

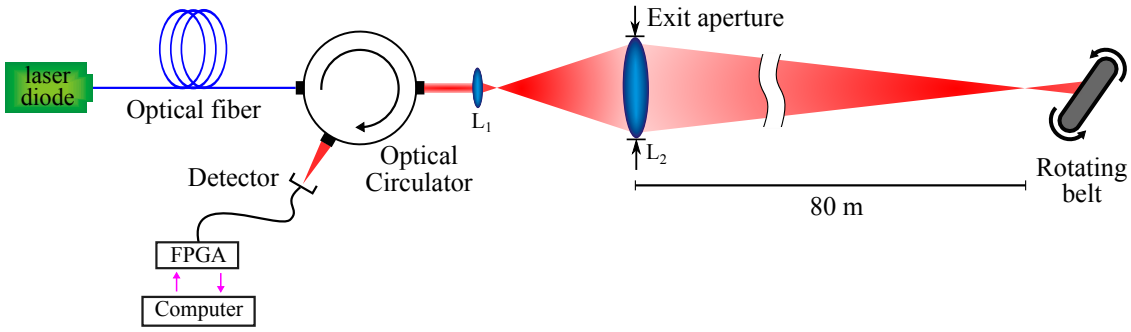

Figure 3.2: *Schematic layout of the system setup. The size of the exit aperture is the diameter of L_2. During the experiments several diffraction limited aspherical lenses, L_1 with different focal lengths are used in order to probe different ρ values; while two different L_2 are used to introduce different degree of aberrations. The rotating belt is used to generated the Doppler signal for our measurements.*

In this work the impact of the SA is measured by probing the lidar weighting function of the system with a rotating belt as the hard target using a 1550 nm CW beam output as shown in the schematic layout in Fig. 3.2. Both the simulation and the experiment follows the geometry in Fig 3.2. The distance between L_1 and L_2 is adjusted such that the lidar signal is optimized with the hard target (rotating belt) placed at a range of 80 m. Around 0.5 mW of the diode laser output is tapped within the optical ciculator and is used as the local oscillator (LO) for the heterodyne detection. Both the signal from the rotating belt and the LO is focused onto the detector through the optical circulator. The "virtual" back propagated local oscillator (BPLO) from the detector plane matches the transmit beam with a Gaussian field amplitude profile of radius, w, at the plane of lens L_2. This configuration is commonly referred to as the Wang design [31]. Different truncation ratios, $\rho = w/r_{L2}$ where r_{L2} is the radius of L_2 aperture, can be probed by changing the focal length (f_1) of lens L_1, since the imaging magnification of the beam is dependent on the focal length ratio between L_1 and L_2. Two different L_2, both with exit aperture radius of $r_{L2} = 35.65$ mm (3 inch optics), are used in our experiments in order to evaluate the system under different degrees of SA. The lenses (L_2) are respectively a singlet lens ($f_2 = 200$ mm) that is not corrected for SA and a doublet lens ($f_2 = 216$ mm) designed for reduced SA. The correlation overview between the L_1 focal lengths and ρ can be found in Table 3.1. A quantitative illustration of the SA introduced by the L_2 lenses is shown in Fig. 3.3(a), where the optical path difference (OPD) is measured in number of waves. The curves in Fig. 3.3(a) are generated using a Zemax simulation with monochromatic input, zero incident angle

Table 3.1: *Relation between focal lengths of L_1 and ρ*

Focal length of L_1	4.6 mm	8.1 mm	11.3 mm	15.6 mm	18.8 mm
ρ, singlet lens	1.28	0.73	0.52	0.38	0.31
ρ, doublet lens	1.38	0.79	0.56	0.41	0.34

and assuming circular symmetry in the transverse plane, i.e. only the symmetrical components of wavefront errors are presented. The first six nonzero Zernike fringe coefficients, generated in Zemax, are listed in Table 3.2. Those coefficients are used to generate the OPD curves and they differ slightly from the standard Zernike coefficients, which is evident from the polynomials provided in the table. A detailed description of those coefficients can be found in the user's manual of Zemax [38]. It is evident from the table values that the SA (Z_9) is the dominant source of the waverfront errors.

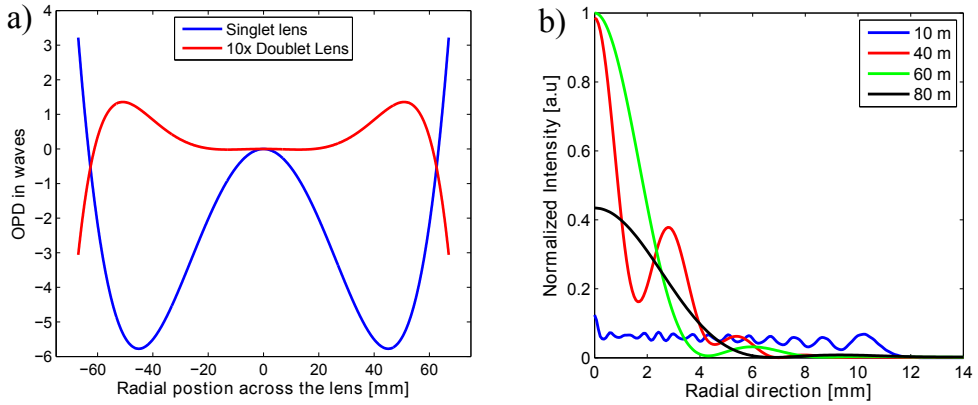

Figure 3.3: *a) The OPDs of the two different L_2 used in our experiments. The OPDs are generated in Zemax with zero incident angle and circular symmetry. b) The calculated transverse irradiance profile of the output beam in different axial distances from the singlet L_2. The focal length of L_1 is 15.6 mm in the simulation.*

An accurate theoretical prediction of the field or irradiance distribution on the target side of L_2 is possible using those OPD curves. The SA can be incorporated in the theoretical simulation by introducing an extra phase term, ϕ_{SA} to the truncated Gaussian field at L_2 according to Eq. (3.4) [37]

$$E(r) = \begin{cases} E_0 \exp\left\{-\frac{r^2}{w^2} + i\phi(r) + i\phi_{SA}(r)\right\} & , 0 \le r \le r_{L2} \\ 0 & , r > r_{L2} \end{cases} , \phi_{SA} = 2\pi * \mathrm{OPD}(r) \quad (3.4)$$

where E_0 is the peak amplitude, r is the radial coordinate, $\phi(r)$ is the phase of the beam due to field curvature, ϕ_{SA} is the phase term induced by the SA and the OPD(r) is either curves shown in Fig. 3.3(a). Due to the circular symmetry, the field on the target plane can be calculated numerically by a simple Fourier-Bessel transformation of Eq.(3.4) with an appropriate field curvature [37].

Table 3.2: *Zernike fringe coefficients from Zemax*

Term Z_j	Singlet L_2	Doublet L_2	Zernike fringe polynomials
Z_1	-3.27339159	0.03707405	1
Z_4	1.50844787	-0.05266555	$2p^2-1$
Z_9	4.87996531	-0.18513369	$6p^4-6p^2+1$
Z_{16}	0.10038714	-0.10019848	$20p^6-30p^4+12p^2-1$
Z_{25}	0.00231510	-0.00501370	$70p^8-140p^6+90p^4-20p^2+1$
Z_{36}	0.00005509	-0.00021833	$252p^{10}-630p^8+560p^6-210p^4+30p^2-1$

Results and discussions

To illustrate the degree of SA for the singlet L_2 case, the transverse irradiance profiles in different distances, z after the singlet L_2 are calculated and shown in Fig. 3.3(b). A side by side comparison between the numerical simulation and the experimental counterpart of the beam profiles is displayed in Fig. 3.4. The observed beam profiles are recorded with aid of an IR-detection card. An intensity clipping level was introduced in the presentation of the numerical results in order to simulate the saturation effect of the IR-detection card. In Fig. 3.4 the consistency between the simulations and the measurements is quite evident, qualitatively validating the accuracy of our theoretical simulations.

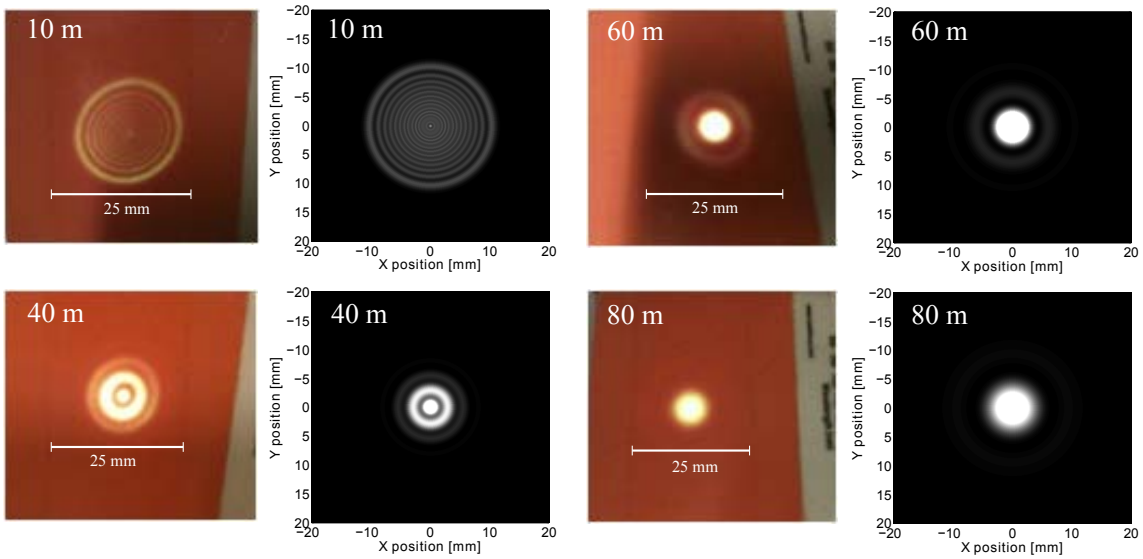

Figure 3.4: *The observed and simulated beam profiles emitted from the singlet L_2 in different axial distances (10m, 40m, 60m and 80m) The focal length of lens L_1 is 15.6 mm.*

In order to maximize the signal in diffraction limited monostatic lidar systems, $\rho \approx 0.8$ through the L_2 is required [15]. However, in the presence of SA, optimal ρ will differ from 0.8 and the overall antenna efficiency will decrease compared to the

aberration-free case. It is easiest to calculate the antenna efficiency, η_a using the target-plane formalism based on Siegman's antenna theorem [15, 39].

$$\eta_a(z) = \frac{\lambda^2 R^2}{A_r} \iint I^2_{\text{target}}(x, y, z) dx dy \tag{3.5}$$

where λ is the wavelength, R is the intended imaging or probing range (80 m in our case), A_r is the area of L_2 and I_{target} is the irradiance distribution of the output beam at the target plane position, z and is normalized by the total beam power before truncation.

In Fig. 3.5(a) the calculated antenna efficiency at $z = R$ as a function of ρ is shown for both L_2 lenses and compared with the aberration-free case (the dashed lines). The simulation is constructed such, that the algorithm is imitating the same distance optimization procedure as in the experiments. It is evident that not only the overall antenna efficiency has decreased as the consequence of SA, but the optimum ρ also shifts with different degrees of aberrations. Even for the doublet case where the SA is minimal, there is still a clear shift of the optimal ρ and a quite noticeable drop in the maximum antenna efficiency. It demonstrates the importance of considering the aberration effects in designing a lidar system. The result in Fig. 3.5(a) indicates that optimal ρ decreases with increasing degree of SA.

The measured hard target lidar signal as a function of ρ, normalized to the maximum data point of the doublet case, is also shown in Fig. 3.5(a). The experimental data shows the same tendencies as the numerical calculations. While the singlet data coincides quite well with the simulations, there is a slight deviation for the doublet case. Since the simulation only includes the SA effect, it is reasonable that the doublet data can deviate from the simulation due to other aberration effects in the rest of the system (we do observe small degree of astigmatism from the output of the optical circulator). The singlet data is, on the other hand, dominated by the SA, which explains the good agreement with the simulation.

So far we have shown how the SA affects the optimal ρ with respect to the maximum antenna efficiency at fixed target distance equal to the intended probing range R. However, the graph in Fig. 3.5(a) only provides an optimal ρ for hard target case. For aerosol target, it is necessary to analyze the lidar weighting function, which provides the effective probing range (may differ from R due to aberration), the spatial resolution and the total signal strength of the system. In a monostatic CW lidar the weighting function is commonly described by a Lorentzian function, F under the assumption of an ideal and untruncated Gaussian beam [16],

$$F = A \frac{1}{(z - R)^2 + z_0^2} \tag{3.6}$$

where A is a normalization constant, z is the distance from L_2 and z_0 is the Rayleigh length of the output beam. However, we just demonstrated in Fig. 3.5(a) that a rather large ρ of around 0.8 is required in order to obtain the optimal antenna efficiency for the aberration-free system. In that case the output will suffer from significant diffraction effects due to the truncation and therefore no longer be considered as an ideal Gaussian beam. In Fig. 3.5(b) the antenna efficiency is calculated as

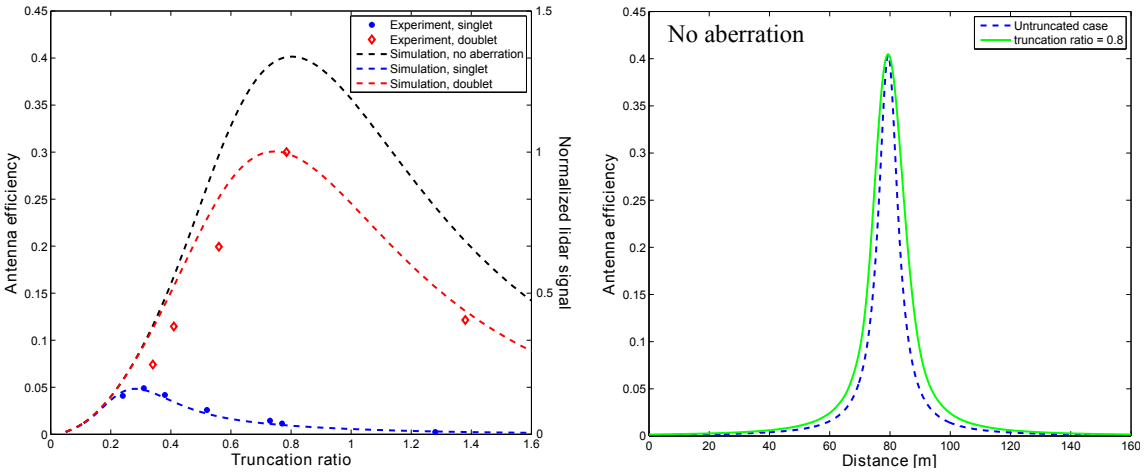

Figure 3.5: *a) The dash lines illustrates the numerically calculated antenna efficiency using Eq. (3.5) as a function of ρ; while the scattered points shows the measured lidar signal as a function of ρ. Both the simulation and the experimental data are acquired at a probing range of 80 m. b) The simulated antenna efficiency for the aberration-free case as a function of distance with and without the truncation effect ($\rho = 0.8$ for truncated case).*

a function of the distance for two different cases: 1) including the truncation effect by numerical integration of Eq. (3.5) and numerical Fourier-Bessel transform of the field in Eq. (3.4) to obtain I_{target}. 2) Using Eq. (3.6) based on the untruncated Gaussian beam assumption. The result demonstrates a broadening of the weighting function by 56% when including the truncation effect, which is quite significant. Since the width of this Lorentzian distribution is directly related to the spatial resolution of the lidar system, the truncation effect should not be underestimated in the system design.

The weighting function can be acquired experimentally by measuring the lidar signal with a moving hard target. The experimental data of six different combinations of L_1 and L_2 are presented in Fig. 3.6 along with their numerical counterparts. In general the numerical results coincide quite well with the experimental data, but the singlet case gives a much better match than the doublet case. As we discussed earlier the simulations only include the SA effect, since the measurement with singlet L_2 is dominated by SA while the doublet L_2 case is not, it is expected that singlet lens case will provide a better fit. The simulation results do suggest that the full system (not only L_2) potentially suffers from other aberration effects like astigmatism and coma, which are comparable with the SA introduced by the doublet L_2, since the experimental data shows a visible broadening of the weighting function compared with their numerical counterparts. Comparing the simulation with the experimental data there is a broadening of 21% for the green dash line ($f_1 = 8.1$ mm) while the broadening is 70% for the blue dash line case ($f_1 = 18.8$ mm). The residual broadening is likely due to the astigmatism of the beam from the optical circulator, which also explains the observed increase in the degree of broadening

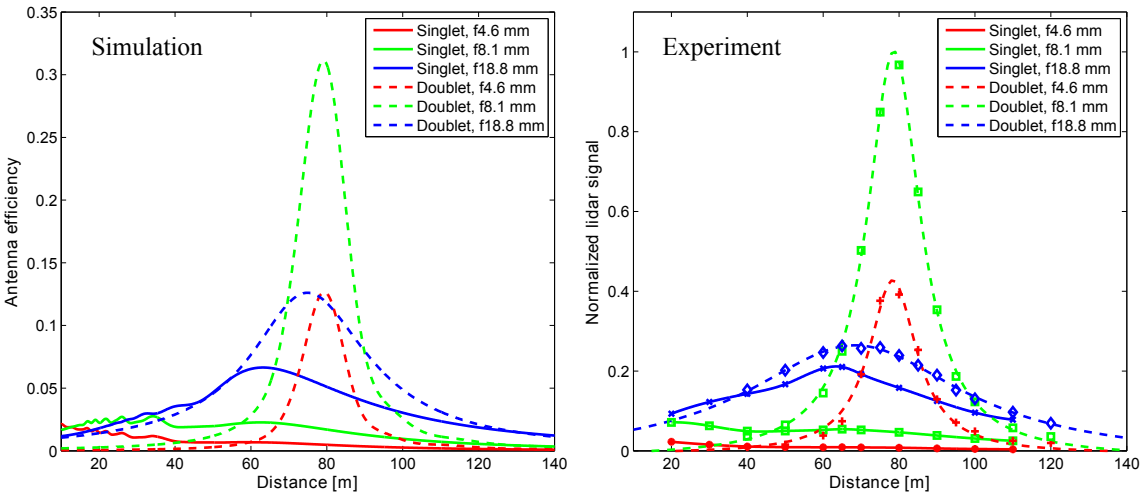

Figure 3.6: *The measured weighting functions for six different transceiver configurations along with their theoretical counterparts. The simulations are acquired using the numerical integration of the fields including the truncation diffraction effects. The blue solid line represents the optimal ρ of 0.3 for the singlet case, while the green dash line corresponds to the optimal ρ of 0.8 for the doublet case. The dash lines in the graph to the right are the Lorentzian fit to the experimental data (scattered points).*

with the focal length of L_1.

From Fig. 3.6 it is quite obvious that in general one should reduce SA in the system, since both the spatial resolution/confinement and the maximum signal strength of the optimal doublet case (green dashed line) are much better than the optimal case for the singlet lens (blue solid line). However, the area under the weighting function (estimating the total lidar signal strength for aerosol target) has only increased by around 30% from the optimal singlet case to the doublet one. So for measurements of laminar air flow (i.e. negligible spatial dependence of wind vector), the benefit gained from using the more expensive doublet L_2 is minor in terms of signal strength enhancement but more on improved spatial resolution. For the more general turbulent air flow in the probing volume, higher signal strength enhancement due to tighter spatial confinement is of course expected.

From the previous theoretical treatments [37] we know that for a fixed ρ the weighting function will suffer from both peak shift and broadening effects under the influence of SA. Recalling Eq. (3.5) and the transverse irradiance profiles in Fig. 3.3(b) it is expected that the weighting function for the singlet L_1 case will have a peak around 60 m, since the effective beam confinement is tightest there and not at the intended imaging range, 80 m. The data shown in Fig. 3.6 provides, to our knowledge, the first experimental confirmation of these tendencies. But our numerical and experimental results also show that both the peak shift and the broadening effect can be compensated to certain degree by selecting a ρ appropriate for a particular degree of SA, which is not described in the theoretical work by Rye

[37]. From the OPD curve in Fig. 3.3(a) we know that the doublet L_2 only suffers from minor SA, nevertheless, we still observe a weighting function peak shift of 2.4 m (for L_1 focal length of 8.1 mm), indicating the sensitivity of the lidar system to the SA effect. We also note in Fig. 3.6 that the peak shift is larger for lower ρ. Thus, in applications where delicate probing range control is necessary, it is advisable to calibrate the lidar system with a hard target by mapping the weighting function.

Conclusion

In this paper we have shown both numerically and experimentally that SA has a significant impact on antenna efficiency, optimal truncation ratio and the shape of the weighting function of a CW coherent lidar. If the system suffers from strong SA effect only very limited spatial confinement can be obtained as shown in Fig. 3.6. It is also evident that the degradation of spatial confinement or broadening of the lidar weighting function due to SA can be reduced by tuning the beam truncation through L_2. This corrective measure results from the novel finding in this work that the optimal truncation ratio depends on the degree of SA. Furthermore we have shown that both SA and truncation ratio influence the peak shift and width of the weighting function. In applications where precise probing range and spatial resolution are essential, a weighting function calibration of the lidar system using a hard target might be necessary. It is worth to stress that this study can also be applied to accurately model the weighting function of pulsed coherent lidar systems [33].

3.4 Astigmatism and Monostatic Condition

As observed in Fig. 3.6, the simulation and the experimental data match quite well.[1] Figure 3.7 shows both the simulation and the experimental result of the weighting function in the ideal case (the green dash line curves from Fig. 3.6). The small discrepancy can be caused by two different reasons or a combination of them: 1) Astigmatism in the transmitting optics, and/or 2) imperfect monostatic condition in the transmitting optics.

The astigmatism was not included in the simulations, but we know from [36] that astigmatism should introduce a broadening of the weighting function without shift in its peak position; and normally, the impact of SA will dominate over the astigmatism. An effort to quantify the astigmatism in the system was made using a beam profiler placed between the L_1 and L_2 in the set-up shown in Fig. 3.2. Unfortunately, the measurement uncertainty was too big to provide a conclusive result.

Since the LO is not tapped from a fiber tip, but rather from within the optical

[1] a small correction: it was stated "Comparing the simulation with the experimental data there is a broadening of 21% for the green dash line". However, the real deviation is actually only 13% and not 21%.

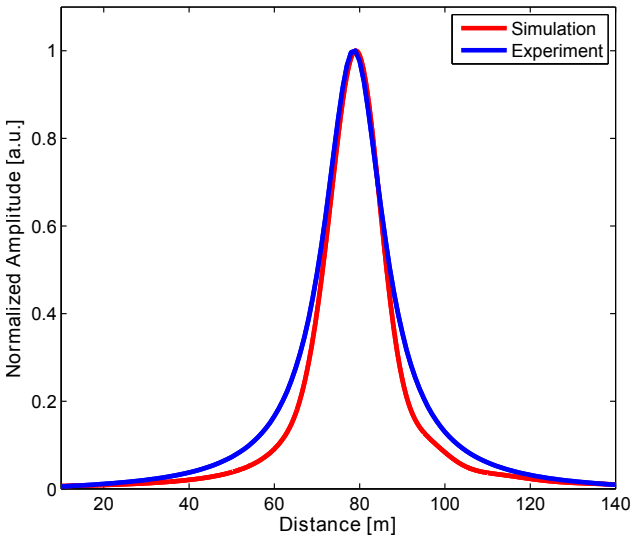

Figure 3.7: *The green dash curves from Fig. 3.6, both data set has been re-normalized to the peak value of the experimental data. There is only a 13% devaition between measured weighting function and the simulation.*

circulator, the monostatic conditions will not necessarily be fulfilled, see the discussion in Section 4.1. Slight misalignment in the transmitting optics, particularly from the surface where the LO is tapped, inside the circulator can cause deviation from the perfect monostatic condition. As discussed in the previous section, the shape of the weighting function is dictated by the overlap integral between the BPLO and the output beam. A small angular displacement between the two will change the optical path length between them as well. Figure 3.8 illustrates how this will look like in the target plane (the sketch is highly exaggerated). The spatial displacement between the two focal positions will cause a broadening of the weighting function.

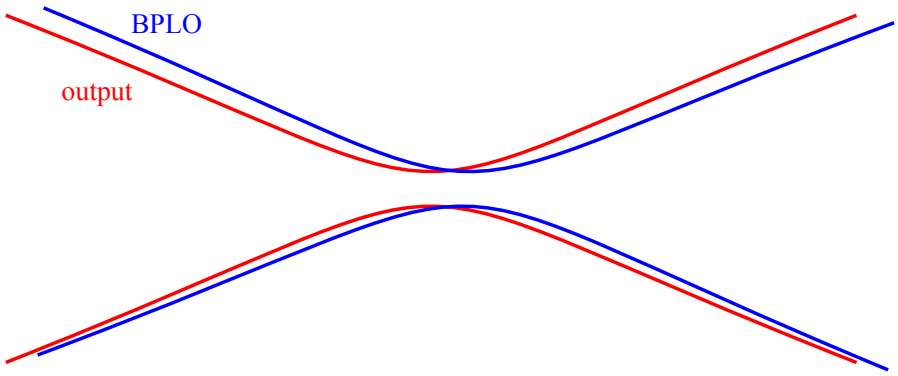

Figure 3.8: *An illustration of possible spatial overlap between the BPLO and output beam. The blue line represent the BPLO, while the red line represent the out put beam.*

4 Light source

The heart of this project is to utilize a semiconductor light source to reduce the lidar cost, since the main cost contributor of a conventional fiber laser lidar is the light source [17]. The light source of choice is a 1.5 μm single-frequency semiconductor master oscillator power amplifier (MOPA), where both the MO and PA part are integrated on the same die. The laser die can reach an optical power output of approx. 1 W while having a relatively narrow linewidth (hundreds of kHz to a few MHz). For easy handling, the laser die is integrated in a butterfly package (30 mm $\times$ 12.7 mm) with a single mode fiber pigtail, and the relatively good beam quality allows for around 60% coupling efficiency into a single mode fiber.

4.1 PIIN Suppression

As mentioned in Chapter 2, the RIN (in the form of relaxation oscillation noise) in the RF band can be efficiently avoided by using a semiconductor laser source. However, the linewidth of semiconductor lasers are relatively large, which can have a significant impact on the PIIN according to Eq. (2.12). In the first all-fiber CDL system [12], two semiconductor lasers were used as seed for a EDFA . They concluded that, due to the stray light from the EDFA and the crosstalk in the optical circulator, shot noise limited operation can not be reached when using a semiconductor laser seed. In this project, the stray light from an optical amplifier is circumvented by using the integrated MOPA, but the excess noise from circulator crosstalk is expected to be much worse due to the increased linewidth.

Recalling Eq. (2.11), the PIIN scales linearly with the laser linewidth and has a quadratic dependence on the delay time, τ_d. So in principle, if the delay time can be reduced sufficiently, the PIIN should still be manageable even with an increased linewidth. In an all-fiber CDL design, the LO is generated from the Fresnel reflection from the fiber end at the input to the optical transceiver. This configuration has the advantage that the signal beam and the LO will always propagate along the exact same optical patch, i.e., the monostatic condition is auto-fulfilled. However, this configuration also gives arise to a relatively large delay time (around $\tau_d = 10$ ns) between the LO and the stray lights from within the fiber-optic circulator, Since the LO is tapped from the tip of a 1 m long fiber pigtail. For this reason, the fiber-optical circulator approach has be to abandoned in our design. Instead, we have

designed a free-space optical circulator, where the LO is tapped within the circulator itself. In this way, the delay time between the LO and the stray light sources within the circulator is kept below 67 ps. According to Eq. (2.11), this should suppress the PIIN by 3 orders of magnitude, compensating for the large linewidth difference between the semiconductor and fiber-laser based light source. In this design, not only the delay time is reduced significantly, the crosstalk has also been suppressed below -80 dB.

4.2 Linewidth Measurement

The spectral content of a laser can be measured using a self-heterodyne set-up as shown in Fig. 4.1. This technique was originally proposed by Okoshi et al.[40]. The self-heterodyne spectral line shape of a laser source is a convolution of two components: a Lorentzian component resulting from the white frequency noise and a Gaussian component due to the $1/f$ frequency noise. If the measured spectrum originates from the Lorentzian component, it is 2 times the laser linewidth; and $\sqrt{2}$ times the laser linewidth when it is the Gaussian component [40]. In practice, the factor will always be between 2 and $\sqrt{2}$, since every light source contains both white frequency noise and $1/f$ flicker noise [41, 42].

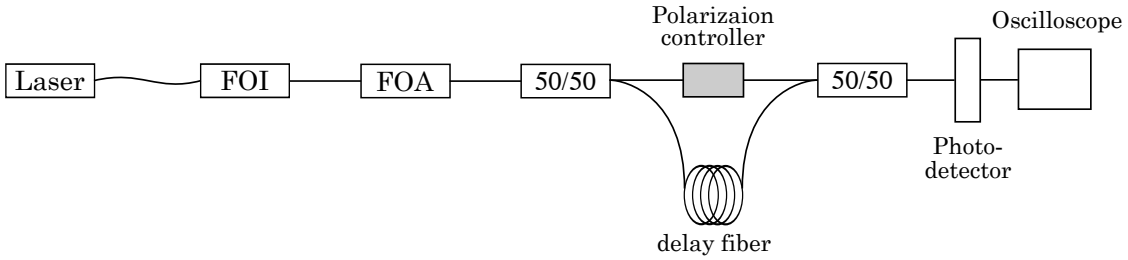

Figure 4.1: *A self-heterodyne set-up for laser linewidth measurement, where FOI is a fiber optical isolator, and FOA is a fiber optical variable attenuator. From my conference contribution [43].*

The self-heterodyne spectrum originates from the Lorentzian component is independent of delay length in the set-up, while the Gaussian part of the spectrum increases with the delay length [44]. This complicates the definition of the laser linewidth further. Many laser manufacturers specify the laser linewidth without specifying the corresponding self-heterodyne delay length. It is adequate only in cases, where the Lorentzian component is the dominant term in the measured spectrum. Since the Gaussian part increases with the delay length and the Lorentzian does not, the Gaussian component will always become the dominant term, when the delay length is long enough. Thus, it is important to specify the delay length when defining the laser linewidth.

An empirical expression describing the spectral width of the Gaussian compo-

nent, Δg, was presented by Mercer [44]:

$$\Delta g = \frac{1}{\pi}\sqrt{\frac{2\kappa \ln 2}{\pi}\left(4.3 + \ln\frac{4.3\kappa\tau_0^{2.1}}{\pi}\right)} \tag{4.1}$$

where κ is a device specific parameter that describes the $1/f$ noise, τ_0 is the delay time caused by the delay fiber and G is measured in Hz^2 in FWHM; the expression is only valid for $\frac{\kappa\tau_0^2}{\pi} \gg 1$ – the incoherent regime.

In Fig. 4.2, linewidth measurements of the same light source with different delay lengths are presented. The Gaussian part of the linewidth shown in Fig. 4.2(b) are obtained by fitting the data in Fig. 4.2(a) to a Voigt profile. Only the red part of the curves are used for the Voigt fit, due to the inherent high-pass filtering in the detector (AC coupled). It is quite evident, that the laser linewidth depends on the delay length in measurement set-up, and expression (4.1) matches well with the measured data in the incoherent region (the last 5 data points). The kink of the slop in Fig. 4.1 can be considered as the transition between the coherent and incoherent regime of the light source. This kink is also described in [44].

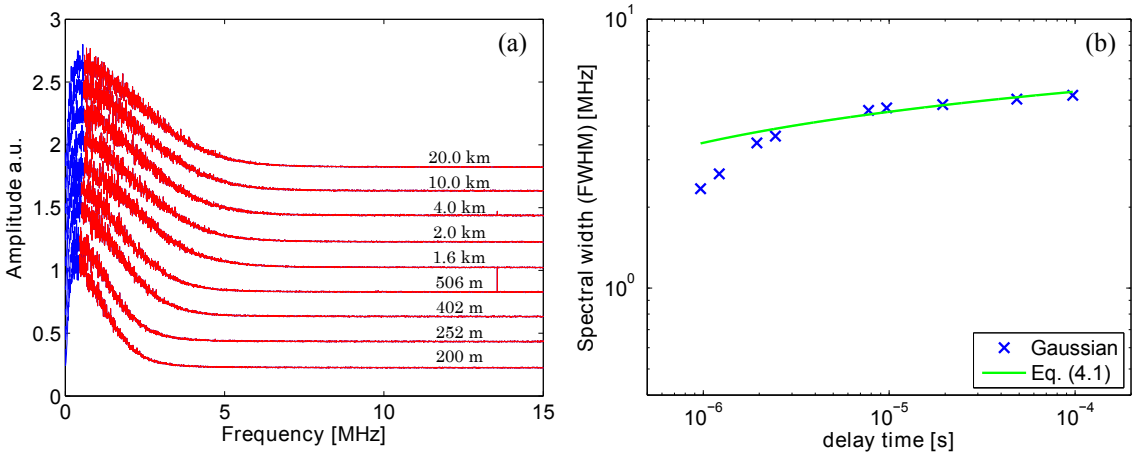

Figure 4.2: *Linewidth measurement of the same light source as function of the delay fiber length using the set-up shown in Fig. 4.1. (a) shows the actual spectral contents from the measurement. (b) shows the Gaussian part of the linewidth of each curve taken in (a) and compares them with expression* (4.1) *when* $\kappa = 3.9 \cdot 10^{13}$ *Hz*^{2}.

In remote wind sensing applications using a coherent lidar system, it is reasonable to require the coherent length of the light source being longer than twice the probing distance, as the light travels twice that distance before it reaches the detector. The common definition of the coherent length is $L_{coh} = \frac{c}{\pi\Delta\nu}$, where $\Delta\nu$ is laser linewidth. However, as shown in Fig. 4.2, the linewidth depends on the delay time in the heterodyne set-up, which makes the definition of coherence length more complicated. In this work, a considerable amount of time was spent to investigate the laser linewidth requirement of lidar based turbine control. The founding was

published in Optics Letter in 2014 [45]. The contents has been reformatted and is presented in the next section.

4.3 Remote Wind Sensing With a CW Diode Laser Lidar Beyond the Coherence Regime

We experimentally demonstrate for the first time (to our knowledge) a coherent CW lidar system capable of wind speed measurement at a probing distance beyond the coherence regime of the light source. A side-by-side wind measurement was conducted on the field using two lidar systems with identical optical designs but different laser linewidths. While one system was operating within the coherence regime, the other was measuring at least 2.4 times the coherence range. The probing distance of both lidars is 85 m and the radial wind speed correlation was measured to be $r^2 = 0.965$ between the two lidars at a sampling rate of 2 Hz. Based on our experimental results, we describe a practical guideline for designing a wind lidar operating beyond the coherence regime.

In recent years, coherent lidar systems have drawn a lot of attention from the wind energy industry. Lidar systems offer a unique capability to measure wind profiles ahead of wind turbines, which can be used to improve the turbine power output, reduce load, and prolong its lifetime[46]. This lidar application typically requires an "eye-safe" light source operating at wavelength λ in the infrared region, narrow linewidth in the <100 kHz regime, and output power of about one Watt. These requirements have been met by using fiber lasers at 1.55 μm (telecom wavelength) combined with erbium-doped fiber amplifiers (EDFA), since fiber laser technology can readily provide kHz linewidth performance at Watt-level average power. Furthermore, due to the maturity and availability of telecom components, the lidar optical design also becomes easier to implement. Unfortunately, fiber lasers and EDFAs are relatively expensive – restricting the fiber laser based lidar system as a scientific instrument.

An attractive alternative for fiber lasers is found in low-cost narrow linewidth diode lasers which can be mass-produced on wafers – enabling wind lidars for industrial use. The first demonstration of such a lidar system was accomplished in 2008 [18] using an integrated 1.55 μm single-frequency semiconductor master oscillator power amplifier (MOPA) with a linewidth in the order of 100 kHz and an output power reaching 1 W. However, we find that the measured linewidth (using a self-homodyne setup including a 2-km-long fiber delay) of these MOPA systems vary from unit to unit in the range of ∼100 kHz to a few MHz. Linewidth broadening in MOPAs is influenced by e.g. unwanted optical feedback [47] and amplified spontaneous emission coupling [48] from PA to MO section. If the laser coherence requirement can be relaxed, the potential yield of diode MOPAs for wind lidars will increase significantly.

The conventional way of determining laser linewidth is to measure it in a self-

heterodyne setup with a sufficiently long fiber delay. The laser linewidth is then defined as the half width half maximum (HWHM) of a Lorentzian fit to the measured self-heterodyne spectrum. However, this is only valid when the power spectral density (PSD) of the instantaneous laser frequency is white — i.e. independent of the sampling frequency, f. For semiconductor (diode) lasers, the $1/f$ frequency noise contribution is often non-negligible. Thus, the measured width of a self-heterodyne spectrum is dependent on the delay length [44], making the definition of laser linewidth more complicated. Despite this issue, previous authors [49] have relied on the conventional assumption of a Lorentzian laser lineshape when analyzing the role of coherence in semiconductor lasers for lidar applications.

In this Letter, we present (to our knowledge) the first demonstration of a coherent CW lidar system that can measure wind speed at a distance beyond the laser coherence regime. The system performance was evaluated against a similar MOPA lidar system but employing a diode laser with a much narrower linewidth. We discuss the laser linewidth constraint on a CW lidar by addressing the following issues: 1) the effective instrument response in the presence of $1/f$ frequency noise, 2) the dependence of phase induced intensity noise (PIIN) on linewidth, and 3) the influence of the wind speed distribution, which typically describes a non-laminar flow, on the lidar spectrum. Note that the aspects influencing the laser linewidth constraint described in this work are general in nature, and can be applied to any solid or distributed targets with different velocity profiles.

The lidar measurements were tested against a standard Metek 3D sonic anemometer. The side-by-side comparison of Lidar1 and Lidar2 is realized in a field test configuration sketched in Fig. 4.3. The self-heterodyne spectrum width of the lasers in Lidar1 and Lidar2 were measured to be <200 kHz and 10 MHz, respectively, using a 2 km fiber delay (see setup in [50]). The optical design of the two lidar systems is identical and is described in our previous work [51]. The probing distance of the lidars was determined to be 85 m from measurements of their spatial weighting function using a solid target [51]. The field test was conducted during a clear sunny afternoon and the optical output powers of the lidar systems are within a 5% difference.

In general, the physical principle behind a Doppler lidar is equivalent to that of a delayed self-heterodyne linewidth measurement setup. The delay time is just determined by the transit time for light to traverse twice the lidar probing distance (instead of the optical path length of the 2 km fiber delay). To describe the instrument response, consider the case where the wind profile is laminar. If the probing distance is within the coherence regime of the light source (Lidar1), the width of the corresponding lidar spectrum will be limited primarily by the resolution bandwidth of the data processing electronics. However, when the probing distance is beyond the coherence region (Lidar2), the width of the lidar spectrum is influenced by the laser self-heterodyne spectral width (in our case 2.7 MHz), which is much broader than the signal processing resolution bandwidth (147 kHz). The spectra described above can be considered as the instrument response of Lidar1 and Lidar2, respectively, and can be probed using the setup in our previous work [51] with a hard

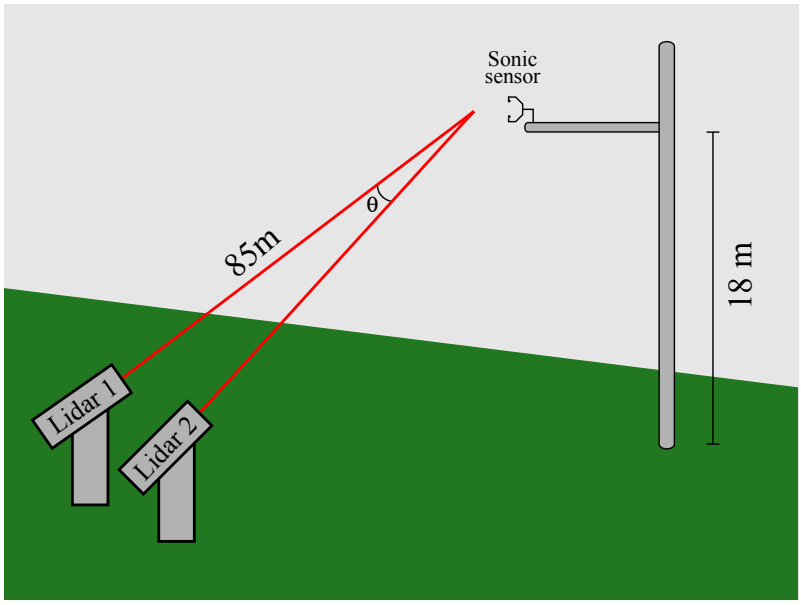

Figure 4.3: *Schematic layout of the setup. Lidar1 and Lidar2 are placed side-by-side with their beams focused a few meters away from the sonic anemometer. The probing distance of each lidar is around 85 m and* $\theta \approx 0.3°$.

target placed at 85 m distance (simulating a laminar wind profile). The response function of Lidar1 was measured to have a full width half maximum (FWHM) of ∼200 kHz (limited by the electronics), while it is 2.7 MHz for Lidar2. In our system, the instrument response can be considered as the self-heterodyne spectrum of the lidar with a delay distance of 170 m in free space. It is apparent, that the spectral width of Lidar2 is smaller than that for the 2 km fiber delay case; which is consistent with the theory described in an earlier study [44].

It is possible to estimate the degree of coherence for Lidar2 using its instrument response spectrum. Note that the laser field spectrum is accurately modelled by the convolution of a quasi-Gaussian spectrum (due to $1/f$ frequency noise) and a Lorentzian spectrum (white frequency noise component) [44]. Assuming the response spectrum is purely Lorentzian with a FWHM of 2.7 MHz, we can calculate an upper limit for the coherence length, $L_{\text{coh}} = c/(\pi\Delta\nu)$, where ν is the HWHM of the response spectrum [52]. The obtained coherence length is 69 m, which corresponds to a probing distance of 34.5 m in our lidar setup, if Lidar2 needs to measure within the coherence regime. In our system, the probing distance of Lidar2 is at least a factor of 2.4 of the coherence range.

The performance of a coherent detection lidar can be characterized by the carrier-to-noise ratio (CNR), i.e. the power of the modulated signal divided by the receiver noise power. In our case, the modulated signal (oscillating at Doppler shift frequency, ν_d) is the photo-detected beat signal between a laser-tapped local oscillator (LO) and the received Doppler shifted back-scattered field. For a signal bandwidth

B,

$$CNR(t) = \frac{\eta P_S(t)}{h\nu B F(t)}, \qquad F(t) = 1 + S_D + S_{\mathrm{PIIN}(t)}, \tag{4.2}$$

where η is the net efficiency considering optical losses, heterodyne efficiency and detector sensitivity, $P_S(t)$ is the optical power of the received Doppler shifted signal, h is Planck's constant, ν is laser frequency, and F represents the total noise power normalized to the optical shot noise power of the LO [15]. S_D and S_{PIIN} are the PSDs from detector dark noise and PIIN, respectively, normalized to the LO shot noise PSD. In most optimized coherent lidar systems, the detector dark noise can be neglected, while SPIIN can contribute significantly to the excess noise. In general, PIIN dynamically lifts the noise floor above LO shot noise as a result of interference between stray light reflections from stationary surfaces and the LO. These reflections are generated as the transmit beam passes through the lidar optics. The nominal strength of the PIIN scales linearly with the laser source linewidth [28], which is one main reason for the general requirement of using narrow linewidth light sources in coherent lidar systems. In our optical design, PIIN is strongly suppressed due to minimal spurious reflections (e.g., by introducing slight tilt when aligning the optics) and reduced path differences between LO and residual stray light sources. This allows us to relax the linewidth requirement while still keeping PIIN sufficiently low.

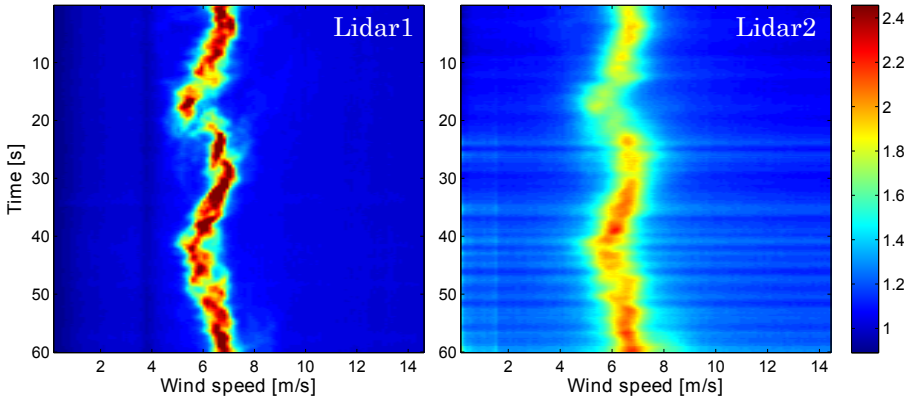

Figure 4.4: *Wind data from both lidar systems in the same time frame. The update rate of the presented data is 5 Hz. Both plots are normalized to the noise floor of Lidar1. The colour intensity represents the Doppler signal strength.*

Raw wind data is obtained from 512-point fast Fourier transform (FFT) of the photodector signal time series sampled at 75 MHz. Figure 4.4 illustrates the acquired wind data from both Lidar1 and Lidar2 as function of time. The presented data is time averaged to an update rate of 5 Hz. The Doppler signal strength is given by a color intensity scale that applies for both Lidar1 and Lidar2 plots. In Fig. 4.4, we observe a fairly constant (unity) noise floor in the wind data of Lidar1. This indicates that in Lidar1, PIIN is sufficiently suppressed due to the narrow linewidth

of its laser source. However, the PIIN, clearly observed as light blue stripes in the Lidar2 plot, is comparable to that of the LO shot noise. The fluctuating average noise floor ranges from ∼1 to ∼1.5. Figure 4.5 is the result of a simple subtraction of the time-varying noise floor from Fig. 4.4. Despite the increased PIIN in Lidar2, it is kept to a level that does not overwhelm the wind signal—maintaining a well-defined Doppler peak that coincides well with that of Lidar1. It is apparent from Fig. 4.5, that both systems are capable of determining the average wind speed with temporally consistent results. Noticeably, the effect of the increased laser linewidth from Lidar1 to Lidar2 manifests as a broadening of the wind spectrum, which is related to frequency jitter between two portions of the laser output when one portion is delayed with respect to the other.

Since the response function width is limited by the signal processing resolution bandwidth for a lidar whose probing distance is well within its coherence regime [49], the Lidar1 data in Fig. 4.5 essentially represents the actual wind speed distribution in probe volume, which makes Lidar1 capable of resolving finer features of the Doppler spectrum (i.e. multiple peaks). However, for Lidar2, whose response function at the probing distance is more dominated by the laser linewidth, we observe a smearing effect of the actual wind speed distribution. This effect is an additional concern when using a relatively broader linewidth light source for coherent lidar systems. In general, the response function can be approximated as a delta function if the lidar probing distance is within its coherence regime, assuming no limitations from the electronics, while the bandwidth of the response function approaches the FWHM of the self-heterodyne spectral width (2.7 MHz in our case) when the probing distance falls outside the coherence regime.

The relation between radial wind speed v_r, and Doppler frequency can be expressed as $v_r = \nu_d(\lambda/2)$. The highlighted time frames in Fig. 4.5 ($t = 20.8\ s$ and $t = 23.2\ s$) are illustrative of the different instrument responses between the two sensors. Fig. 4.5 also demonstrates how the signal strength can vary depending on the velocity components in the wind profile. Under laminar wind flow (t = 23.2 s) the signal peak strength of Lidar1 is superior; however, when the wind profile is more turbulent ($t = 20.8\ s$) the difference decrease significantly. From the plot for $t = 23.2\ s$, we can make an estimate of the response function width for Lidar2 assuming that the wind profile can be approximated as a delta function. The obtained FWHM response width for Lidar2 is $\sim 2\ m/s$, corresponding to ∼2.6 MHz in frequency. This result is well consistent with the measured response width using the hard target setup.

In general, a wind profile contains velocity components spanning over a couple of MHz in Doppler shift. Effectively, this circumstance reduces the benefit of using a very narrow linewidth laser in a CW lidar. To quantitatively evaluate the performance between Lidar1 and Lidar2, the signal strengths of both data sets in Fig. 4.5 are plotted as a function of time. The results are displayed in Fig. 4.6. In terms of peak values, Lidar1 does perform better. However, the average performance (marked with the thin dotted lines) between Lidar1 and Lidar2 only shows a ratio of 1.73, despite the large difference in their response function widths. Since

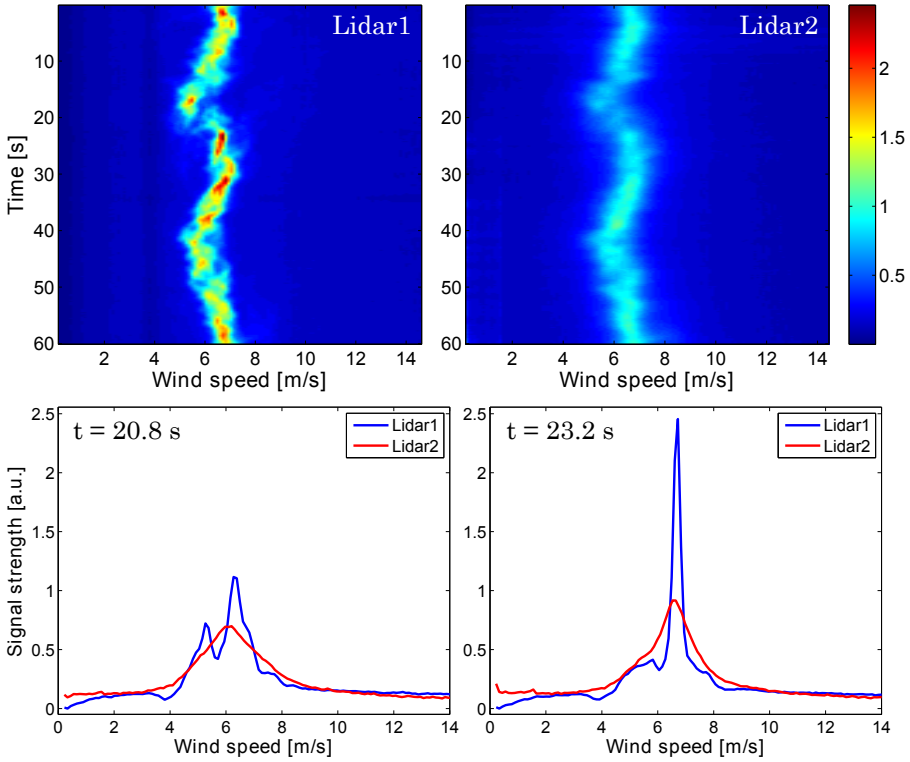

Figure 4.5: *Wind data from Fig. 4.4 after subtracting a time-varying background, along with data points from two specific time frames for both Lidar1 and Lidar2. At $t = 20.8$ s, the wind profile contains several velocity components, while it is laminar at $t = 23.2$ s.*

the average peak value is 73% higher in Lidar1, we expect it to maintain high data availability compared to Lidar2 if the particle concentration in the atmosphere is decreased. However, if Lidar2 is able to keep its data availability close to 100% (as we will show in the field test results below), both sensors should perform almost equally well for most wind speed measurement applications.

In Fig. 4.7, wind data series for a duration of 50 min are shown for Lidar1 and Lidar2 including the sonic anemometer data as reference. Figure 4.7(a) shows that both lidars have nearly 100% data availability. There are only a few dropouts in the data sets (denoted by data points lying on the time-axis). Further, we can observe a very high wind data correlation between the two lidar systems, $r^2 = 0.965$ at 2 Hz update rate, where r^2 is the coefficient of determination of a linear fit to the Lidar2 wind speed data plotted against the Lidar1 data.

Both lidar data series are compared with the corresponding sonic anemometer data; see Fig. 4.7(b) and Fig. 4.7(c), giving a further confirmation that the lidars are accurately measuring the temporal evolution of the radial wind speed. The correlation between each lidar and the sonic anemometer is not as high as the correlation between the two lidars because the lidars are not pointing directly at the sonic sensor. Additionally, a low-pass filtering is expected in the lidar data due to spatial volume averaging [53] (i.e., the lidar is measuring in an elongated volume

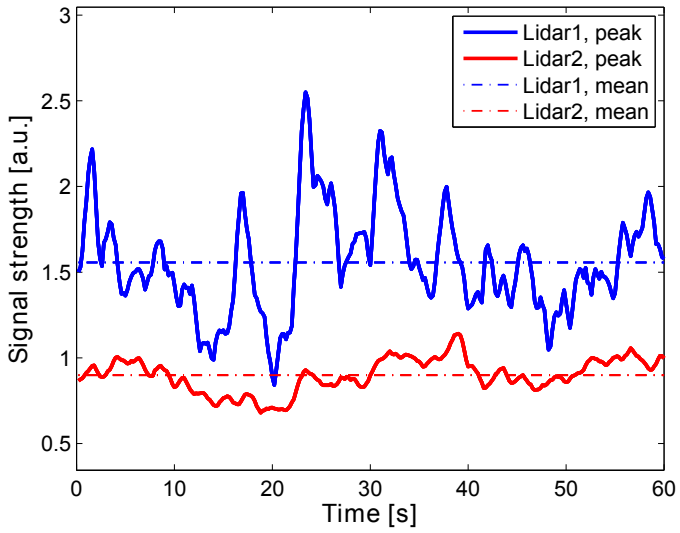

Figure 4.6: *Strength of wind signals from Fig. 4.5 as a function of time. The solid lines represent the peak values of the wind signals, while the dotted lines are the peak signal averages.*

while the in situ sonic sensor measures at a more confined position).

In this work we have compared the field performance of a CW coherent lidar probing at a distance within coherence regime (Lidar1) and another measuring outside the coherence region (Lidar2). We have experimentally demonstrated that Lidar2 is capable of measuring the wind profile at a probing distance which is at least a factor of 2.4 of the coherence range. The conventional requirement of narrow linewidth lidars (kHz regime) in wind speed measurements can be relaxed significantly, if PIIN is sufficiently suppressed. The lidar performance is dependent on the instrument response, and it generally varies with the probing distance beyond the coherence regime. At a selected probing distance, the instrument response width needs to be smaller or comparable to the relevant spectral features of the target speckle fluctuation. In the (average) wind speed measurements shown in this Letter, an instrument response width of a couple of MHz at the 85 m probing distance is sufficient, due to the non-laminar nature of the wind profile (speed distribution width $\geq 2\,m/s$). No considerable performance difference was found between Lidar1 and Lidar2 in terms of the consistency of their radial wind speed time series. The increased laser linewidth simply results in a tolerable smearing of the wind spectra.

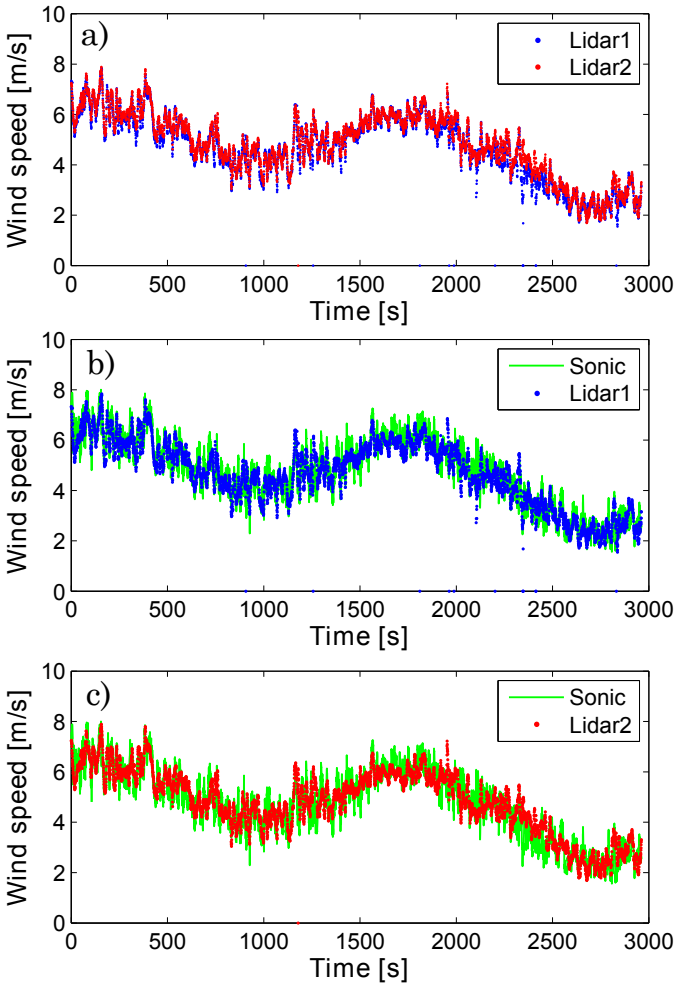

Figure 4.7: *Wind speed comparison between Lidar1, Lidar2 and the sonic sensor over a period of 50 min. The temporal resolution is 0.5 s and the correlation values for the different cases are: (a)* $r^2 = 0.965$ *, (b)* $r^2 = 0.833$ *and (c)* $r^2 = 0.862$ *. The experiment was performed during a clear, sunny afternoon at the DTU lidar test site in Roskilde, Denmark.*

4.4 Spectral Content of Lidar Signal

As discussed in Chapter 2, both the signal power and the signal bandwidth affect the SNR. Recalling Eq. 2.12 and, that the RIN can be ignored when using a semiconductor light source; the SNR of our system can be expressed as

$$\mathrm{SNR} = \frac{1}{B}\frac{2\rho_0^2 P_{\mathrm{LO}} P_s}{2e\rho_0 P_{\mathrm{LO}} + S_{dark}R_e^{-2} + 2\rho_0^2 P_{\mathrm{LO}} P_{stray}\tau_d^2 \Delta\nu} \tag{4.3}$$

It is clear from the expression, that the SNR will decrease with increasing signal bandwidth, B. This representation assumes that the spectral distribution of the signal is top hat shaped, but it is obvious from the wind data shown in Fig. 4.5, this is not the case. Thus, a better representation is

$$\mathrm{SNR} = \frac{1}{B}\frac{2\rho_0^2 P_{\mathrm{LO}} P_s \int S_{\mathrm{sig}}(\nu)\,\mathrm{d}\nu}{2e\rho_0 P_{\mathrm{LO}} + S_{dark}R_e^{-2} + 2\rho_0^2 P_{\mathrm{LO}} P_{stray}\tau_d^2 \Delta\nu} \tag{4.4}$$

where $S_{\mathrm{sig}}(\nu)$ is the distribution function of the signal spectral content and

$$\int S_{\mathrm{sig}}(\nu)\,\mathrm{d}\nu = 1. \tag{4.5}$$

To first order, the $S_{\mathrm{sig}}(\nu)$ of the wind signal can be approximated by a triangle. In this case, the SNR can be expressed as:

$$\mathrm{SNR} \simeq \mathrm{SNR}_{peak} = \frac{S_{\mathrm{sig}}(\nu_{peak})}{2}\frac{2\rho_0^2 P_{\mathrm{LO}} P_s}{2e\rho_0 P_{\mathrm{LO}} + S_{dark}R_e^{-2} + 2\rho_0^2 P_{\mathrm{LO}} P_{stray}\tau_d^2 \Delta\nu} \tag{4.6}$$

where ν_{peak} is the frequency of the signal peak. For delta-function-like lidar signals, Eq. (4.3) and (4.6) approaches the same value.

Assuming laminar flow – the Doppler spectral of the wind is a delta function – the laser linewidth will dictate the PSD of the lidar signal. To the first order, the peak of the signal PSD, $S_{\mathrm{sig}}(\nu_{peak})2\rho_0^2 P_{\mathrm{LO}} P_s$, is inversely proportional with the laser linewidth. Hence in the experiment presented in the previous section, we could expect a difference between Lidar1 and Lidar2 by a factor of 13.5 due to their laser lineshape difference. But it is clearly not the case based on the data shown in Fig. 4.8, where the lidar signal peak values are shown for both systems. In the experiment, the lidar signal power should be similar for Lidar1 and Lidar2, which is also supported by the data (dashed lines) in Fig. 4.8. The dashed lines represent the total lidar signal power for Lidar1 and Lidar2. They are obtained by taking the integral of the signal PSD shown in Fig. 4.5, where the noise background has already been subtracted. This means that the solid lines are proportional with the SNR_{peak} of the systems, see expression (4.6).

The lidar signal PSD is a convolution between the spectral contents of the wind speed distribution in the probe volume and the laser linewidth. Thus, the only explanation of this reduced penalty in SNR_{peak} is because the Doppler spectral

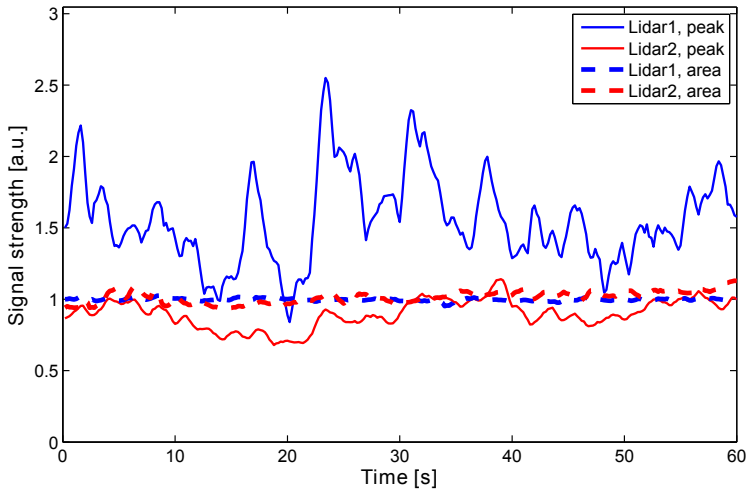

Figure 4.8: *Lidar signal generated from the wind data presented in Fig. 4.5. The solid lines are the same peak values as shown in Fig. 4.6, the dash lines are the total lidar signal power, $2\rho_0^2 P_{\mathrm{LO}} P_s R_e^2$, which have been renormalized to a value around 1.*

bandwidth of the measured wind field is comparable to the laser linewidth of Lidar2 and the variation of the PSD peak values is due to the Doppler spectral bandwidth variations. It is also evident from the data presented in Fig. 4.5, that the wind distribution are nowhere close to a delta-function. Note that Doppler spectral bandwidth is affected by the probe length, so if probe length decreases e.g., from reducing the focus distance, the SNR_{peak} difference between Lidar1 and Lidar2 will start to increase.

5 Multi-Beam Steering

Generally, the wind turbines are not big enough to escape the atmosphere boundary layer where the mean wind speed increases with the altitude; but the wind direction variations in different heights should be small. Thus, for lidar assisted turbine control, two measurement points at the hub height should be sufficient for yaw control. Since the yawing time scale is relatively slow (10 min), the data acquisition rate of the lidar can be quite relaxed.

Unlike the yaw control, pitch control of the turbine blades happens at a much faster time scale (seconds), and requires wind shear information. Thus, at least three measurement points are needed. Recent study showed that proper control system containing pitch control might reduce the load up to 50% for extreme wind gusts and 30% for lifetime fatigue loads without negative impact on overall energy production [54]. In 2012, field test of collective pitch control using nacelle-based lidar was conducted by Schlipf et al. [55]. They showed that lidar-assisted collective pitch control is a promising concept, also under real conditions.

In this chapter, we present two different approaches to generate multiple LOS in order to provide enough measurement points for either yaw or pitch control of wind turbines. Existing lidar scanning systems usually rely on a mechanical scanning head [56], but the wind turbines are designed to last at least 20 years [57, 58], so it will be ideal if the nacelle-mounted lidar has the same life time. For this reason, the two beam steering methods presented here are designed to minimize the mechanical tear and wear – no bulky mechanical scanning system, that requires a lot of maintenance compared to 20 years operation time.

5.1 Liquid Crystal Retarder

In this design, the system employs two fixed-focus transceiver telescopes for launching laser beams interchangeably into two horizontal LOS with a 60-degree separation angle. The measured radial speeds, v_{LOS1} and v_{LOS2}, allow the estimation of both magnitude and direction of the wind vector in the horizontal plane. The time sharing between the two LOS is achieved through polarization control using a controllable liquid crystal retarder (LCR), a polarization beam splitter, and a pair of mirrors. This design is described in more details in my publication [59] and this section is a recap/reproduction of the instrumentation part of [59].

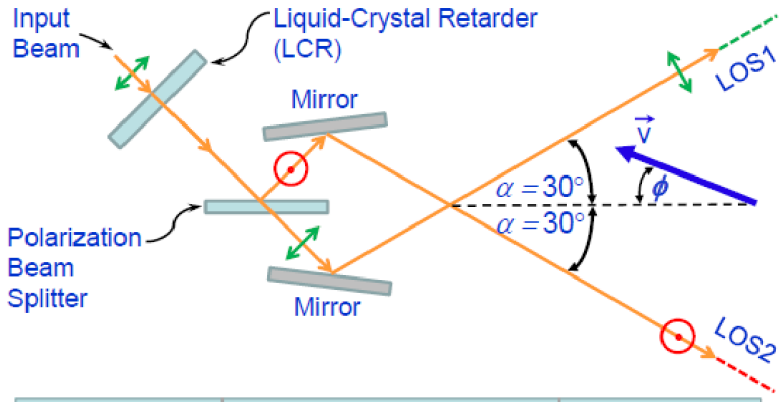

LCR Voltage	LCR Output Polarization	Active Beam
~1.5 V (rms)	⊙ s-polarized	LOS2
25 V (rms)	↕ p-polarized	LOS1

Figure 5.1: *Non-mechanical beam-steering system with a liquid-crystal retarder (LCR). The LCR is electronically addressed to either preserve the input beam polarization state (linear p-polarized for high LCR drive voltage) or change it to its orthogonal counterpart (linear s-polarized for low drive voltage). p-polarized (/s-polarized) beam is transmitted through (/reflected from) the polarization beam splitter and deflected by a mirror to activate LOS1 (/LOS2). Both LOS1 (green dash line) and LOS2 (red dash line) are at 30° angle with the lidar axis (black dash line). A blue arrow illustrates a possible orientation of the wind velocity vector $\overline{v}$ with an azimuthal direction ϕ relative to the lidar axis. From my publication [59]*

Figure 5.1 illustrates the working concept of the design. The LCR acts as a half-wave plate when a 2 kHz square wave drive voltage, ~ 1.5 V (rms), is applied. The input p-polarized beam is unchanged by the LCR and transmits through the beam splitter if the drive voltage is 25 V (rms). Thus, measurement of v_{LOS1} is activated by the low LCR voltage while measurement of v_{LOS2} gets triggered by the high LCR voltage. For every pair of v_{LOS1} and v_{LOS2}, the magnitude $|\overline{v}|$ and direction ϕ of the wind velocity can be determined by the following equations

$$|\overline{v}|\cos\phi = \frac{1}{\sqrt{3}}(v_{\mathrm{LOS1}} + v_{\mathrm{LOS2}}), \quad |\overline{v}|\sin\phi = v_{\mathrm{LOS1}} - v_{\mathrm{LOS2}} \tag{5.1}$$

The laser beam is switched between the two LOS every half a second. To evaluate the switching characteristics of the system, the optical power of the beam transmitted out of the two telescope exit apertures are measured. The alternating modulation of the beam power for LOS1 and LOS2 is shown in Fig. 5.2 along with corresponding LCR voltage. These results show that the switching time constants to reroute the transmitted beam from LOS1 to LOS2 is longer ($\tau_{12} = 16$ ms) than for the opposite direction ($\tau_{21} = 100\ \mu$s). It is worth to note that next-generation

LCRs with stabilizing polymer materials are already commercially available and can provide switching speeds in the order of 100 μs in both directions. Nonetheless, the present asymmetry in the switching time is not critical, since the update rate is in the order of 1 Hz for wind field magnitude and direction measurement.

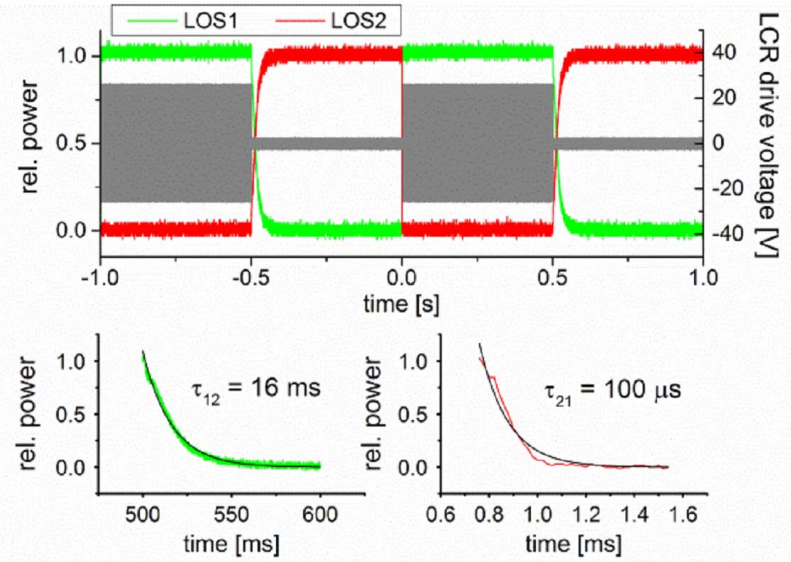

Figure 5.2: *(Top) Measured relative power of the laser beam versus time, alternately transmitted along LOS1 (green) and LOS2 (red), along with the corresponding LCR drive voltage (gray) that enables this non-mechanical lidar beam-steering mechanism. (Bottom) Time constants for switching the beam from LOS1 to LOS2 and vice versa (i.e. τ_{12} and τ_{21}) are estimated by fitting exponential decay curves to the relative beam power transitions at 0.5 s and 0.0 s, respectively. The measurements were performed at an ambient temperature of 25 °C. From my publication [59]*

A field-programmable gate array (FPGA) unit is used to perform real-time lidar spectral analysis. The FPGA continuously calculates PSD of the photodetector signal every 6.83 μs (a sampling rate of 75 MHz consisting 512 sample points) and averages a few thousands of these spectra to produce 33 Hz PSD plots regardless of the LCR's state. It was observed that some 33 Hz PSD, generated at times very close to the switch transitions, contain two Doppler peaks that originate from both LOS1 and LOS2 measurements. This ambiguous situation (or crosstalk) occurs often for the slow transition (LOS1 to LOS2) but is also observed in the opposite switch direction. Figure 5.3 shows an example of such crosstalk. To mitigate this issue, a filtering algorithm is introduced which simply drops two 33 Hz PSD plots for every switching event – one before and one after a transition.

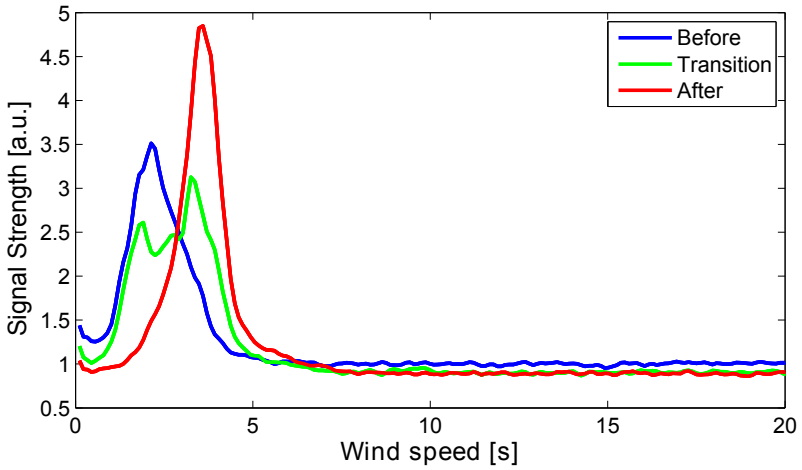

Figure 5.3: *An illustration of double Doppler peak in the wind spectrum due to the LCR crosstalk. The blue curve is the wind spectrum just before the LCR switching, the green curve is during the transition, and the red curve is after the transition.*

5.2 MEMS Scanning Mirror

In the next section, we present an approach where a micro-electro-mechanical-system scanning mirror (MEMS-SM) is deployed to steer the probe beam into multiple optical transceivers. Due to its small size, MEMS-SM is not subject to the same mechanical wear and tear as the conventional scanning systems, and it is typically specified with >1 billion switch cycles of operation. Compared to the LCR concept [59], presented in the previous section, the MEMS-SM has the advantage of having a lower insertion loss. The difference is not significant in yaw control applications, where only 2 LOS are needed. But for pitch control, the LCR method requires the the transmitted beam to pass through multiple LCR units – thus increasing optical insertion loss and wavefront aberration that ultimately degrade the lidar's sensitivity.

Besides the lower insertion loss, compared to the LCR concept, the MEMS-SM also has other features such as wavelength and polarization independence, which could be utilized to improve future system design. Another useful feature of the MEMS-SM is the capability of continuous scan in 2D, enabling active spatial dithering to reduce the mean irradiance of the beam focus. It can be helpful when addressing possible eye safety issues. The working concept and system specific characteristics such as switching time and robustness are presented in my publication in Optics Express 2016 [60], along with details regarding the spatial dithering of the beam focus. The publication has been reformatted and is presented in the next section.

5.3 Eye-safe Diode Laser Doppler Lidar With a MEMS Beam-scanner

We present a novel Doppler lidar that employs a cw diode laser operating at 1.5 μm and a micro-electro-mechanical-system scanning mirror (MEMS-SM). In this work, two functionalities of the lidar system are demonstrated. Firstly, we describe the capability to effectively steer the lidar probe beam to multiple optical transceivers along separate lines-of-sight. The beam steering functionality is demonstrated using four lines-of-sight — each at an angle of 18° with respect to their symmetry axis. Secondly, we demonstrate the ability to spatially dither the beam focus to reduce the mean irradiance at the probing distance (R = 60 m) of each line-of-sight — relevant for meeting eye-safety requirements. The switching time of the MEMS-SM is measured to be in the order of a few milliseconds. Time-shared (0.25 s per line-of-sight) radial wind speed measurements at 50 Hz data rate are experimentally demonstrated. Spatial dithering of the beam focus is also implemented using a spiral scan trajectory resulting in a 16 dB reduction of beam focus mean irradiance.

Introduction

Since 1970s, coherent laser radars (also known as Doppler lidars) for wind velocimetry have been mostly limited to scientific use due to lack of inexpensive laser sources with appropriate optical power, wavelength and coherence. The potential of laser based wind sensors in industrial applications, e.g. in wind energy industry, has been greatly enhanced by the use of cost-efficient semiconductor laser sources operating at 1.5 μm [18, 19]. Previously, we have improved our diode laser based lidar wind sensor by incorporating an electronically controlled liquid-crystal retarder (LCR) as means to switch the beam direction between two lines-of-sight (LOS) [59]. This equips the low-cost lidar with the capability to measure not only the magnitude but also the direction of a 2D wind vector, assuming a relatively laminar wind flow. It makes the lidar system useful for applications like wind turbine yaw control [61]. By increasing the number of LOS and hence the velocity components that can be obtained, the lidar functionality can extend to wind shear measurement or perhaps even blade pitch control of wind turbines [54]. Existing lidar scanning systems either rely on a mechanical scanning head [56] or integrate the lidar inside the turbine spinning hub [62]. Due to mechanical wear and tear, the scanning head has a limited operational lifetime, making it undesirable from an industrial point of view. In principle, the spinning lidar [62] does not necessarily require any mechanical beam-scanner from the lidar itself, but the lidar's integration inside the spinning hub is more complicated than the installation of nacelle-mounted lidars that are easier to retrofit in existing turbines. One could use a variant of the LCR based wind lidar [59] to generate more than two LOS. However, the method entails that the transmitted beam passes through multiple LCR units – thus increasing optical insertion loss and wavefront aberration that ultimately degrade the lidar's sensitivity (signal-to-noise ratio).

In this work, we demonstrate an alternative solution to create multiple LOS in our 1.5 μm semiconductor laser lidar system. The proposed method has the advantage of simplicity, low insertion loss, low power consumption, and wavelength- and polarization-independent operation. Only one optical switching device is utilized which leads to reduced footprint and low cost for the lidar system. This novel method relies on a single dual-axis micro-electro-mechanical-system scanning mirror (MEMS-SM) [63]. The use of a two-axis MEMS-SM enables angular deflection of the lidar beam ($\pm 15^\circ$ optical deflection for each axis) to several LOS — the number of LOS is limited by the size of optical transceivers that can fit within a given footprint. The MEMS-SM is specified with > 1 billion switch cycles of operation. Furthermore, the MEMS-SM can be used to spatially dither the beam and potentially reduce the mean irradiance down to a prescribed eye-safe level at the focal plane. In the following sections, we describe the two MEMS-SM functionalities and demonstrate the operation of the lidar system by measuring multiple (four LOS) radial wind speed components.

Lidar configuration based on a MEMS scanning mirror

Figure 5.4(a) shows the geometrical configuration of the probing directions in our "multiple-beam" lidar system if mounted on the nacelle of a wind turbine to preview the approaching wind. The lidar transmitted beam is time-shared among the four LOS. Speed component along each LOS is measured for 0.25 s in each cycle in our demonstration. The schematic diagram of the lidar system itself is shown in Fig. 5.4(b) where only two of the four LOS are shown. A fiber-coupled cw diode laser with ~ 500 mW of optical power operating at wavelength $\lambda = 1.5\mu$m is used. The laser beam is transmitted through a single-mode fiber into an optical circulator that taps a tiny fraction ($\sim 0.1\%$) of the laser power and directs it to the detector as a local oscillator. A Doppler shifted backscattered radiation from aerosol in the probe volume coherently mixes with the local oscillator resulting in a detector beat signal that oscillates at a mean Doppler shift frequency f_D. The field-programmable gate array (FPGA) board calculates the power spectral density (PSD) from 512-point time series (100 MHz sampling) of the ac-coupled detector signal. Averages of the spectra are produced to estimate at 50 Hz rate the radial wind speed v_{LOS}:

$$v_{\mathrm{LOS}} = \frac{\lambda}{2} f_D \tag{5.2}$$

The proposed lidar uses a dual-axis MEMS-SM (mirror diameter = 3 mm). Beam steering to multiple LOS relies on the 2D scanning feature of the MEMS-SM using its point-to-point scanning mode. The switch time between successive LOS impacts data availability and limits the effective acquisition rate – making it an important parameter to characterize. The MEMS-SM controller contains a low-pass filter (i.e. 6^{th} order Bessel filter with a programmable cutoff frequency) for each axis drive input to reduce the mirror's mechanical oscillations that result from a step input signal [64]. In order to characterize the MEMS-SM switching speed, the time-domain

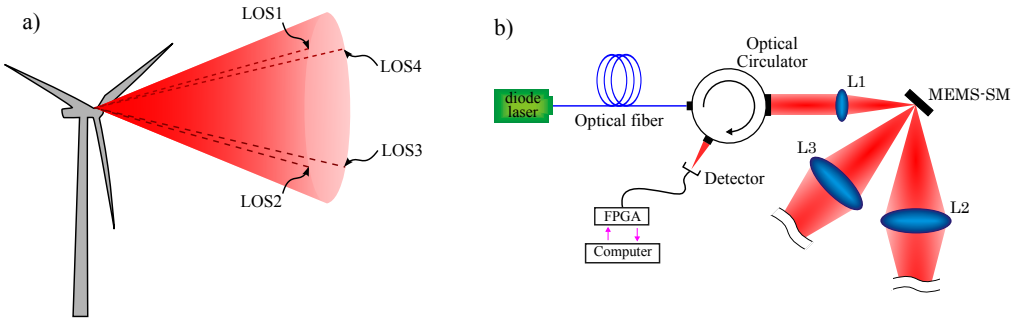

Figure 5.4: *(a) Geometry of the four lines-of-sight (LOS) of the lidar. The half cone angle is* 18°. *LOS1, LOS2, LOS3 and LOS4 represent the optical axes of four optical transceivers. On each LOS, the lidar beam is focused at a probing distance* $R = 60$ *m resulting in a Rayleigh length of 5 m. The beam is alternately focused to positions that form the vertices of a square. (b) Schematic of a multiple LOS (time-shared) lidar based on a MEMS-SM. The custom-built optical circulator consists of a polarizing beam splitter plate and a 45-degree Faraday rotator. The collimated output of the circulator has a beam diameter of 2 mm. For brevity, only two optical transceivers are shown in the sketch. L1: aspheric lens* ($f_1 = 8$ *mm). L2 and L3: 3-inch diameter doublet lenses* ($f_2 = f_3 = 216$ *mm).*

step-response was measured for different low-pass cutoff frequencies ranging from 40 Hz to 200 Hz. The results are shown in Fig. 5.5(a). To make the measurement more precise, the optical power transmitted through the transceiver doublet lens is refocused by an identical lens into a 1 mm on-axis pinhole at the focal plane in front of a detector as in Fig. 5.5(b). Optical power fluctuations caused by the mirror oscillations in response to a step input are sufficiently reduced to within of the steady-state (high) value at a cutoff frequency of 80 Hz or less. Based on the results in Fig. 5.5(a), all the measurements in the following sections were conducted using a filter cutoff frequency of 80 Hz, which gives a rise time and fall time of 3.85 ms and 2.63 ms, respectively. Rise and fall times are defined as the temporal duration between 10% and 90% of the steady-state amplitude.

Radial speed measurements with 4 lines-of-sight

Field test for outdoor wind measurement is conducted using the 4-LOS lidar. The raw wind spectra – i.e. PSD but with the frequency axis converted to speed using Eq. (5.2) – are produced from 512-point fast Fourier transform (FFT) of the photodetector signal at a sample rate of 100 MHz. Figure 5.6(a) shows the 50 Hz averaged wind spectra as a function of time. The color intensity represents the normalized Doppler signal strength (i.e. the noise floor is unity). The staircase feature in the data (evident in the first few seconds) demonstrates that we are indeed measuring the wind in all four LOS in a time-shared fashion.

Each vertical trace in Fig. 5.6(a) corresponds to a 50 Hz wind spectrum. Back-

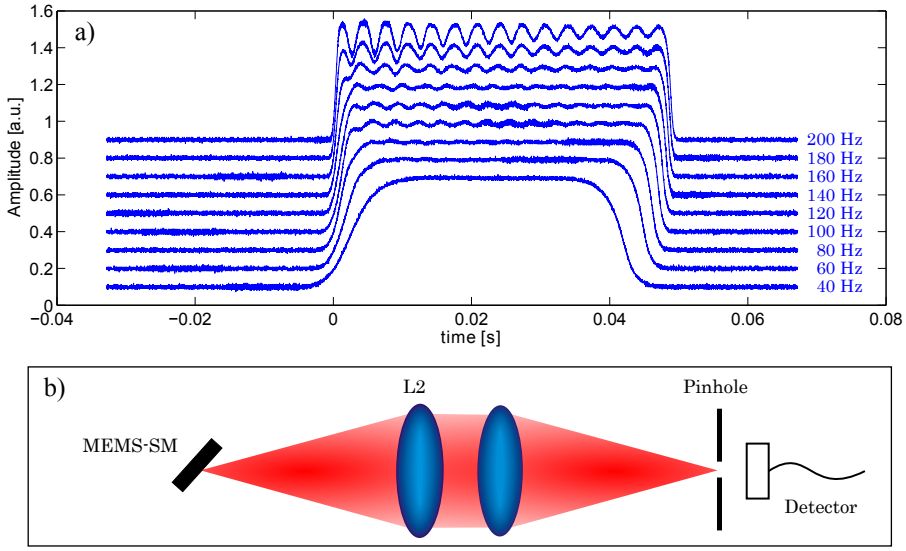

Figure 5.5: *(a) Step-response of the MEMS-SM for different input low-pass filter cutoff frequencies. For clarity, amplitude offsets of 0.1 to 0.9 are introduced to separate the curves. The amplitude represents the relative optical power the MEMS-SM is able to send through one doublet lens (e.g. L2) as it steers the lidar beam to successive LOS. (b) The setup used to probe the step-response of the MEMS-SM. Here the LOS of lens L2 was used. An identical doublet lens was placed in front of lens L2 to direct the optical power to an on-axis pinhole and a detector.*

ground noise measurements, shown in Fig. 5.6(b), were recorded by blocking the lidar beam. During the transition between two LOS, the spurious backreflection from the metallic material separating the doublet lenses is observed to cause a large signal peak at zero speed as seen in Fig. 5.6(b) and Fig. 5.6(c). In both cases, the recorded spectra immediately before (blue) and after (green) the transition spectra are shown. As observed, there are no signs of spurious peak in these spectra. This suggests that the switching time is indeed shorter than the 20 ms duration required to produce one averaged wind spectrum. The result agrees well with the MEMS-SM characterization shown in Fig. 5.5(a).

As shown in Fig 5.6(a), it is possible to visually discriminate the four LOS speeds while there are also occurrences where the radial speeds are similar to each other. Thus, further data processing is needed before the data is practically useful. An average wind speed is extracted from each 50 Hz wind spectrum using a simple peak-finding algorithm. The results are shown in Fig. 5.7. Since the data acquisition is not synchronized with the MEMS-SM steering control, the transition spectra can be either at the beginning or the end of each LOS data block. For this reason both the first and the last data point in each 0.25 s block are discarded, and the remaining data (i.e. about 80% duty cycle) are average into 1 Hz wind data for each LOS. The processed 1 Hz wind data are also presented in Fig. 5.7. It is also evident from

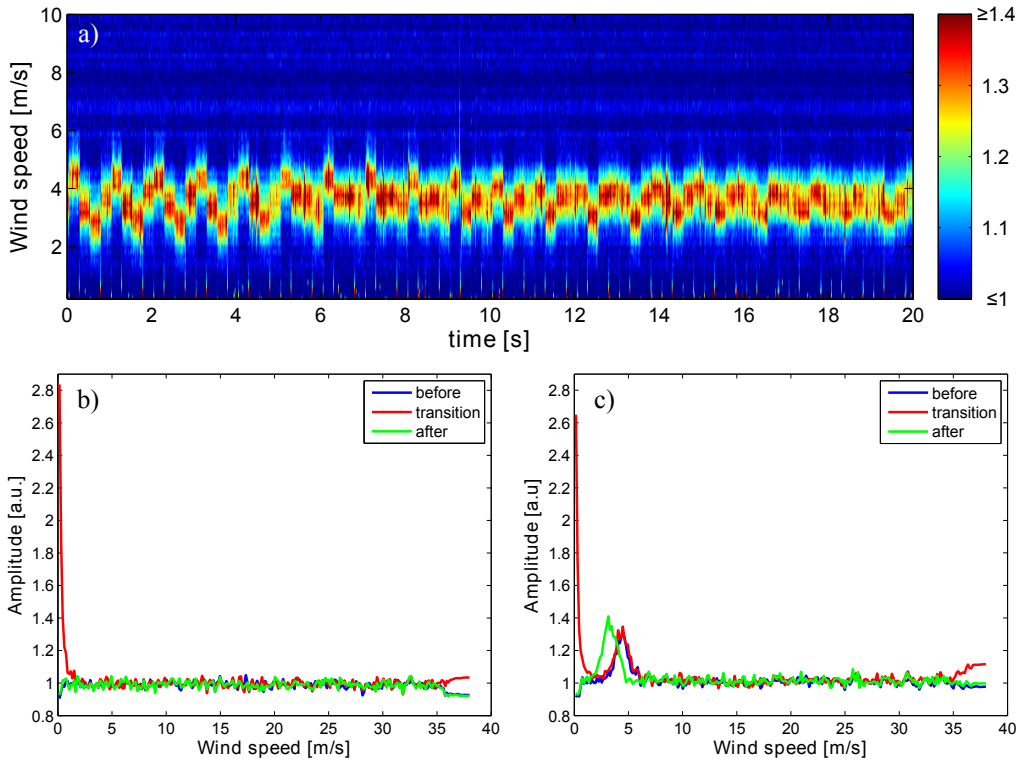

Figure 5.6: *(a) Sample wind spectra over 20 seconds at 50 Hz update rate. The color scale to the right denotes the Doppler signal strength normalized by the local oscillator dominated noise floor. (b) The background spectra of the lidar system when the probe beam is blocked. (c) Wind measured by the system before, during, and after a LOS transition. The red curves in (b) and (c) are the transition spectra between two LOS, while the blue curves are the spectra just before the transition and the green curves are the ones immediately after the transition.*

Fig. 5.7, that discarding the transition spectra is necessary to avoid errors. Note that future synchronization of data acquisition and steering control, and the use of a peak-finding algorithm that discards spurious peaks in wind spectra can increase the duty cycle or data availability of the system.

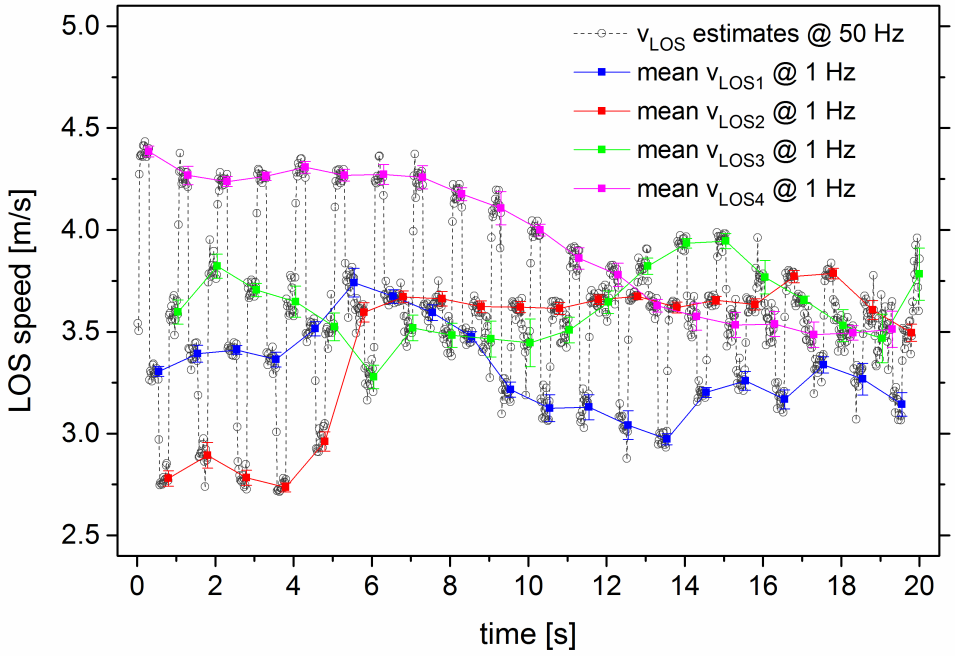

Figure 5.7: *The gray curve represents the wind data generated directly from the raw data in Fig. 5.6(a) using a LabVIEW peak-finding algorithm. The other curves represent the average radial wind speed in the four respective LOS where each data point is an average of 10 to 11 points from the 50 Hz radial speed data but excluding potentially erroneous data that correspond to transition spectra like the one shown in Fig. 5.6(c).*

Spatial dithering to reduce the average irradiance of beam focus

In this section, we describe another elegant utility of the MEMS-SM that improves the ability of our lidar system to satisfy eye-safety requirements. The method relies on the active spatial dithering of the focused beam at a remote range R (tens of meters or more) so that it wanders over a larger area and effectively reduces the time-averaged irradiance (and hence the averaged energy density) during the exposure time. Since the needed area over which the beam is spatially dithered is much smaller in dimension compared to R, the influence of dithering on the radial speed measured by the lidar is extremely small and thus negligible.

A spatial dithering method has been conceptually proposed in a patent [65] but does not specifically disclose the use of a MEMS-SM. The optical geometry we propose here is also different. As shown in Fig. 5.8, the MEMS-SM is placed between the two telescope lenses of each optical transceiver (e.g. between L1 and L2). Furthermore, we describe how the MEMS-SM is able to apply a sufficient amount of spatial dither using a ray transfer matrix model.

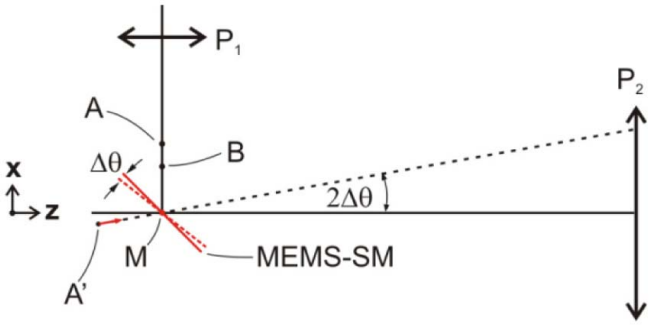

Figure 5.8: *Schematic diagram showing the relative positions of the MEMS-SM plane, planes P_1 and P_2 of lenses L1 and L2, respectively. Point A is where a collimated input beam is focused by lens L1. Point B indicates the focal point of lens L2. By pivoting at point M, the mirror deflects the beam either aligned with the optical axis of L2 or off-axis.*

Consider the optical geometry in Fig. 5.8, which takes the case of the LOS defined by the optical axis of lens L2 in Fig. 5.4. Planes P_1 and P_2 indicate the locations of lens L1 and L2, respectively. An input collimated beam gets focused by lens L1at point A displaced from the focal point B of lens L2. An image of this focus at a far distance R to the right of plane P2 is formed by lens L2 where the object distance is $\left(f_2+\overline{AB}\right)$ where $\overline{AB} \ll f_2$. The thin lens formula gives the approximate image distance R for the object (focus) at point A for the optimally aligned case where $\Delta\theta = 0$, that is, the input ray vector is $(0,0)$. If spatial dithering is applied, a small angular deflection $\Delta\theta$ of the mirror is introduced. This corresponds to having the object originate from a virtual point A' in Fig. 5.8 (i.e. $\overline{AM} = \overline{A'M}$) with an input ray vector $\left(-2\overline{AM}\Delta\theta, 2\Delta\theta\right)$. Using ray transfer matrix analysis and assuming small mirror deflection $\Delta\theta$ and $R \gg f_2$, the lateral displacement r_{out} at R

is calculated as:

$$r_{out} = \left(x_{out}^2 + y_{out}^2\right)^{1/2} = \frac{2R\overline{AM}}{f_2}\Delta\theta. \tag{5.3}$$

Note that as $\overline{AM} \to 0$ or as the beam focus is brought closer to M, $r_{out} \to 0$, which emphasizes our design criterion that the beam focus formed by lens L1 must not lie on the scanning mirror surface. $\overline{AM}$ also has an upper limit that increases with the diameter of the scanning mirror used. For a given mirror diameter, $\overline{AM}$ must not be too large in order to avoid significant beam truncation.

For the settings we used where $R = 60$ m, $\overline{MP_2} = 212$ mm and $\overline{BM} = 4$ mm, we find $\overline{AM} = \overline{AB} + \overline{BM} = 4.78$ mm. This is a sufficient value that avoids undesirable truncation of the beam incident on the mirror and results in a satisfactory $r_{out}/\Delta\theta$ ratio of 2.7 mm/mrad (for $f_2 = 216$ mm). This enables us to spatially dither the beam using a spiral trajectory shown in Fig. 5.9(a) over a circular region of 7 mm radius with a maximum mirror deflection of only 0.15 degree. Before applying spatial dither, the on-axis beam focused at R is approximately described by a Gaussian irradiance profile of radius $\omega_0 = 1.56$ mm (measured by a beam profiler) as shown in Fig. 5.9(b). To estimate the effective irradiance for the spatially dithered case, we calculated the sum of Gaussian profiles each centered on coordinate points of the spiral trajectory divided by the number of Gaussians. The result shown in Fig. 5.9(c) illustrates that the mean irradiance resulting from spatial dithering is 40 times less than that at the center of a stationary beam. The initial frame of a short movie clip of the focused beam at $R = 60$ m being scanned in a spiral pattern is shown in Fig. 5.10. This result illustrates the potential to reduce the mean irradiance using a MEMS-SM based dithering method.

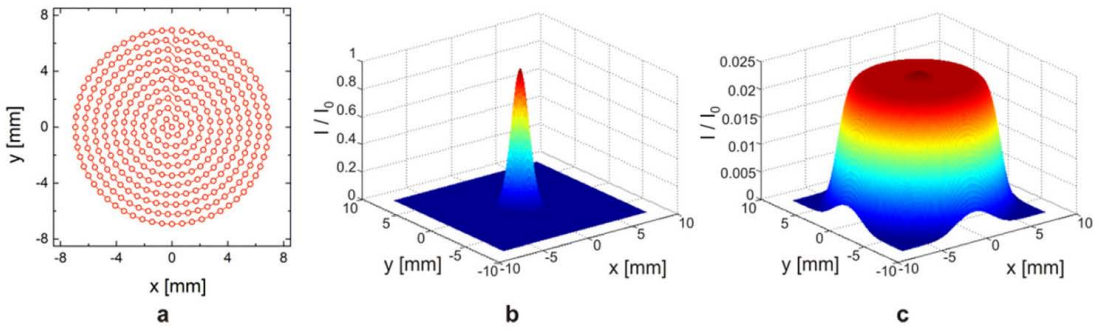

Figure 5.9: *(a) Spiral trajectory used for spatial dithering of the beam on the xy-plane. Simulated mean irradiance profiles at $R = 60$ m for the case (b) before, and (c) after applying the spatial dither. I_0 is the peak irradiance of the stationary Gaussian beam.*

Figure 5.10: *First video frame of the spatially dithered focused beam ($\omega_0 = 1.56$ mm) at probe range $R = 60$ m. The video (see **Visualization 1**) is slowed down four times the original speed to show the beam's spiral trajectory.*

Robustness of the MEMS-SM

The manufacturer specified operating temperature of the dual-axis MEMS-SM is $-40\,^{\circ}C$ to $+120\,^{\circ}C$. However, its superb positional repeatability of 0.0005° is only specified at room temperature. In our current optical configuration with the probing beam focus at 60 m and $r_{out}/\Delta\theta$ ratio of 2.7 mm/mrad, the specified positional repeatability corresponds to a transverse position accuracy of 24 μm for the remote beam focus. The effect of large ambient temperature variation on this positional performance remains to be tested. Nevertheless, the lidar head housing that encapsulates the MEMS-SM together with other optical components contains a temperature sensor and heating elements to enable a rudimentary regulation of the enclosure's internal temperature (room temperature $\pm 5\,^{\circ}C$) for most outdoor conditions.

According to specifications, the Al or Au coated mirror of the MEMS device can handle incident optical powers up to 1 W across a broad wavelength range. Although a specification of damage threshold in units of W/cm^2 is needed to assess an incident beam of specific width or profile, we consider the 500 mW laser power (at 1.5 μm wavelength) used in our system to be below the limit. This is validated by the fact that no laser induced thermal effects on the MEMS-SM were observed. As also described in the previous section, the laser beam is, by design, focused at a finite distance from the mirror surface to achieve an adequate ratio for spatial dithering — effectively reducing the power density of the incident beam on the mirror surface. Furthermore, the lidar head enclosure prevents or minimizes dust contamination to the MEMS-SM.

In contrast to bulk mechanical beam-scanners (e.g. Risley prisms or galvanometer scanning mirrors), the MEMS-SM has a dynamic component that is more robust to wear and tear due its ultra-low mass. MEMS-SM offers other advantages due to its mass-producible and low-power consumption features. With a typical specification of > 1 billion switch cycles, the MEMS-SM has a projected lifetime of a few decades -– matching the operational lifespan of a wind turbine.

Conclusion

We have demonstrated a novel semiconductor laser wind lidar with four time-shared lines-of-sight based on a MEMS-SM device. Radial wind speed data obtained from a field test have been presented, and it is clear that speed components along four LOS are distinguishable. Characterization of the MEMS-SM shows that the temporal step-response of the device is fast enough to satisfy our target radial speed acquisition rate of 50 Hz, which is relevant for applications such as wind turbine blade pitch control. Furthermore, we have demonstrated experimentally that the MEMS-SM is capable of spatially dithering the beam at the desired focal plane (at 60 m remote distance in our demonstration). This reduces the mean irradiance of the lidar probe beam at the focal plane – relevant for meeting eye-safety requirements. It is also worth noting that unlike the liquid-crystal based beam steering method, the use of MEMS-SM enables steering of an incident beam of any polarization state and any wavelength over a wide spectral range – features that have potential advantages in future variants of our lidar system. These include future designs that aim to further increase the number of measurement points to achieve a more detailed measurement of wind profiles by increasing the number optical transceivers used. As we mentioned in the first section, this will be constrained by the size of the optics. Note however that if a shorter wavelength is used with a MEMS-SM for beam steering and dithering, smaller focusing lenses can be utilized while keeping the same spatial resolution since Rayleigh length scales inversely with wavelength.

5.4 Wind Signal during Dithering

The spatial dithering described in the previous section, is only significant around the focus of the probe beam. Thus, the dithering should not have any noticeable impact on both the shape and the position of the weighting function. Figure 5.11 shows the measured wind data with dithering on and off through the same transceiver. There is no immediate difference on the spectral features between the two data sets. Unfortunately, no side-by-side data is available, but at least the data in Fig. 5.11 do support our claim of no significant wind signal distortion should occur from the dithering.

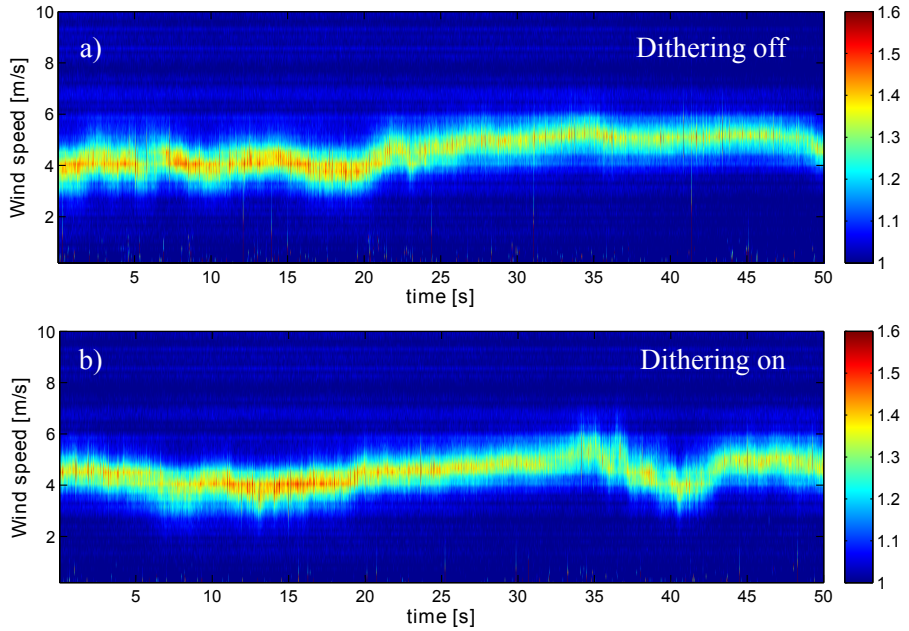

Figure 5.11: *Measured 50Hz wind data through the same transceiver telescope, a) MEMS dithering was switched off. b)Mems dithering was switched on. The wind data was taken within 2 minutes of each other.*

6 Field Tests

During the period of this project, my host company Windar Photonics has successfully commercialized an industrial wind lidar based on a CW all semiconductor light source at 1.5 μm, called *WindEye*. Many design choices were based on the research presented in the previous chapters.

The lidar system has 2 LOS with a horizontal angle separation of 60 degrees, and the beam steering concept is based on the polarization control shown in Section 5.1. 3 inch lenses are deployed as the exit lenses in the telescope design, since a relatively high spatial resolution can be obtained when the focus distance is below 100 m (see discussions in Chapter 3). The main application is for individual turbine yaw control and it is designed to be mounted on the turbine nacelle. The system itself contains two parts: an optical head (443 mm $\times$ 250 mm $\times$ 190 mm, 15 kg) and a control box (430 mm $\times$ 250 mm $\times$ 120 mm, 9 kg), and they are separated by a 10 m long cable. More details of the product can be found in [66] (Appendix B).

Different field tests of the WindEye lidar was conducted in order to evaluate the system performance up against the existing technologies e.g., sonic anemometers and fiber-laser-based CW CDL system, and the results are presented in this chapter. The WindEye units used in different experiments are not the same system, but randomly picked from the production. So the systems will be denoted with different numbers to distinguish between them.

6.1 Sonic Anemometers vs. WindEye

In this section, we present the results of a measurement campaign, designed to evaluate the lidar product, WindEye, using two USA-1 sonic anemometers with a standard sensor head (Metek Gmbh, Germany) as the reference instruments. The measurement campaign lasted for two months, and some of the result was presented in the ISARS conference 2014 in Auckland [67]. The slides of the presentation can found in Appendix C. My primary contribution in this campaign was to construct the instrument, the characterization of it, and technical support during the set-up, such as how to track the beam. The majority of the wind data analysis and sytsem evaluations were conducted by DTU Wind Energy, and the results can be found in [68].

In the measurement campaign, to minimize the measurement uncertainty, the

weighting function of WindEye1 was measured using the method described in Fig. 3.2. The results are shown in Fig. 6.1, and the weighting function peaks are estimate to be at 93 m and 84 m for LOS1 and LOS2, respectively. The probe length difference of the weighting functions of LOS1 and LOS2 correspond well with the quadratic dependence of the probe distance, as discussed in Section 3.2.

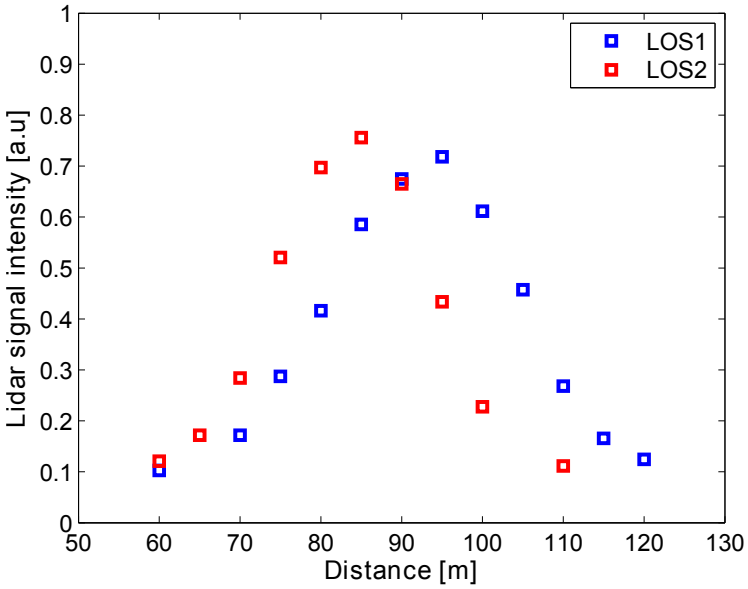

Figure 6.1: *The weighing function measurement results of WindEye1. For LOS1, the estimated weighting function peak is 93 m and the FWHW probe length is 29 m. For LOS2, the estimated weighting function peak is 84 m and the FWHW probe length is 23 m.*

The experiment was designed such, that the distance between the sonic anemometers and the lidar matches exactly to the respective weighting function peak positions of LOS1 and LOS2. The exact beam locations of both LOS were tracked by monitoring the lidar signal of a moving cardboard, and was then visually confirmed using an IR-detection card. Since the sonic anemometers were placed ~ 8 m above the ground, a moveable lift was required to track the beam. The actual location of the lidar beams were within 0.3 m of the measurement volume of the sonic sensors and the positions were further confirmed when the measurement campaign ended. Images of the actual experimental set-up can be found in Fig. 6.2. All three sensors are placed at a height of 8 m to avoid the turbulent wind fields close to the ground.

In general, the wind data between WindEye1 and the sonic sensors agree well throughout the whole measurement campaign, and there were no sign of system performance deterioration during the whole measurement period. Figure 6.3 shows the wind direction correlation between WindEye1 and the two sonic sensors. The wind direction measured by WindEye1 is determined based on the radial wind speeds according to Eq. (5.1). The presented data includes data from both the beginning and the end of measurement campaign. It is clear, that the data is consistent between the sonic sensors and WindEye1. The minor discrepancy between them can properly

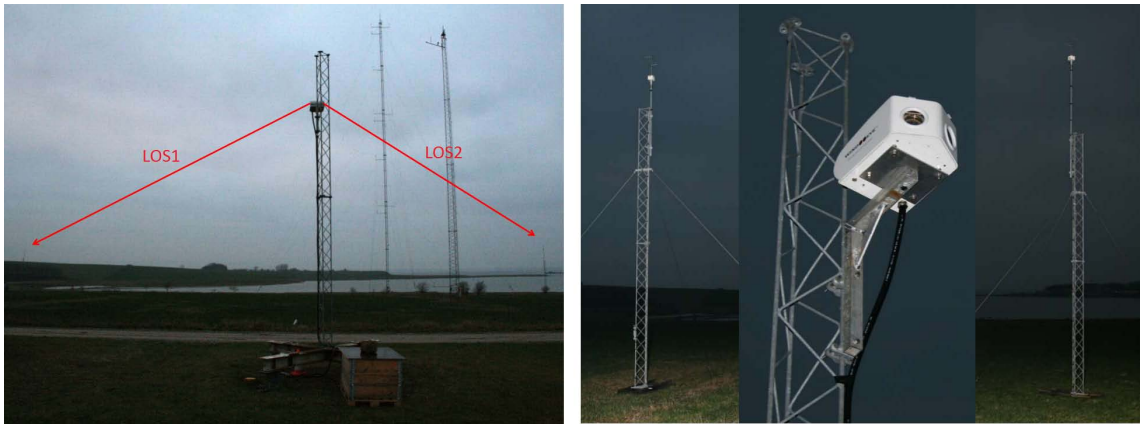

Figure 6.2: *Images of the experiment, where WindEye1 is compared with 2 sonic anemometers. The instruments are placed such that the sonic measurement volume is within 0.3 m of the lidar beam, and the distance between the sonic anemometers and lidar matches exactly to the respective weighting function peak position. Adapted from [67]*

be explained by the measurement volume difference between the two instruments. For the complete evaluation of WindEye1, see [68], but the overall conclusion is that Windeye1 measured the wind direction with a high accuracy compared to the sonic data throughout the whole campaign.

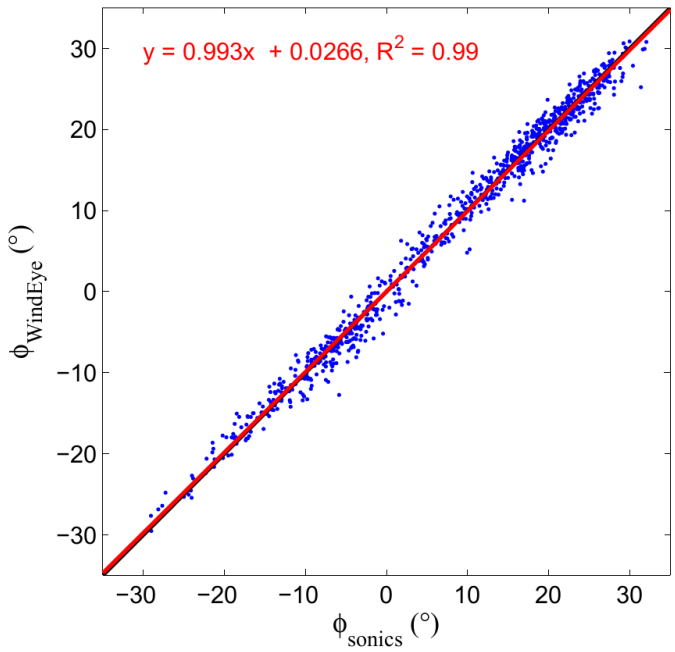

Figure 6.3: *The wind direction correlation between WindEye and the two sonic anemometers. Each data point represents a data block of 2 minutes wind data, and the data are selected from both the beginning and the end of the measurement period to ensure consistency. From [68]*

6.2 WindEye vs. Windscanner R2D1

In this section, a side-by-side wind speed measurement comparison between WindEye2 and another lidar system, Windscanner R2D1, is presented. Windscanner R2D1 is based on a modified CW ZephIR wind lidar produced by Natural Power U.K., which uses a fiber laser and a EDFA as the light source. The unit has the capability to control both the direction and the focus of the output beam [69], hence it can easily match the beam geometry of WindEye2. In this experiment, we are only interested in the average radial wind speed comparison between the two lidars. Thus, the switching and scanning features were disabled for WindEye2 and Windscanner R2D1, respectively, during the experiment. The main difference between the two systems is the laser linewidth due to the choice of different light sources. The laser linewidth of R2D1 should be 2-3 orders of magnitude narrower than the light source of WindEye2.

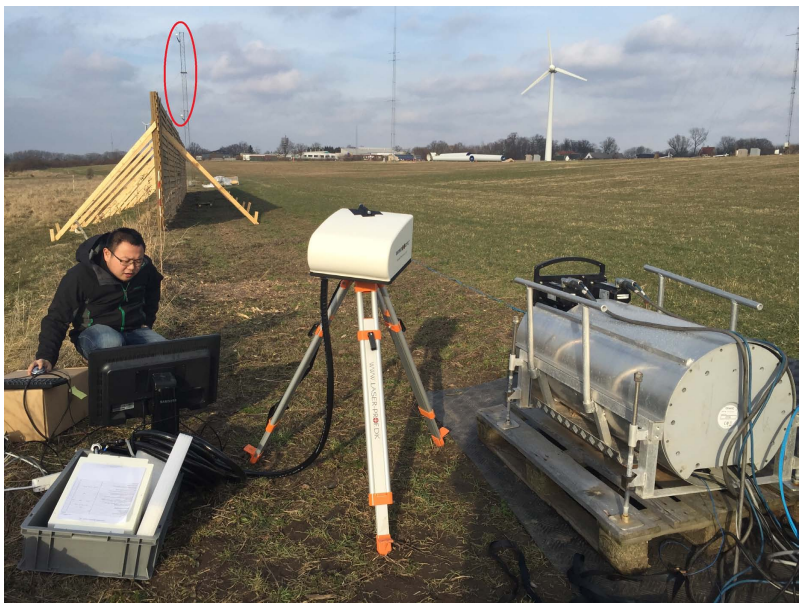

Figure 6.4: *An image of the experiment, where WindEye2 and Windscanner R2D1 was placed side-by-side to measure the same wind field. The red ring marks a met-mast, which had two 3D sonic anemometers installed. The met-mast was roughly 78 m ahead of the two lidars, and one of the sonic sensors was mounted at an altitude of 18 m above the ground.*

As shown in Fig. 6.4, the units were placed side-by-side at the measurement site of DTU Risoe. The focus of both systems were intended to be at 80 m. The exact weighting function was measured after the experiment using the same method as presented in Fig. 3.2. The output of WindEye2 was located using a IR-detection card at the ground level to determine the direction. The focus was then elevated such that the angle of elevation of the LOS was 12 degrees. R2D1 has a sophisticated targeting system, and was adjusted to match the LOS of the WindEye2. The actual

beam positions of the units were not confirmed by visually inspection, but they are expected to be at least be within a couple of meters of each other. The measurement positions were very close to a 3D sonic anemometer mounted on a met-mast. The sonic data can become useful, if the data was inconsistent between the two lidars. The sonic anemometer is roughly 78 m away, and placed 18 meters above the ground.

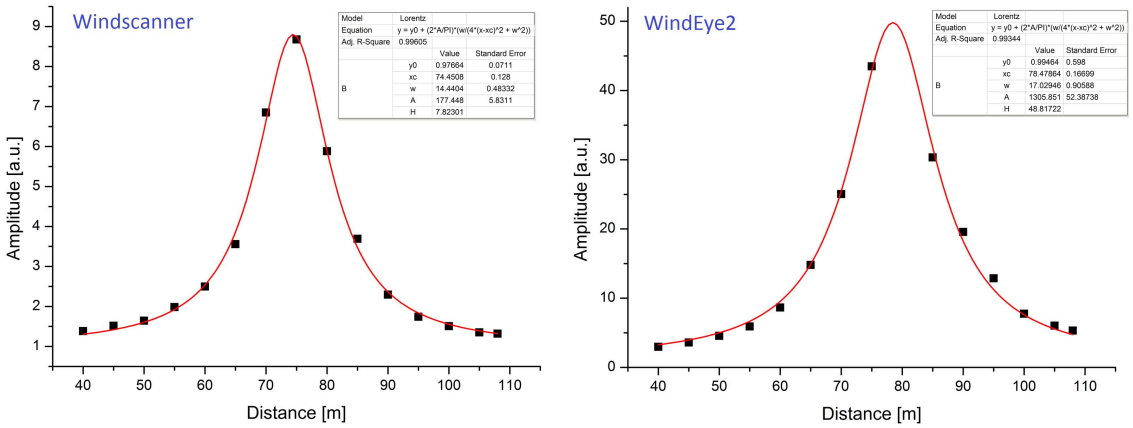

Figure 6.5: *The measured weighting function of both WindEye2 and Windscanner R2D1. The probe distance is 74.45 m and the probe length is 14.44 m for R2D1; while the probe distance is 78.47 m and the probe length is 17.03 m for WindEye2.*

The measured weighting function of both systems are shown in Fig. 6.5. The probe distance is 74.45 m and the probe length is 14.44 m for R2D1; while the probe distance is 78.47 m and the probe length is 17.03 m for Windeye2. Recalling Eq. (3.3), the probe length should (to the first order) scale with probe distance squared. Thus, if the probe distance of R2D1 had been 78.47 m, the probe length should be around 16.04 m. Based on this, we should expect the systems to behave quite similarly when measuring the average radial wind speed. Since the linewidth difference between the two light sources can only affect the spectral shape of the acquired wind spectra, but not the value of the average radial speed.

The experiment results are presented in Fig. 6.6. Since WindEye2 and R2D1 were not synchronised in time, the time delay between them was determined in the post-processing, and the presented data is the best-found match. In general, the wind data from the two lidars match quite well, and the 1 Hz wind data correlation between the system is $r^2 = 0.96$. However, WindEye2 is consistently measuring a higher wind speed than R2D1 over the whole measurement series, and the mean speed off-set is 0.2 m/s. This may be explained by the weighting function difference. The actually probe distance of the R2D1 was (unlike our expectation) 4 m shorter than WindEye2. Since both LOS had an angle of elevation of 12 degrees, the Windeye was measuring a slight higher (0.83 m) altitude than R2D1. We know that the wind speed increases with altitude, thus the wind speed off-set between the two lidars was likely caused by this. Unfortunately, the R2D1 was not available for us

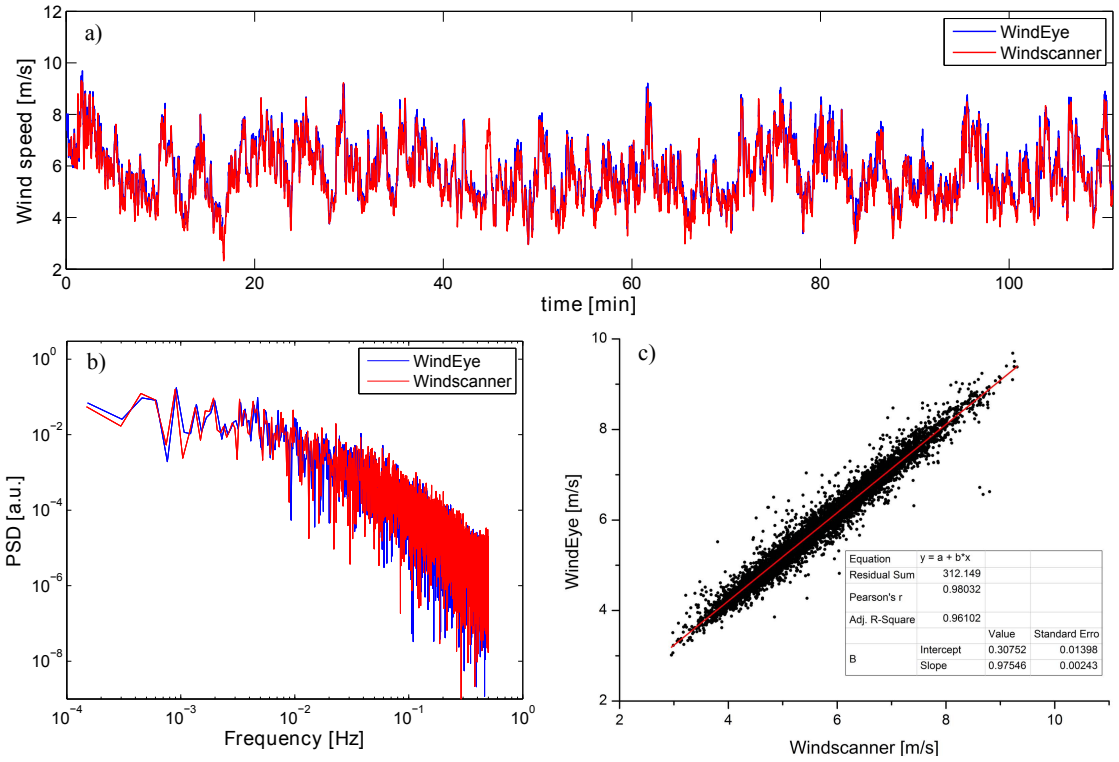

Figure 6.6: *The experiment result of the side-by-side comparison between WindEye2 and Windscanner R2D1. a) The wind data from WindEye2 and Windscanner R2D1 over 110 minuets. These are the mean radial wind speed at 1 Hz, a constant time delay was added to the Windscanner data, since the two lidars are not synchronised in time. b) PSD of 1 Hz wind data of both lidars shown in a). c) The wind speed correlation between WindEye2 and Windscanner R2D1, the r^2 value of the two system is 0.96 for 1 Hz wind data.*

after this experiment due to other measurement campaigns, so we could not redo the experiment to confirm our hypothesis.

We can conclude that, despite the huge linewidth difference, there is no notable performance difference between WindEye2 and R2D1 when measuring the average radial speed. Thus, for applications such as turbine yaw control, where the only required parameter is the average radial wind speed of minimum two LOS, there should be no fundamental hindrance for WindEye to perform as well as a fiber laser based lidar system.

6.3 SNR as Function of Focus Distance

As discussed in Chapter 3, the telescope design has little impact on the total signal power, P_s in a CW CDL system, but it does affect the SNR through the weighting function. To demonstrate this, we have devised a wind measurement experiment,

where the focus of the transceiver telescope is adjustable. This is achieved by mounting one of the telescope lenses on a piezoelectric translation stage. It allows us to adjust the probe range continuously from 10 m to 120 m. A measurement series was conducted where the focus was switched between 20 m and 60 m. Recalling Eq. (3.3), the probe length scales roughly with the focus squared, hence the probe length will be 9 times shorter for the 20 m focus than that for the 60 m focus.

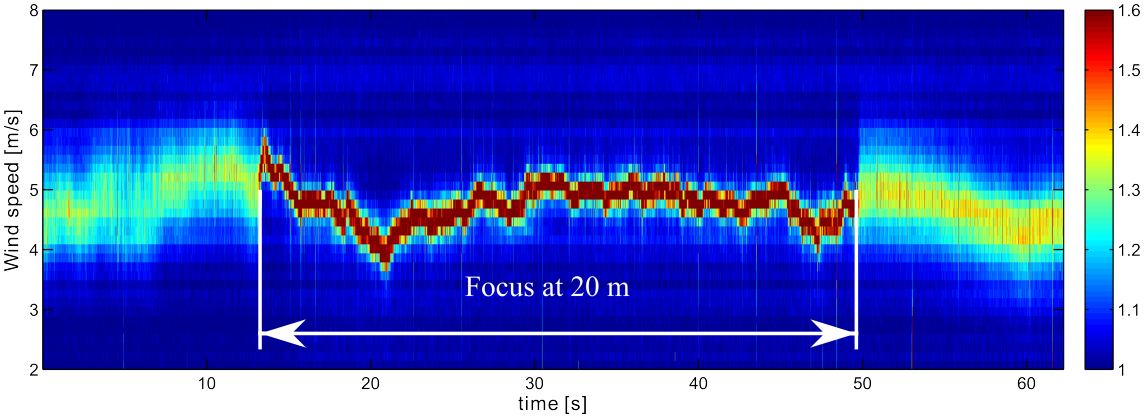

Figure 6.7: *50 Hz wind data, telescope focus was changed from 60 m to 20 m and back to 60 m again. The transition times are around 13 s and 50 s, respectively. The color intensity represents the Doppler signal strength.*

The measurement height is relatively close to the ground (~ 5 m) – the wind field contains relatively many speed components. It means, that a higher spatial resolution (shorter probe length) will give rise to a narrower signal bandwidth, see discussion in Section 3.2. The measured wind data is shown in Fig. 6.7, and the result is very consistent with our expectation. It is clear, that the wind data from 20 m focus (between 13 s and 50 s) has a much narrower signal bandwidth. Note, the signal bandwidth difference between the two measurement points, is a combination of the probe volume change and the distanced dependent linewidth (discussed in Chapter 4).

Figure 6.8 shows the lidar signal power as function of time, and the data contains a baseline of P_s and some outliers. There is a time variation of the P_s baseline, but it seems not to be related to the focus change; since no significant P_s baseline variation occurs at one of the focus transition point (50 s mark). This suggests, the mean signal power variation (baseline) is properly caused by the aerosol concentration variations in the measurement area. A single wind spectral from each cases are shown in Fig. 6.8. For these particular time frames (33.14 s and 53.82 s), the P_s is more or less constant, while the SNR_{peak} is clearly higher for the 20 m focus case, confirming our claim earlier in this section.

Another observation from Fig 6.8 is, that there are some outliers deviating from the mean P_s baseline. It is due to a phenomena called single particle event [70]. Basically, when the probe volume gets sufficiently small, the assumption of uniformly distributed backscatters of Eq (3.1) starts to break down. This can also be confirmed

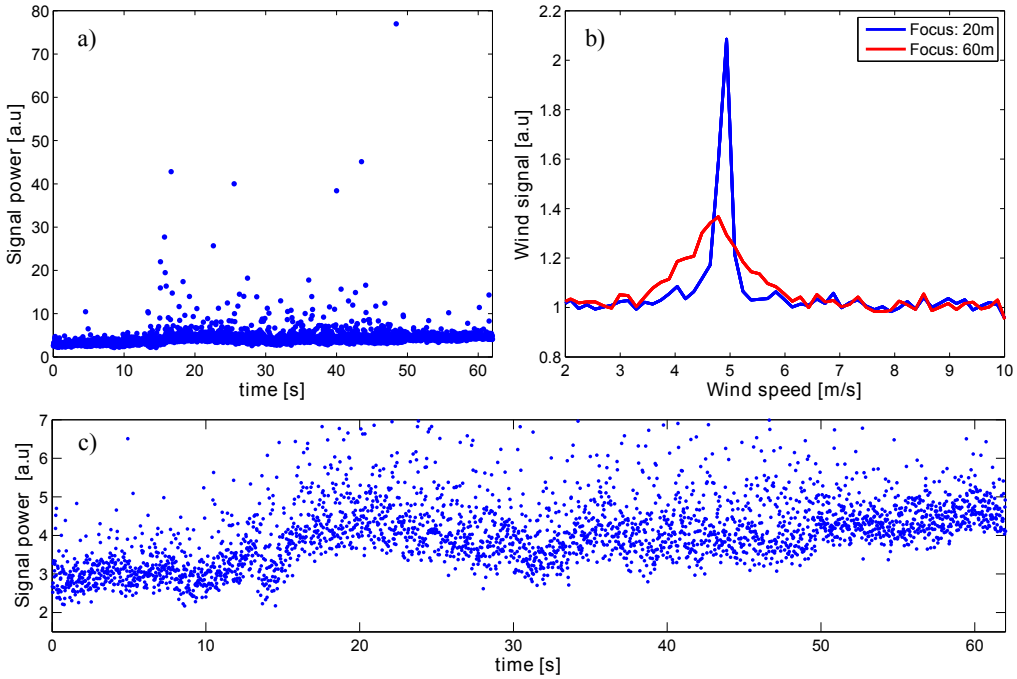

Figure 6.8: *a) The lidar signal power, P_s of the wind data presented Fig. 6.7. b) Two wind spectral samples samples of the data in Fig. 6.7. The blue curve is from the time frame 33.14 s, and the red curve is from the time frame 53.82 s. c) A zoom-in version of a).*

by the fact that the occurrence is much more frequent when the focus is 20 m (13 s to 50 s in the data series). The single particle event can be utilized to reduce the laser power requirement since the SNR is much larger during the event, but for our applications this effect is irrelevant, since a minimum probing range is required for turbine control.

6.4 Yaw Misalignment Correction Using WindEye

As it is today, Windar has many installations with the WindEye system around the globe. Observation from these installations indicates that yaw-misalignment is a common issue for commercial wind turbines, but the degree of the misalignment varies from turbine to turbine.[1] Figure 6.9 shows an example of yaw misalignment correction using WindEye3 on one of Windar's installations, where the yawing has been improved significantly using WindEye3. This demonstrates that turbine yaw error correction using our lidar design based on a semiconductor light source is possible.

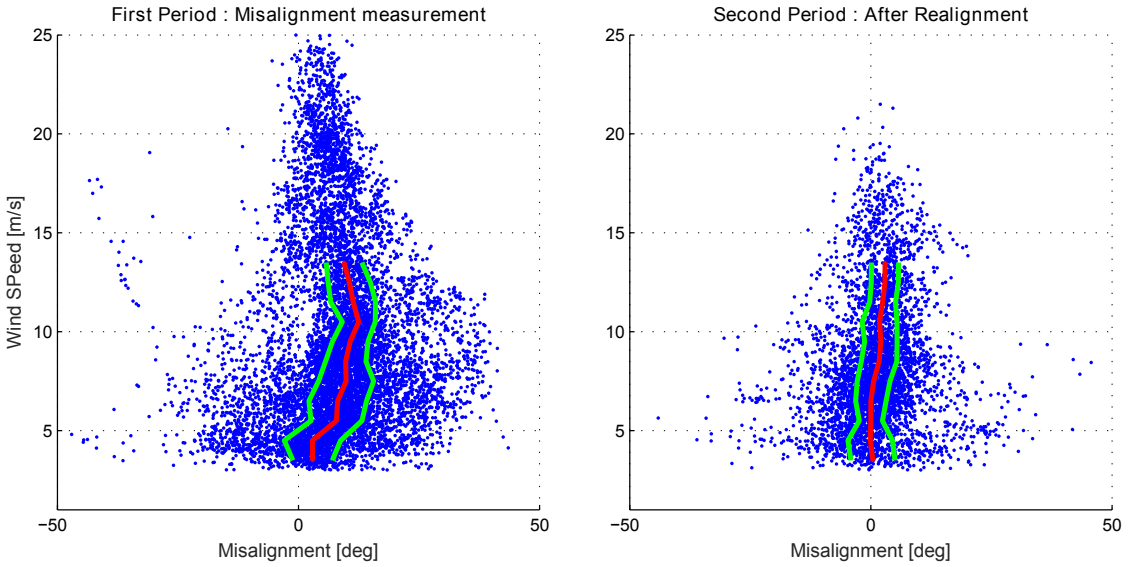

Figure 6.9: *The yaw misalignment before and after a realignment of the turbine using WindEye3. First period: wind data from 2014 October 23rd to 2015 February 18th; second period: 2015 March 12 to 2015 April 27. The mean misalignment was 8.09 degrees before the realignment, and the mean misalignment after is only 0.70 degrees. The data is from one of Windar's installations, it was processed by wind data analyst Antoine Larvol from Windar.*

[1] some samples of severely misaligned turbines can be found in [66].

7 Conclusion

In this work, different design possibilities to realize an industrial wind lidar were investigated. The instrument is intended for active yaw (or even pitch) control of individual wind turbines. The heart of the project was to utilize a semiconductor light source instead of fiber-laser-based light sources to bring down the cost. However, the scientific findings in this project are generic, and in most cases valid for any CW CDL design. The investigation was divided into different areas to, separately, address the key elements in the lidar design. A simple representation of the CW CDL SNR including the most relevant noise sources was formulated, and thorough investigations were conducted in the three following topics: The limitations of transceiver design, the lidar light source, and the beam steering mechanism. Finally, the commercialized wind lidar system for yaw control was evaluated in different field tests.

It was concluded that although the signal power is nearly independent of transceiver telescope design, it still has a great impact on the SNR through its influence on the weighting function in a CW CDL design; and it was proven both numerically and experimentally, that the beam truncation through the transceiver telescope has significant impact on the weighting function. This fact has often been ignored in the literature, and the conventional expression (3.6) for the weighting function has to be revised. It is also worth to note that the weighting function peaks slightly before the beam focus in a CW CDL system, and its location approaches the focus position for diffraction limited systems. Thus, it is recommendable to always characterize the weighting function of a CW CDL design.

The common specification of the laser linewidth as the HFHM of the self-heterodyne spectrum is proven to be misleading. In reality, the so-called laser linewidth depends on the delay length in the set-up due to the presence of $1/f$ flicker noise. Thus, the laser linewidth should always be specified with the self-heterodyne delay length, and it should be matched with the need of individual application to measure the relevant laser linewidth for the application. This reduces the conventional linewidth requirement of the lidar light source, since the probing distance of turbine control is around 100 m. It was also concluded, that since the Doppler spectrum of the wind field can easily span over a couple of MHz (due to the long probe length), the SNR will not benefit from laser linewidth that is much narrower. This relaxes the linewidth requirement of the lidar light source further. Combining this with successfully PIIN suppression through reducing the delay time

between the LO and possible stray light, semiconductor light sources will not suffer as much SNR penalty as initially expected from the larger linewidth.

Two different beam steering mechanism – one based on a LCR device and the other based on a MEMS-SM – was demonstrated. Both designs fulfil the beam steering requirements of turbine yaw control, but the MEMS-SM design is more desirable for pitch control where more than two LOS is required. Furthermore, the MEMS-SM also provides the possibility to reduce the eye safety requirements through active dithering of the beam focus.

During the project period, Windar has successfully commercialized an industrial lidar system for active yaw control of individual wind turbines, and many of the design choices were based on the research results presented here. Different field tests were conducted to evaluate this product. It was concluded that WindEye is able to measure the wind speed and direction with very high accuracy, when comparing it with sonic anemometers and a commercial fiber-laser based CW wind lidar. It was also shown (in Section 6.4) that yaw error correction using WindEye is really possible.

Ongoing Measurement Campaign

In this project, a CW CDL with 4 LOS was successfully demonstrated. A measurement campaign as a preliminary study of the active pitch control using this design was established at end of this project. The campaign is a collaboration between DTU Fotonik, DTU Wind Energy and Windar Photonics, where DTU Fotonik and Windar provide the wind lidar prototype based on the design discussed in Section 5.3, and DTU Wind Energy will handle the data evaluations. The lidar prototype is mounted on top of a Vestas V52 turbine (provided by DTU Wind Energy) and the campaign will last for at least several months. The experiment result will likely reveal some instrumentation challenges or further improvement requirements for the pitch control application.

Bibliography

[1] "Global wind energy council." `http://www.gwec.net/global-figures/wind-in-numbers/`.

[2] T. Knudsen, T. Bak, and M. Svenstrup, "Survey of wind farm control—power and fatigue optimization," *Wind Energy*, vol. 18, no. 8, pp. 1333–1351, 2015.

[3] T. F. Pedersen, N. Sørensen, L. Vita, and P. Enevoldsen, "Optimization of Wind Turbine Operation by Use of Spinner Anemometer," tech. rep., 2008.

[4] G. Biernson and R. Lucy, "a Coherent Laser Pulse-Doppler Radar," *Proc. IEEE*, vol. 51, no. 1, pp. 202–213, 1963.

[5] Y. Yeh and H. Z. Cummins, "LOCALIZED FLUID FLOW MEASUREMENTS WITH AN He[Single Bond]Ne LASER SPECTROMETER," *Appl. Phys. Lett.*, vol. 4, no. 10, p. 176, 1964.

[6] J. W. Foreman, E. W. George, and R. D. Lewis, "Measurement of Localized Flow Velocities in Gases With a Laser Doppler Flowmeter," *Appl. Phys. Lett.*, vol. 7, no. 4, p. 77, 1965.

[7] I. Goldstein and A. Chabot, "7B3 - Characteristics of a traveling-wave ruby single-mode laser as a laser radar transmitter," *Quantum Electron. IEEE J.*, vol. 2, no. 9, pp. 519–523, 1966.

[8] C. K. N. Patel, "Continuous-Wave Laser Action on Vibrational-Rotational Transistions of CO_2," *Phys. Rev.*, vol. 136, no. 5A, pp. A1187 – A1193, 1964.

[9] R. M. Huffaker, "Laser Doppler Detection Systems for Gas Velocity Measurement," *Appl. Opt.*, vol. 9, no. 5, pp. 1026–1039, 1970.

[10] T. J. Kane, W. J. Kozlovsky, R. L. Byer, and C. E. Byvik, "Coherent laser radar at 1.06 microm using Nd:YAG lasers.," *Opt. Lett.*, vol. 12, no. 4, pp. 239–41, 1987.

[11] P. J. Suni and S. W. Henderson, "1-mJ/pulse Tm:YAG laser pumped by a 3-W diode laser.," *Opt. Lett.*, vol. 16, no. 11, pp. 817–9, 1991.

[12] C. J. Karlsson, F. a. Olsson, D. Letalick, and M. Harris, "All-Fiber Multifunction Continuous-Wave Coherent Laser Radar at 1.55 num for Range, Speed, Vibration, and Wind Measurements.," *Appl. Opt.*, vol. 39, no. 21, pp. 3716–3726, 2000.

[13] J. P. Cariou, B. Augere, and M. Valla, "Laser source requirements for coherent lidars based on fiber technology," *Comptes Rendus Phys.*, vol. 7, no. 2, pp. 213–223, 2006.

[14] E. Branlard, A. T. Pedersen, J. Mann, N. Angelou, A. Fischer, T. Mikkelsen, M. Harris, C. Slinger, and B. F. Montes, "Retrieving wind statistics from average spectrum of continuous-wave lidar," *Atmos. Meas. Tech.*, vol. 6, no. 7, pp. 1673–1683, 2013.

[15] "Wind Lidar," in *Laser Remote Sens.* (T. Fujii and T. Fukuchi, eds.), pp. 469–722, CRC, 1 ed., 2005.

[16] J. Mann, A. Peña, F. Bingöl, R. Wagner, and M. S. Courtney, "Lidar Scanning of Momentum Flux in and above the Atmospheric Surface Layer," *J. Atmos. Ocean. Technol.*, vol. 27, no. 6, pp. 959–976, 2010.

[17] M. Harris, M. Hand, and A. D. Wright, "Lidar for turbine control," *NREL Tech. Rep.*, vol. NREL/TP-50, no. January, pp. TP–500–39154, 2006.

[18] R. S. Hansen and C. Pedersen, "All semiconductor laser Doppler anemometer at 1.55 μm," *Opt. Express*, vol. 16, no. 22, p. 18288, 2008.

[19] P. J. Rodrigo and C. Pedersen, "Field performance of an all-semiconductor laser coherent Doppler lidar," *Opt. Lett.*, vol. 37, no. 12, p. 2277, 2012.

[20] P. a. Fleming, a.K. Scholbrock, a. Jehu, S. Davoust, E. Osler, a.D. Wright, and a. Clifton, "Field-test results using a nacelle-mounted lidar for improving wind turbine power capture by reducing yaw misalignment," *J. Phys. Conf. Ser.*, vol. 524, p. 012002, 2014.

[21] S. Wan, L. Cheng, and X. Sheng, "Effects of Yaw Error on Wind Turbine Running Characteristics Based on the Equivalent Wind Speed Model," *Energies*, vol. 8, no. 7, pp. 6286–6301, 2015.

[22] J. F. Holmes and B. J. Rask, "Optimum optical local-oscillator power levels for coherent detection with photodiodes.," *Appl. Opt.*, vol. 34, no. 6, pp. 927–33, 1995.

[23] W. Sorin and D. Baney, "A simple intensity noise reduction technique for optical\nlow-coherence reflectometry," *IEEE Photonics Technol. Lett.*, vol. 4, no. 12, pp. 513–515, 1992.

[24] W. D. Sacher, E. J. Zhang, B. a. Kruger, and J. K. S. Poon, "High-speed laser modulation beyond the relaxation resonance frequency limit.," *Opt. Express*, vol. 18, no. 7, pp. 7047–7054, 2010.

[25] C. Spiegelberg, J. Geng, Y. Hu, Y. Kaneda, S. Jiang, and N. Peyghambarian, "Low-Noise Narrow-Linewidth Fiber Laser at 1550 nm (June 2003)," *J. Light. Technol.*, vol. 22, no. 1, pp. 57–62, 2004.

[26] S. Kameyama, T. Ando, K. Asaka, Y. Hirano, and S. Wadaka, "Compact all-fiber pulsed coherent Doppler lidar system for wind sensing," *Appl. Opt.*, vol. 46, no. 11, pp. 1953–1962, 2007.

[27] H. R. Carleton and W. T. Maloney, "A balanced optical heterodyne detector.," *Appl. Opt.*, vol. 7, no. 6, pp. 1241–3, 1968.

[28] P. Rodrigo and C. Pedersen, "Reduction of phase-induced intensity noise in a fiber-based coherent Doppler lidar using polarization control.," *Opt. Express*, vol. 18, no. 5, pp. 5320–7, 2010.

[29] C. M. Sonnenschein and F. a. Horrigan, "Signal-to-Noise Relationships for Coaxial Systems that Heterodyne Backscatter from the Atmosphere.," *Appl. Opt.*, vol. 10, no. 7, pp. 1600–4, 1971.

[30] V. Srivastava, J. Rothermel, a. D. Clarke, J. D. Spinhirne, R. T. Menzies, D. R. Cutten, M. a. Jarzembski, D. a. Bowdle, and E. W. McCaul, "Wavelength Dependence of Backscatter by use of Aerosol Microphysics and Lidar Data Sets: Application to 2.1- mum Wavelength for Space-Based and Airborne Lidars.," *Appl. Opt.*, vol. 40, no. 27, pp. 4759–69, 2001.

[31] J. Y. Wang, "Optimum truncation of a lidar transmitted beam.," *Appl. Opt.*, vol. 27, no. 21, pp. 4470–4, 1988.

[32] Q. F. C. of Inquiry, "UPWIND Final Report," 2011.

[33] J. Mann, J.-P. Cariou, M. S. Courtney, R. Parmentier, T. Mikkelsen, R. Wagner, P. Lindelöw, M. Sjöholm, and K. Enevoldsen, "Comparison of 3D turbulence measurements using three staring wind lidars and a sonic anemometer," *Meteorol. Zeitschrift*, vol. 18, no. 2, pp. 135–140, 2009.

[34] Y. Zhao, M. J. Post, and R. M. Hardesty, "Receiving efficiency of pulsed coherent lidars. 1: theory," *Appl. Opt.*, vol. 29, no. 28, pp. 4111–4119, 1990.

[35] R. G. Frehlich and M. J. Kavaya, "Coherent laser radar performance for general atmospheric refractive turbulence.," *Appl. Opt.*, vol. 30, no. 36, pp. 5325–52, 1991.

[36] B. J. Rye and R. G. Frehlich, "Optimal truncation and optical efficiency of an apertured coherent lidar focused on an incoherent backscatter target.," *Appl. Opt.*, vol. 31, no. 15, pp. 2891–9, 1992.

[37] B. J. Rye, "Primary aberration contribution to incoherent backscatter heterodyne lidar resturns," *Appl. Opt.*, vol. 21, no. 5, pp. 839–844, 1982.

[38] Radiant ZEMAX LLC, "ZEMAX ® Optical Design Program User's Manual," 2011.

[39] A. E. Siegman, "The Antenna Properties of Optical Heterodyne Receivers," *Appl. Opt.*, vol. 5, no. 10, p. 1588, 1966.

[40] T. Okoshi, K. Kikuchi, and a. Nakayama, "Novel method for high resolution measurement of laser output spectrum," *Electron. Lett.*, vol. 16, no. 16, p. 630, 1980.

[41] J. Barnes and D. Allan, "A statistical model of flicker noise," *Proc. IEEE*, vol. 54, no. 2, pp. 176–178, 1966.

[42] L. Cutler and C. Searle, "Some aspects of the theory and measurement of frequency fluctuations in frequency standards," *Proc. IEEE*, vol. 54, no. 2, pp. 136–154, 1966.

[43] Q. Hu, P. J. Rodrigo, and C. Pedersen, "Effects of 1/f frequency noise in self-heterodyne linewidth measurement system with various delay lengths," in *Conf. Lasers Electro-Optics Eur. (CLEO Eur.*, p. CH_P_34, 2015.

[44] L. B. Mercer, "1/F Frequency Noise Effects on Self-Heterodyne Linewidth Measurements," *J. Light. Technol.*, vol. 9, no. 4, pp. 485–493, 1991.

[45] Q. Hu, P. J. Rodrigo, and C. Pedersen, "Remote wind sensing with a CW diode laser lidar beyond the coherence regime," *Opt. Lett.*, vol. 39, no. 16, pp. 4875–4878, 2014.

[46] E. Bossanyi, B. Savini1, M. Iribas, M. Hau, B. Fischer, D. Schlipf, T. van Engelen, M. Rossetti, and C. E. Carcangiu, "Advanced controller research for multi-MW wind turbines in the UPWIND project," *Wind Energy*, vol. 15, no. 1, pp. 119–145, 2012.

[47] K. Petermann, "External optical feedback phenomena in semiconductor lasers," *IEEE J. Sel. Top. Quantum Electron.*, vol. 1, pp. 480–489, jun 1995.

[48] A. Champagne, J. Camel, R. Maciejko, K. Kasunic, D. Adams, and B. Tromborg, "Linewidth broadening in a distributed feedback laser integrated with a semiconductor optical amplifier," *IEEE J. Quantum Electron.*, vol. 38, pp. 1493–1502, nov 2002.

[49] M. Harris, G. N. Pearson, J. M. Vaughan, D. Letalick, and C. Karlsson, "The role of laser coherence length in continuous-wave coherent laser radar," *J. Mod. Opt.*, vol. 45, no. 8, pp. 1567–1581, 1998.

[50] P. J. Rodrigo and C. Pedersen, "Comparative study of the performance of semiconductor laser based coherent Doppler lidars," in *Proc. SPIE 8241, High-Power Diode Laser Technol. Appl. X* (M. S. Zediker, ed.), vol. 8241, pp. 824112–824112–7, feb 2012.

[51] Q. Hu, P. J. Rodrigo, and T. F. Q. Iversen, "Investigation of spherical aberration effects on coherent lidar performance," *Opt. Express*, vol. 21, no. 22, pp. 25670–25676, 2013.

[52] B. E. A. Saleh and M. C. Teich, *Fundamentals of Photonics*. Wiley, 2007.

[53] M. Sjöholm, T. Mikkelsen, J. Mann, K. Enevoldsen, and M. Courtney, "Time series analysis of continuous-wave coherent Doppler Lidar wind measurements," *IOP Conf. Ser. Earth Environ. Sci.*, vol. 1, p. 012051, 2008.

[54] D. Schlipf, D. J. Schlipf, and M. Kühn, "Nonlinear model predictive control of wind turbines using LIDAR," *Wind Energy*, vol. 16, no. 7, pp. 1107–1129, 2013.

[55] D. Schlipf, P. Fleming, F. Haizmann, A. Scholbrock, M. Hofsäß, A. Wright, and P. W. Cheng, "Field Testing of Feedforward Collective Pitch Control on the CART2 Using a Nacelle-Based Lidar Scanner," *J. Phys. Conf. Ser.*, vol. 555, p. 012090, 2014.

[56] T. Mikkelsen, J. Mann, M. Courtney, and M. Sjöholm, "Windscanner: 3-D wind and turbulence measurements from three steerable doppler lidars," *IOP Conf. Ser. Earth Environ. Sci.*, vol. 1, p. 012018, 2008.

[57] International Electrotechnical Commission (IEC), "IEC 61400-1 Wind turbine generator systems - Part 1: Design requirements," vol. 2005, pp. 1–92, 2005.

[58] A. Sathe and J. Mann, "A review of turbulence measurements using ground-based wind lidars," *Atmos. Meas. Tech.*, vol. 6, no. 11, pp. 3147–3167, 2013.

[59] P. J. Rodrigo, T. F. Q. Iversen, Q. Hu, and C. Pedersen, "Diode laser lidar wind velocity sensor using a liquid-crystal retarder for non-mechanical beam-steering.," *Opt. Express*, vol. 22, no. 22, pp. 26674–9, 2014.

[60] Q. Hu, C. Pedersen, and P. J. Rodrigo, "Eye-safe diode laser Doppler lidar with a MEMS beam-scanner," *Opt. Express*, vol. 24, no. 3, p. 1934, 2016.

[61] K. A. Kragh, M. H. Hansen, and T. Mikkelsen, "Precision and shortcomings of yaw error estimation using spinner-based light detection and ranging," *Wind Energy*, vol. 16, no. 3, pp. 353–366, 2013.

[62] T. Mikkelsen, N. Angelou, K. Hansen, M. Sjöholm, M. Harris, C. Slinger, P. Hadley, R. Scullion, G. Ellis, and G. Vives, "A spinner-integrated wind lidar for enhanced wind turbine control," *Wind Energy*, vol. 16, no. 4, pp. 625–643, 2013.

[63] S. T. S. Holmström, U. Baran, and H. Urey, "MEMS laser scanners: A review," *J. Microelectromechanical Syst.*, vol. 23, no. 2, pp. 259–275, 2014.

[64] L. Mol, L. a. Rocha, E. Cretu, and R. F. Wolffenbuttel, "Fast step-response settling of micro electrostatic actuators operated at low air pressure using input shaping," *J. Micromechanics Microengineering*, vol. 19, no. 7, p. 074020, 2009.

[65] M. Harris, S. M. Stone, and A. Lewin, "Lidar Mean Power Reduction." U.S. Patent 20110149363, 2011.

[66] "Imagine being able to predict the wind, WindEYE™." `http://www.windarphotonics.com/f/f1/wp_profile_single_screen.pdf`.

[67] M. Sjöholm, E. Dellwik, Q. Hu, J. Mann, C. Pedersen, and P. J. Rodrigo, "FIELD TEST OF AN ALL-SEMICONDUCTOR LASER-BASED COHERENT CONTINUOUS-WAVE DOPPLER LIDAR FOR WIND ENERGY APPLICATIONS," in *17th Int. Symp. Adv. Boundary-Layer Remote Sens.*, 2014.

[68] E. Dellwik, M. Sjöholm, and J. Mann, *An evaluation of the WindEye wind lidar DTU Vindenergi E Rapport 2015*. DTU Wind Energy, 2015.

[69] T. Mikkelsen, "WindScanner. eu - a new Remote Sensing Research Infrastructure for On- and Offshore Wind Energy," 2013.

[70] M. Harris, G. N. Pearson, K. D. Ridley, C. J. Karlsson, F. A. Olsson, and D. Letalick, "Single-Particle Laser Doppler Anemometry at 1.55 μm," *Appl. Opt.*, vol. 40, no. 6, pp. 969–73, 2001.

A List of Abbreviations

AOM	Acousto-Optic Modulator
BPLO	Back Propagated Local Oscillator
CDL	Coherent Doppler Lidar
CNR	Carrier to Noise Ratio
CW	Continuous Wave
DFB-FL	Distributed Feedback Fiber Laser
EDFA	Erbium-Doped Fiber Amplifier
FFT	Fast Fourier Transform
FPGA	Field-Programmable Gate Array
FWHM	Full Width Half Maximum
HWHM	Half Width Half Maximum
LCR	Liquid-Crystal Retarder
LO	Local Oscillator
LOS	Line Of Sight
MEMS-SM	Micro-Electro-Mechanical-System Scanning Mirror
MOPA-SL	Master-Oscillator Power-Amplifier Semiconductor Laser
OPD	Optical Path Difference
PIIN	Phase Induced Intensity Noise
PSD	Power Spectral Density
RF	Radio Frequency

RIN	Relative Intensity Noise
SA	Spherical Aberration
SNR	Signal to Noise Ratio

B WindEye Description

WINDAR PHOTONICS

www.windarphotonics.com

With our wind sensor you can!

- **Yaw optimization: 1-4% AEP increase**
- **Load reduction: 10-14%**
- **High ROI**
- **CIL - Control Integrated LiDAR**

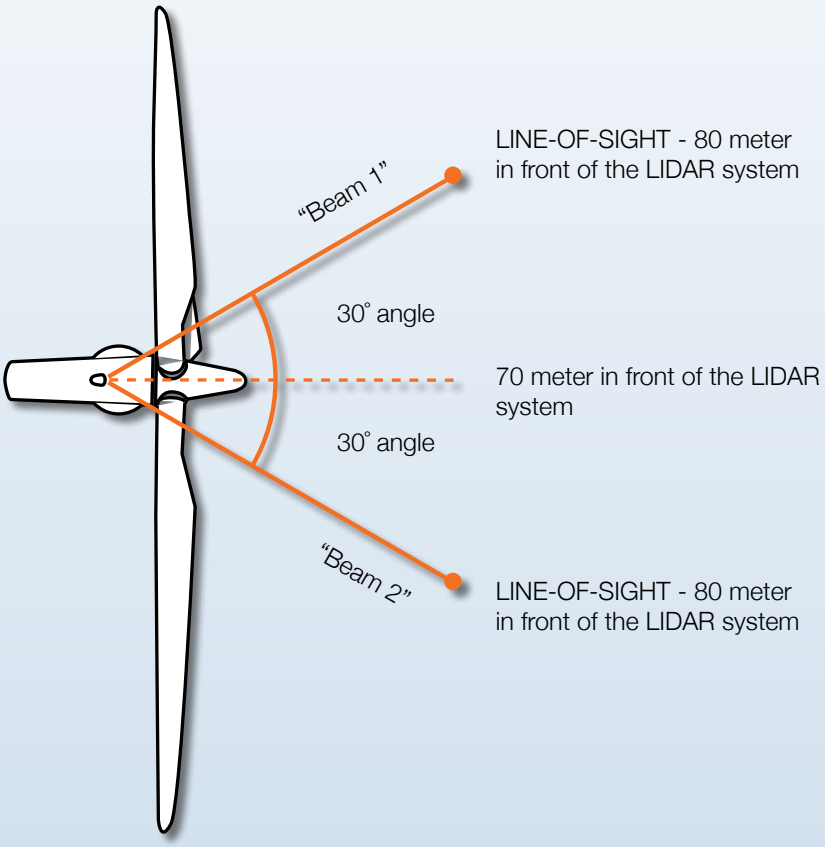

Data every second

The LIDAR wind sensor emits two laser beams horizontally in a radius of 60 degrees. The exact speed is measured in the laser beam line of sight, and by means of that measurement accurate software algorithms calculate the oncoming wind speed and direction relative to the turbine direction every second.

From the top of the nacelle, the precise wind direction and wind speed are measured 80 metres out in front of the blades.

Researchers in the wind industry envision tomorrow's wind turbines as "smart machines", capable of maximizing power production and minimizing dynamic load according to changes in the oncoming wind. This requires that each turbine is equipped with an instrument that can obtain accurate and timely knowledge of the wind inflow. Wind LIDARs, which use laser beams to remotely probe the flow of aerosols, are the right sensor for this task.

In the wind energy sector, laser-based wind sensors have become the add-on to conventional anemometry instruments.

The successful introduction of wind LIDARs can be attributed to their ability to accurately measure wind speed and direction remotely.

Predicting the wind
The wind speed and wind direction are measured accurately from the top of the turbine, while the wind is still far away from the blades.
With these data the turbine is able to adapt to the oncoming wind in advance, which results in increased power production and a decrease in wear-and-tear on the wind turbine.

Gain more power
You can expect a 1% to 4% increase in power and at least 10-14 % less stress on the vital components of the wind turbine. Depending on the price of power, your investment in the wind sensor could pay for itself within 12 to 36 months. In subsequent years, you can reap the economic benefits of the additional power production, decreased wear-and-tear and fewer stoppage days.

Benefits to you from the wind sensor
Our LIDAR wind sensor is an add-on to existing wind sensors and provides the basis for:

- Reduced yaw misalignment
- Optimized pitch system
- Reduced loads
- Precise wind data in front of the turbine
- Increased lifetime, decreased downtime

We are the result of a bright idea

Windar Photonics A/S is a young, forward-looking spin-off company from the Risø DTU research environment. In 2005, a research scientist had a bright idea about using LIDAR for wind sensing.

Wind sensors in a new light

A wind sensor that pays its way
Our wind sensor measures the wind using laser light. The principle known as LIDAR was invented back in the 1970s. But we have fine-tuned the technology and replaced expensive light sources with a much more affordable laser. We have filed a patent for the use of LIDAR. The result is a wind sensor unlike any other, which is well worth putting on all wind turbines.

What is LIDAR?

How light can measure the wind
LIDAR stands for “Light Detection And Ranging”. The light emitted by the wind sensor is reflected by small particles in the air: pollen, dust and water droplets. By measuring how these wind-borne particles move, we are able to calculate how the wind is moving. That, in simple terms, is the principle behind LIDAR wind sensing.

Purely optical, nothing mechanical

Inside the compact design there are no mechanical parts to wear out or break down. It is controlled entirely by electrical signals and can withstand extreme conditions at the top of a wind turbine. This means a minimum of maintenance. Our wind sensor is designed to operate maintenance-free for 24 months, and thus follows the servicing cycle of the wind turbine.

Features:

- No mechanical moving parts
- Very limited maintenance required
- Easy handling and installation
- Light and compact system
- Durable design

The WindEYE™ shows good correlation
The wind speed and wind direction measurements from the WindEYE™ correlates well with measurements performed with met. masts equipped with calibrated sonic sensors.

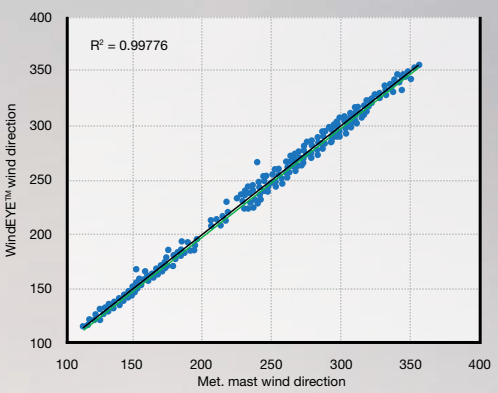

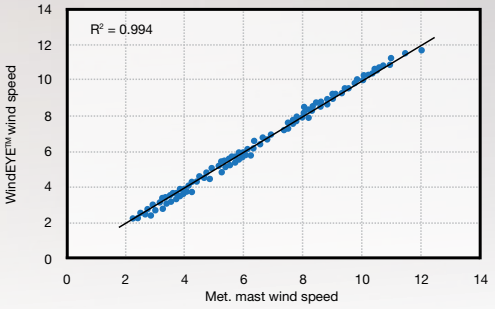

You harvest the wind better from the top

WindEYE™ is both a compact and a light-weight system (24 kilograms), that is also very durable.

WindEYE™ is designed to endure the harsh environment of today's wind turbines. Our well-proven and well-tested product enables you to use it in even the toughest environments. Furthermore, the system is designed and tested in order to withstand lightning in the lightning zone 0B.

We have designed the system with a lifetime of 20 years and a minimum of maintenance requirements. We aim to provide a relatively uncomplicated plug-and-play solution that is easy to install, use, and maintain, which will ultimately help you increase the energy output of wind turbines.

Functional specifications	
Laser source	CW – Continuos Wave laser
Operating Wavelength	1550nm (Eye safety class 1)
Wind speed range	2m/s to 30m/s (wind aligned)
Wind speed accuracy	0.2m/s (Lidar beam line-of-sight)
Wind direction range	-30° < ϕ< +30°
Wind direction accuracy	1°
Sensing range, Z0	80 m (line-of-sight), 70 m (horizontally for = 30°)
Probe length	10 m
Data Output Rate	1 Hz
Operating temperature	-40°C to +55°C
Storage temperature	-50°C to +70°C
Interfaces	RS485, Ethernet and USB
Power supply	24VDC, 20A (110VAC/230VAC as an option)
Optical head (mm)	443 x 250 x 190 (L x W x H)
Control unit (mm)	430 x 250 x 120 (L x W x H)
Optical head weight	15 kg incl. cable
Control unit weight	9 kg
Cable length	10 m
IP class	IP66 (optical head), IP30 (control unit)
Storage	60GB (12 months)
Data output (each second)	Line-of-sight wind speed (cm/s) Relative wind direction (1/100 degree) Wind speed (cm/s)

ROI - it's all about Asset Management

Electricity tariffs are constantly under pressure, and that challenges existing wind turbines to be as optimized and able to produce as much energy as possible. We at Windar Photonics understand this situation, and our aim is to take part in this efficiency increase, and to provide a solution that enables existing wind turbines to produce even more energy. A ROI, Return of Investment, between 1-4 years is a profitable investment that should appeal to any WPO and/or owner. Once you go above 4-4.5 years ROI you have to further consider other benefits from the LIDAR system such as load and maintenance reduction.

Cost efficient LIDAR system

	750kW	1,0MW	1,5MW	2,0MW	3,0MW	3,6MW	5,0MW	6,0MW
1,5%	11,4 YEARS	8,5 YEARS	5,7 YEARS	4,3 YEARS	2,8 YEARS	2,4 YEARS	1,7 YEARS	1,4 YEARS
2,0%	8,5 YEARS	6,4 YEARS	4,3 YEARS	3,2 YEARS	2,1 YEARS	1,8 YEARS	1,3 YEARS	1,1 YEARS
3,0%	5,7 YEARS	4,3 YEARS	2,8 YEARS	2,1 YEARS	1,4 YEARS	1,2 YEARS	0,9 YEARS	0,7 YEARS
4,0%	4,3 YEARS	3,2 YEARS	2,1 YEARS	1,6 YEARS	1,1 YEARS	0,9 YEARS	0,6 YEARS	0,5 YEARS

We help you optimize the energy output of your wind turbine.

Example of energy increase:

The following example uses data collected from a 3,6mw turbine during a two months measurement period, where wind data from SCADA was compared to the measurements from the WindEYE™

Measurement showed a mean misalignment of 6 degrees and an absolute mean yaw misalignment of 9,8 degrees without the yaw algorithm and 4,7 degrees with the yaw algorithm.

During the two months period the energy increase was a total of 35MWh, if the WindEye™ data was used instead of the SCADA data, which equals an energy gain of 2,38%.

The calculated return of investment for the above mentioned project was 1,5 years.

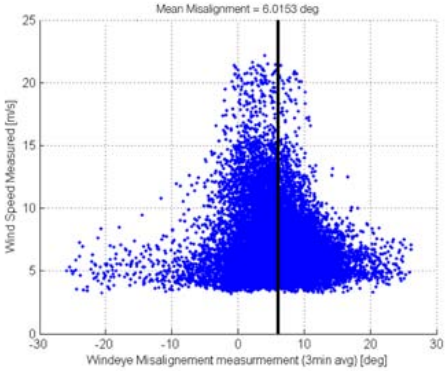

	Energy [MWh]
Energy produced using Scada data	1468.8
Energy produced if perfectly aligned	1520.5
Energy produced using yaw algorithm	1502.5
Energy gain using using yaw algorithm	35.0
Percentage og Energy gain if using Lidar instead of Scada	2.38 %
Maximum percentage og Energy gain if perfectly aligned	3.52 %

Absolute mean yaw misalignment	Value [deg]
Without yaw algorithm	9.8
With yaw algorithm	4.7

WindSwitch for Control Integrated LiDAR

A central feature of the WindEYE™ LiDAR system is its ability to integrate with the Wind Turbine controller without jeopardizing the safety chain, which we have dubbed CIL or Control Integrated LiDAR.

Most importantly, the integration with the controller allows the WindEYE™ system to dynamically measure and correct yaw-misalignment.

The WindSwitch combines the signals from the original wind-sensors in one switchbox, converts the signal from the WindEYE™ LiDAR to the protocol of the original wind-sensor signals, and gives the WindEYE™ signal into the WTG-controller, as long as the WindEYE™ signal is available.

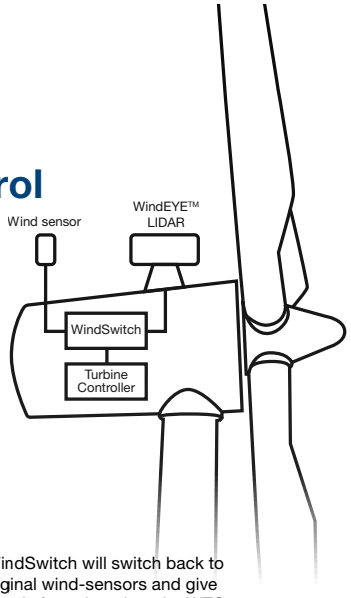

The WindSwitch will switch back to the original wind-sensors and give the signals from them into the WTG-controller in case the signal from the WindEYE™ LiDAR is no longer available due to climatic or technical reasons.

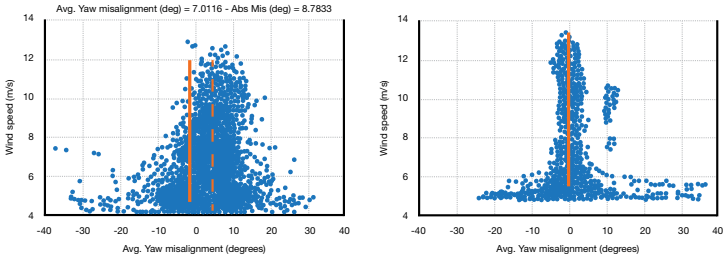

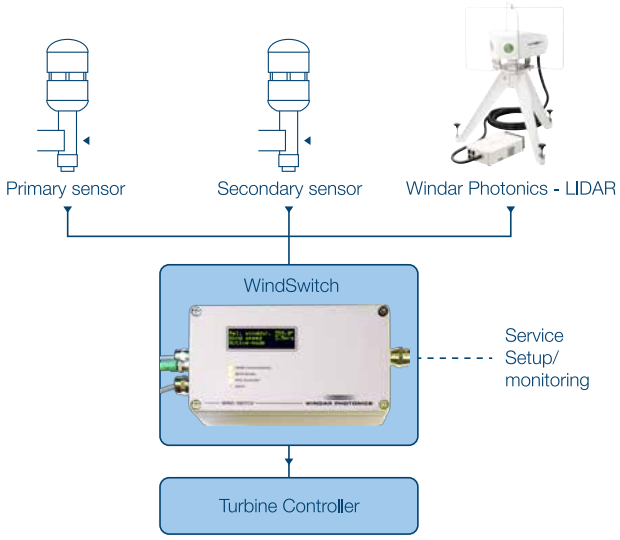

Protocol

Protocol list from RS485		
Protocol	**Specification**	**Unit**
Timestamp		YYYY/MM/DD HH:MM:SS
Vlos1	Measured Wind speed along beam 1	Cm/s
Vlos2	Measured Wind speed along beam 2	Cm/s
U	Calculated Lateral Wind speed	Cm/s
W	Calculated Axial Wind speed	Cm/s
V	Calculated Incoming Wind speed	Cm/s
Phi (Φ)	Calculated Misalignment angle	°x100
Status	1 second measurement Status	0/1 - Bad/Good

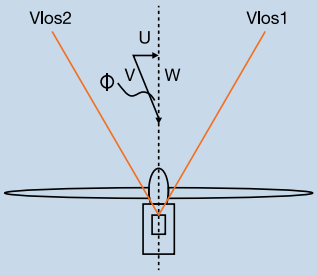

Optional:

Power Supply

Our WindEYE™ system can optionally be supplied with a 110VAC/230VAC power supply.

3G wireless internet for data extraction

Our WindEYE™ system can optionally be equipped with a 3G-module that makes it possible to access and extract the data stored in the WindEYE™ system remotely using an ordinary internet connection. The module is designed for durability, like the rest of the WindEYE™ system, to withstand the harsh conditions atop the wind turbine.

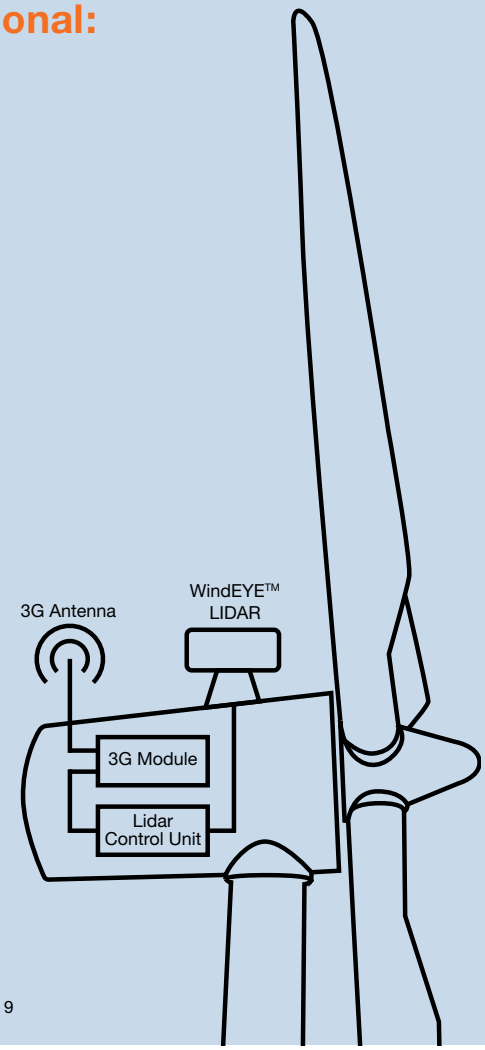

References

We have installations in different countries around the world and in different environments and on different wind turbine models. Due to our universal system it can be used on any wind turbine around the globe.

VESTAS 2 MW

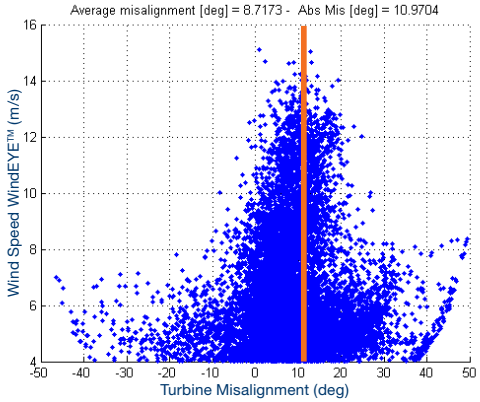

VESTAS 2 MW

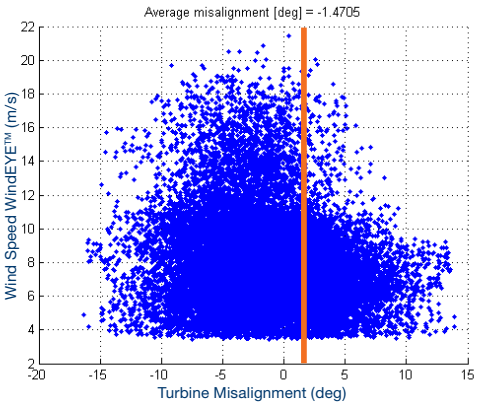

VESTAS 2 MW

SIEMENS 3,6 MW

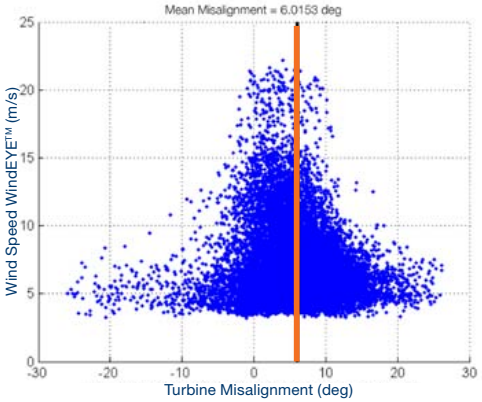

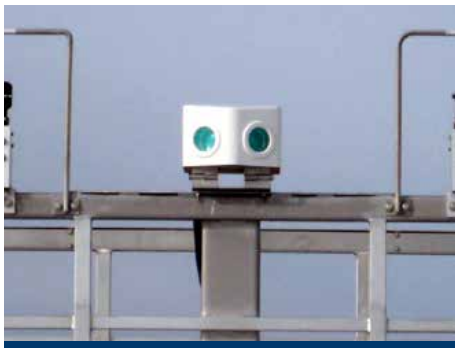

SIEMENS 3,6 MW

SIEMENS 3,6 MW

SIEMENS 2,3 MW

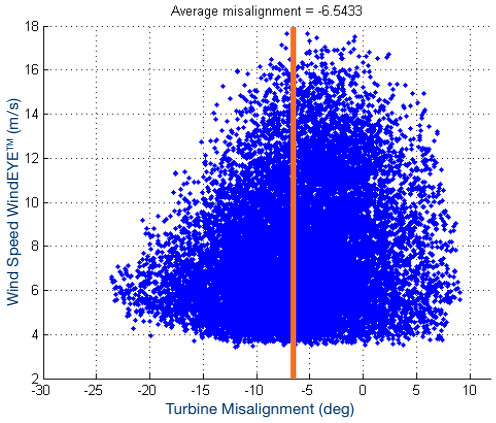

SINOVEL 1,5 MW

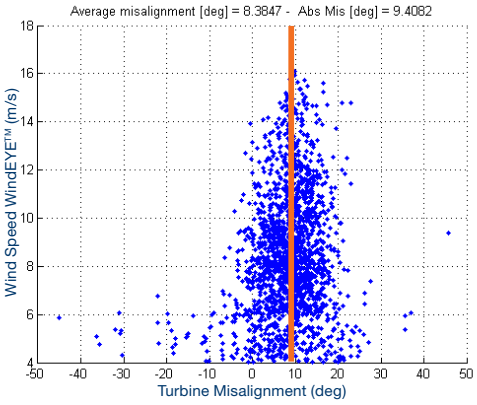

General references < 1 MW

MICON 600 kW

VESTAS 660 kW

WINDEY 750 kW

EWT 900 kW

General references 1-6 MW

DONGQI 1,5 MW

GAMESA 2 MW

ENVISION 3,6 MW

SIEMENS 6,0 MW

Cost efficient LIDAR solution:

- Yaw optimization: 1-4% AEP increase
- Load reduction: 10-14%
- High ROI
- CIL - Control Integrated LiDAR

Features:

- No mechanical moving parts
- Very limited maintenance required
- Easy handling and installation
- Light and compact system
- Durable design

WINDEYE™

Cost efficient LIDAR system

WINDAR PHOTONICS

www.windarphotonics.com

C Conference Slides from ISARS 2014

FIELD TEST OF AN ALL-SEMICONDUCTOR LASER-BASED COHERENT CONTINUOUS-WAVE DOPPLER LIDAR FOR WIND ENERGY APPLICATIONS

M. Sjöholm[1], E. Dellwik[1], Q. Hu[2], J. Mann[1], C. Pedersen[2], and P. J. Rodrigo[2]

[1]Department of Wind Energy
and
[2]Department of Photonics Engineering
at
Technical University of Denmark, Roskilde, Denmark

In collaboration with
the Danish company Windar Photonics A/S

Turbine Industry - Challenges

- Today, Capital is restricted and there is increasing requirement for Wind Turbines to be more cost efficient relative to alternative energy sources.
- Therefore the industry has high focus on optimizing the performance of the Turbines through:
  - Increase the efficiency of extracting energy from the wind
  - Increase the life time of the Turbines through load reductions
  - Reduce maintenance costs also through load reductions

The key to optimization
is
better wind intelligence
and
forward looking wind measurement equipment

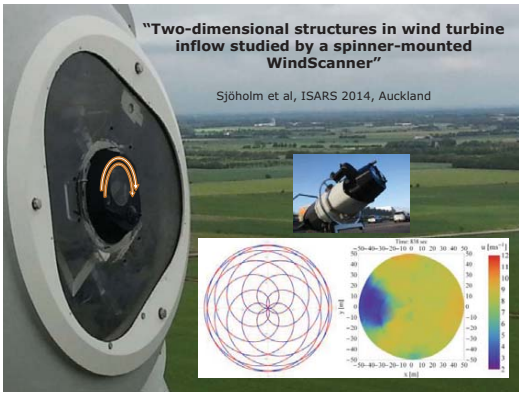

The low-cost alternative

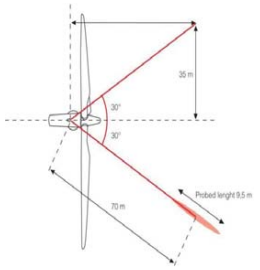

Courtesy Jørgen Korsgaard Jensen, Windar Photonics

Historical Development

2005 2006 2008 2010 2011 2012

Danish Technical University developed a CO_2 laser based Lidar system.

OPDI Technologies started development of a semiconductor based Lidar system

First Lidar using semiconductor laser developed.
1. Patent was filed.
Windar Photonics was established

Proof-of-concept

Polarisation system was introduced
2. Patent was filed

First installation on wind turbine – Vestas V47

Semiconductor Laser (SL)

Master Oscillator Power Amplifier (MOPA-SL)

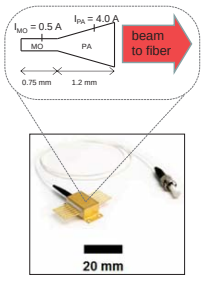

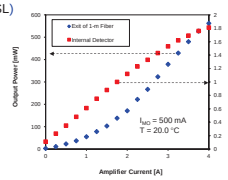

Optical Properties:

- λ = 1550 nm
- Gaussian beam out of fiber
- Output power > 500 mW
- Linewidth ~ 200 kHz
- Low relative intensity noise (RIN)
- Linear polarized beam

Line-of-sight comparison with sonic

Line-of-sight comparison with sonic

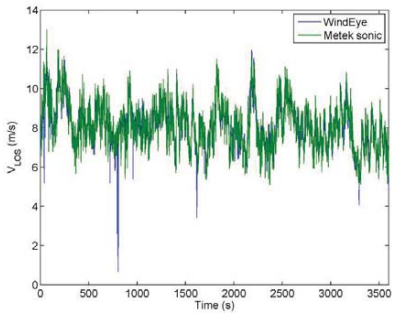

Switching between two beams

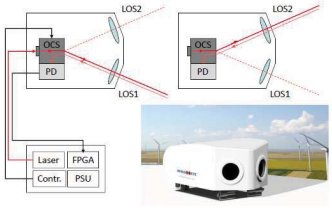

OCS = Optical Circulator/Switch
PD = Photo-detector
Contr. = Controller of OCS liquid crystal switch
FPGA = Field-Programmable Gate Array
PSU = Power Supply Unit

Optical Switch Principle

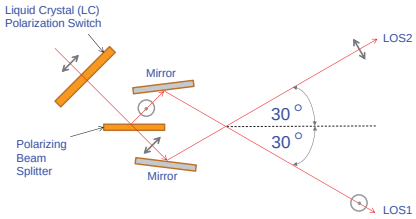

LC Voltage	LC Output Polarization	Active Beam
1.5 V (rms)	⊙	LOS1
25 V (rms)	↕	LOS2

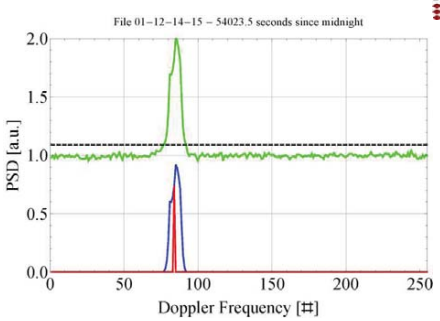

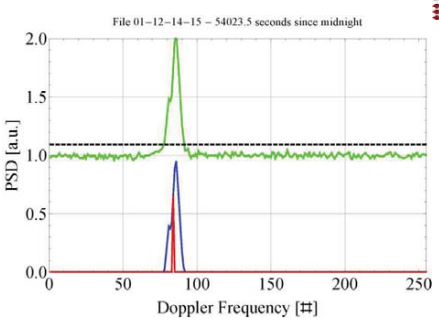

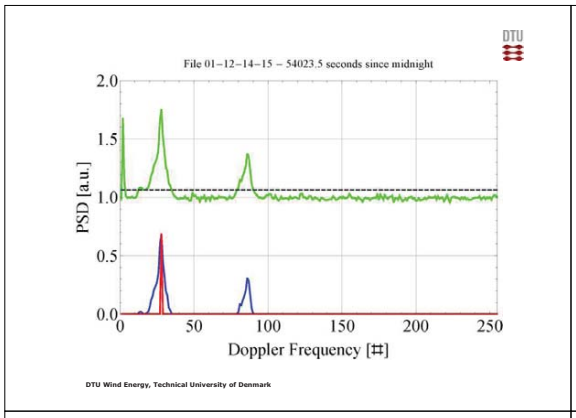
DTU
File 01–12–14–15 – 54023.5 seconds since midnight
PSD [a.u.]
Doppler Frequency [⌗]
DTU Wind Energy, Technical University of Denmark

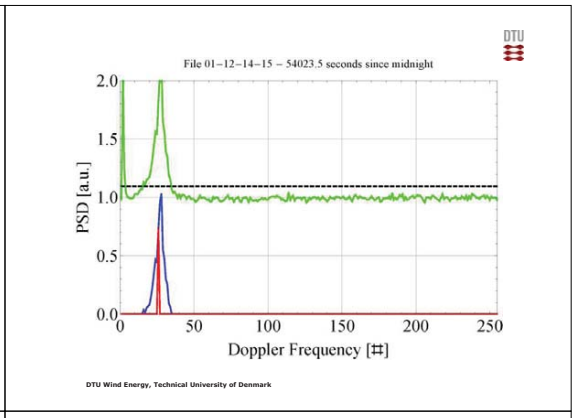
DTU
File 01–12–14–15 – 54023.5 seconds since midnight
PSD [a.u.]
Doppler Frequency [⌗]
DTU Wind Energy, Technical University of Denmark

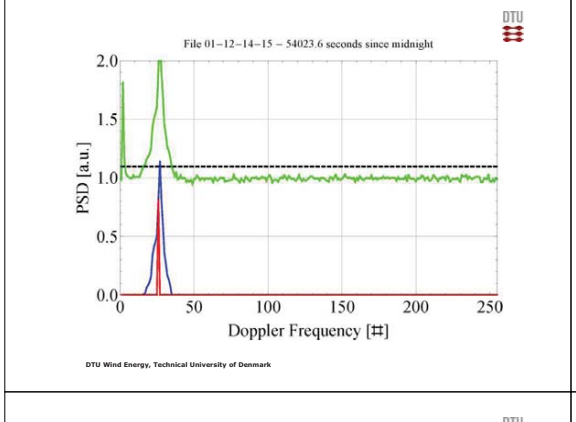
DTU
File 01–12–14–15 – 54023.6 seconds since midnight
PSD [a.u.]
Doppler Frequency [⌗]
DTU Wind Energy, Technical University of Denmark

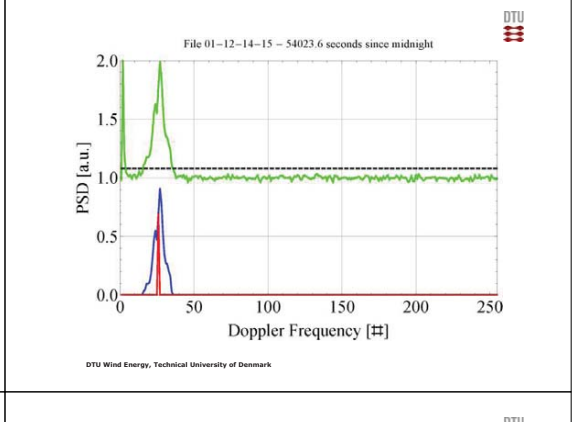
DTU
File 01–12–14–15 – 54023.6 seconds since midnight
PSD [a.u.]
Doppler Frequency [⌗]
DTU Wind Energy, Technical University of Denmark

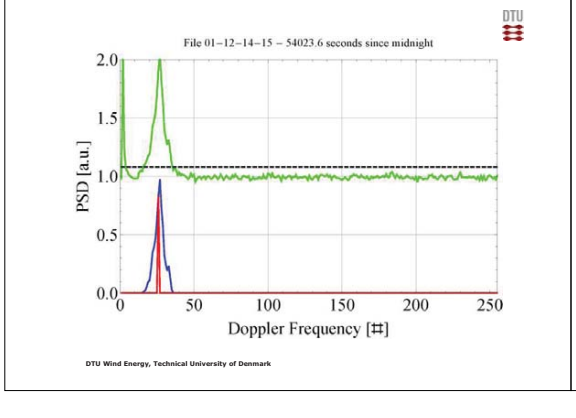
DTU
File 01–12–14–15 – 54023.6 seconds since midnight
PSD [a.u.]
Doppler Frequency [⌗]
DTU Wind Energy, Technical University of Denmark

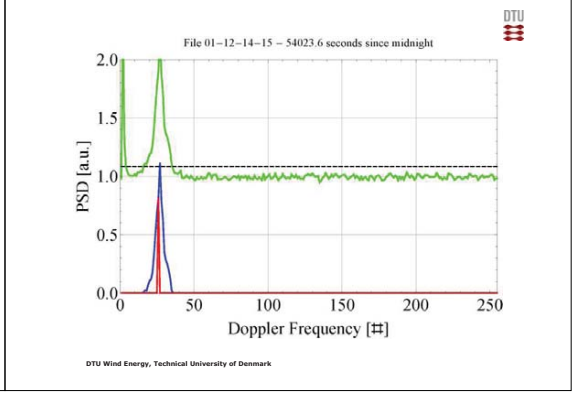
DTU
File 01–12–14–15 – 54023.6 seconds since midnight
PSD [a.u.]
Doppler Frequency [⌗]
DTU Wind Energy, Technical University of Denmark

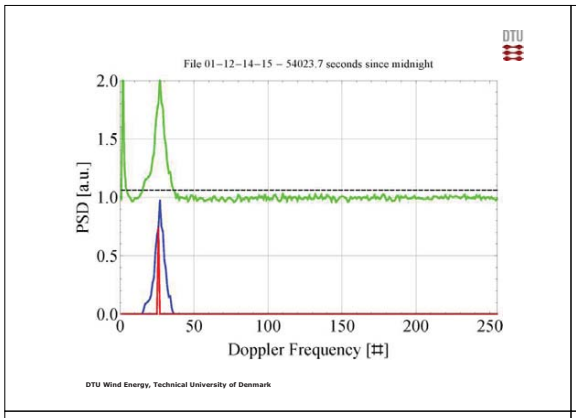
File 01–12–14–15 – 54023.7 seconds since midnight
PSD [a.u.]
Doppler Frequency [#]
DTU Wind Energy, Technical University of Denmark

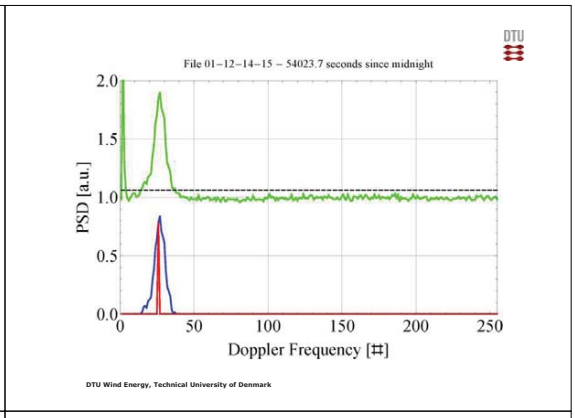
File 01–12–14–15 – 54023.7 seconds since midnight
PSD [a.u.]
Doppler Frequency [#]
DTU Wind Energy, Technical University of Denmark

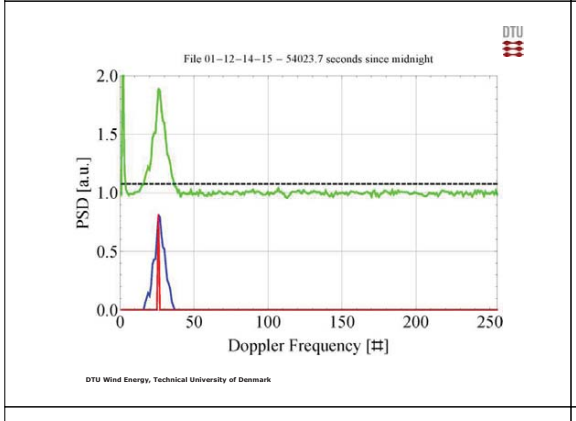
File 01–12–14–15 – 54023.7 seconds since midnight
PSD [a.u.]
Doppler Frequency [#]
DTU Wind Energy, Technical University of Denmark

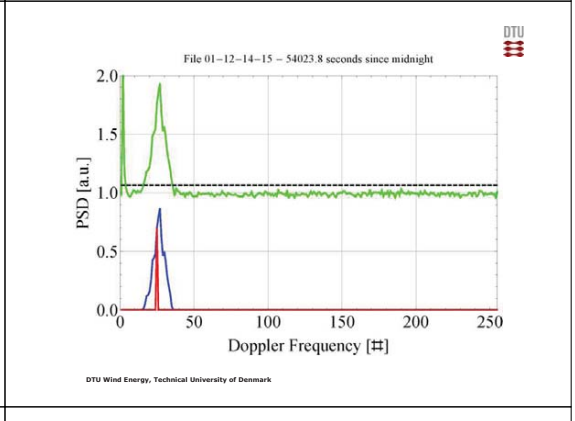
File 01–12–14–15 – 54023.8 seconds since midnight
PSD [a.u.]
Doppler Frequency [#]
DTU Wind Energy, Technical University of Denmark

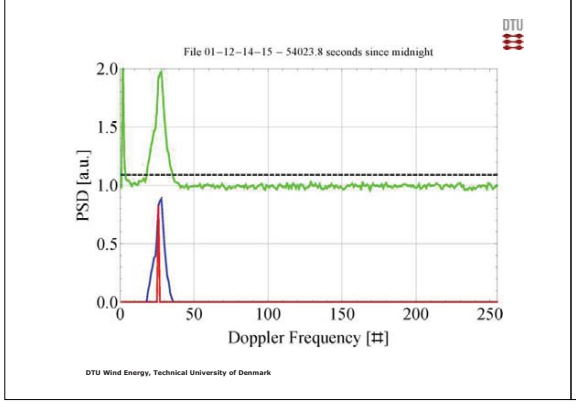
File 01–12–14–15 – 54023.8 seconds since midnight
PSD [a.u.]
Doppler Frequency [#]
DTU Wind Energy, Technical University of Denmark

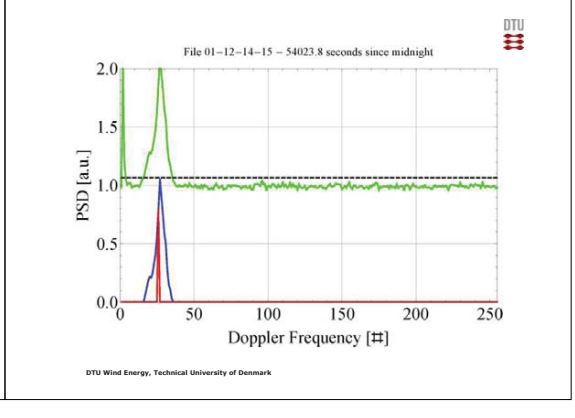
File 01–12–14–15 – 54023.8 seconds since midnight
PSD [a.u.]
Doppler Frequency [#]
DTU Wind Energy, Technical University of Denmark

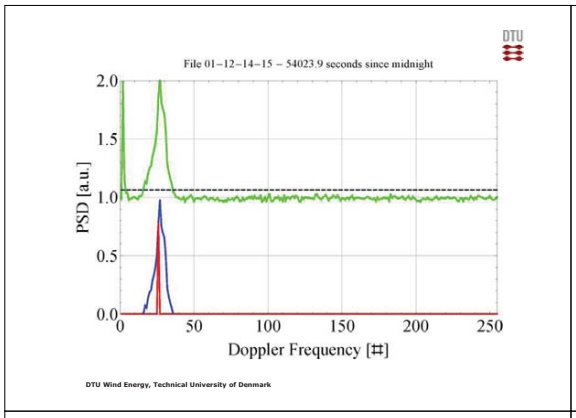
File 01–12–14–15 – 54023.9 seconds since midnight
PSD [a.u.]
Doppler Frequency [#]
DTU Wind Energy, Technical University of Denmark

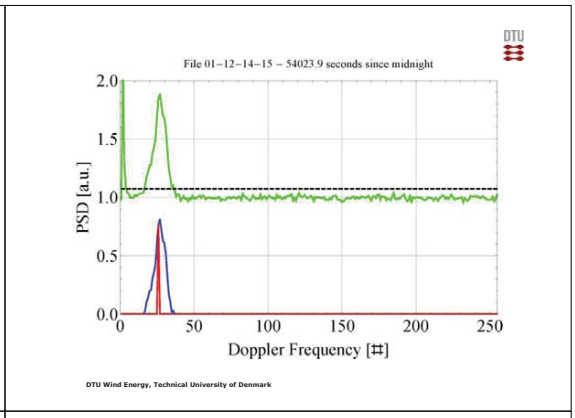
File 01–12–14–15 – 54023.9 seconds since midnight
PSD [a.u.]
Doppler Frequency [#]
DTU Wind Energy, Technical University of Denmark

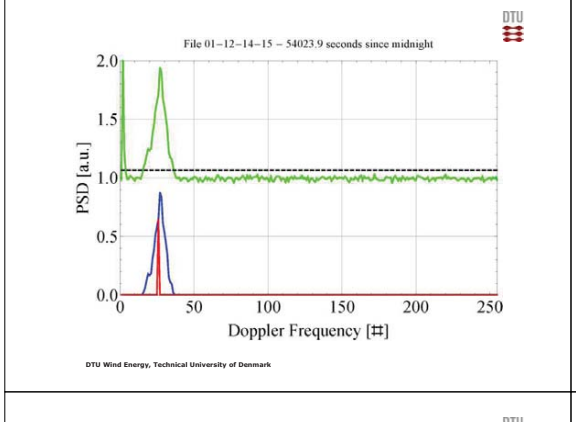
File 01–12–14–15 – 54023.9 seconds since midnight
PSD [a.u.]
Doppler Frequency [#]
DTU Wind Energy, Technical University of Denmark

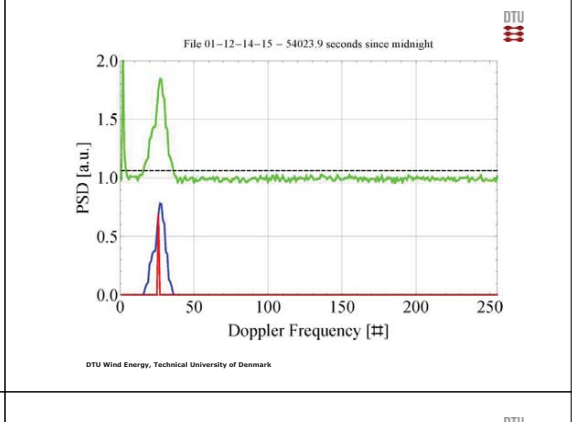
File 01–12–14–15 – 54023.9 seconds since midnight
PSD [a.u.]
Doppler Frequency [#]
DTU Wind Energy, Technical University of Denmark

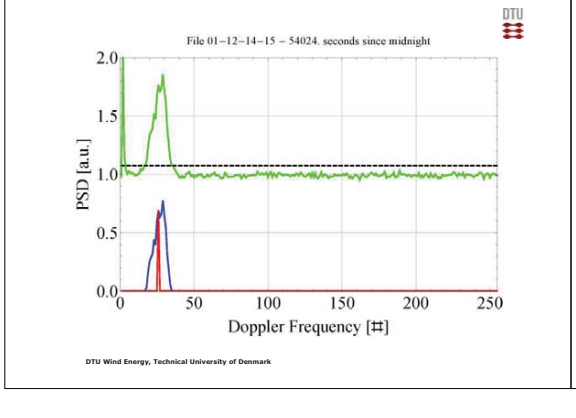
File 01–12–14–15 – 54024. seconds since midnight
PSD [a.u.]
Doppler Frequency [#]
DTU Wind Energy, Technical University of Denmark

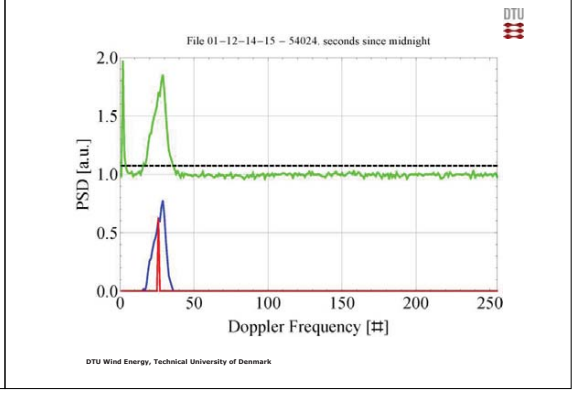
File 01–12–14–15 – 54024. seconds since midnight
PSD [a.u.]
Doppler Frequency [#]
DTU Wind Energy, Technical University of Denmark

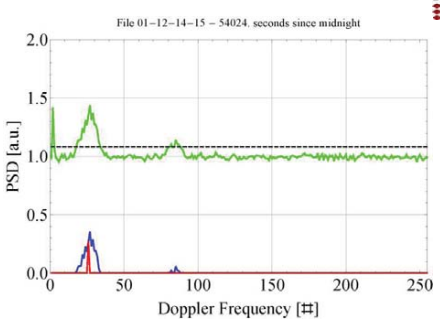

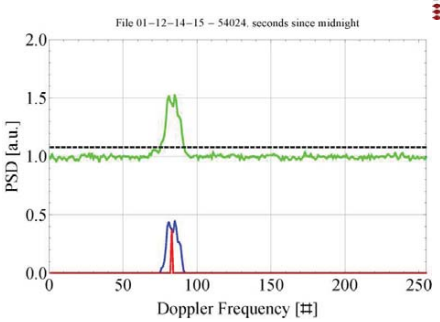

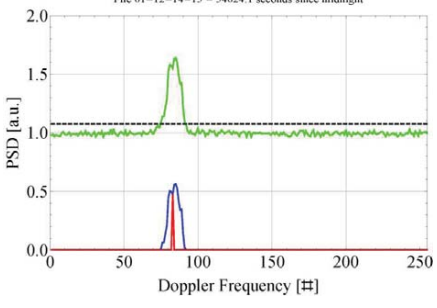

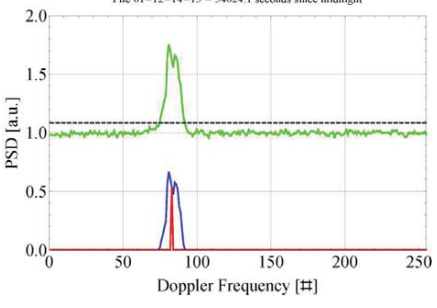

The influence from humidity

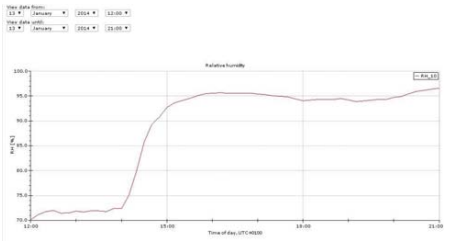

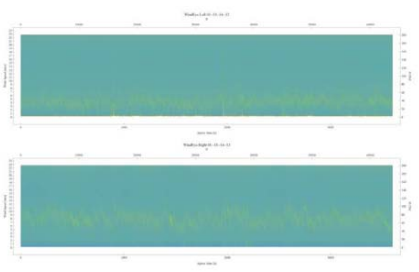

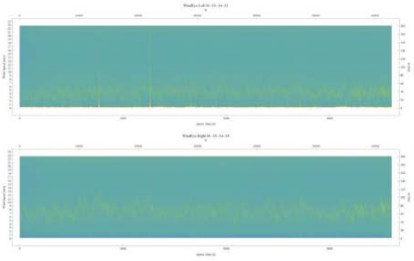

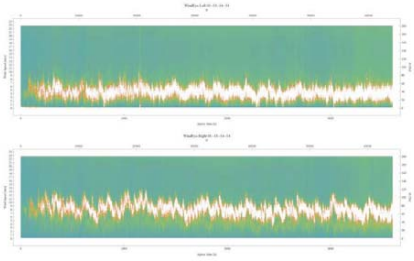

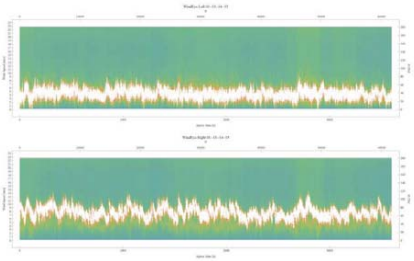

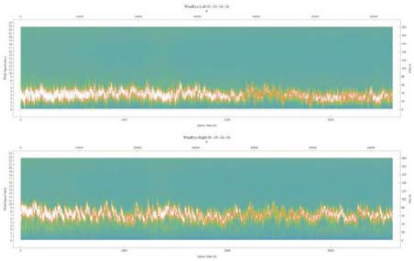

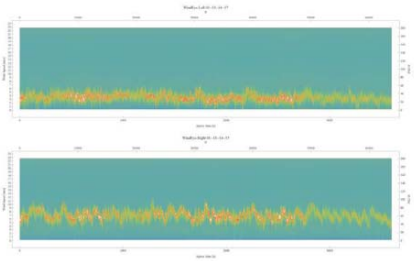

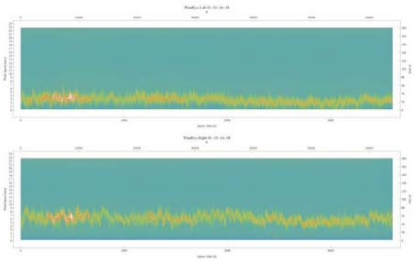

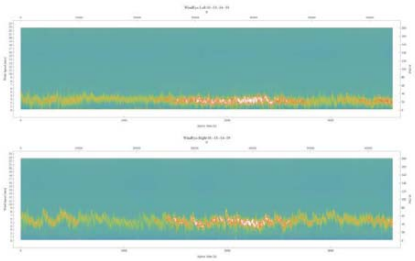

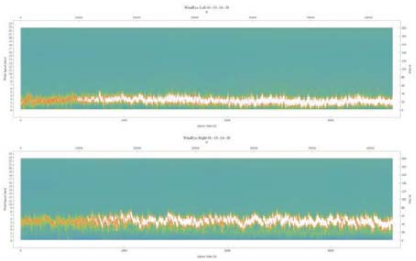

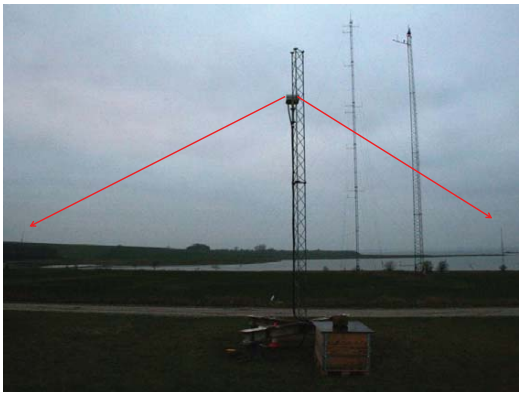

Waiting for the wind

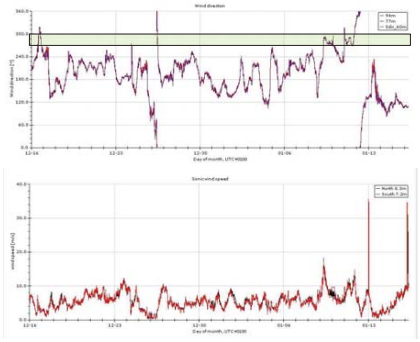

Line-of-sight speed comparison with sonic

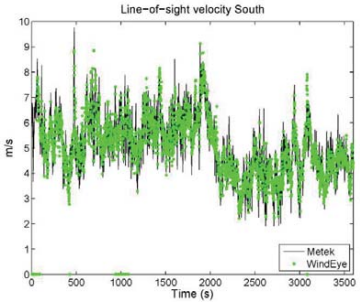

Line-of-sight speed comparison with sonic

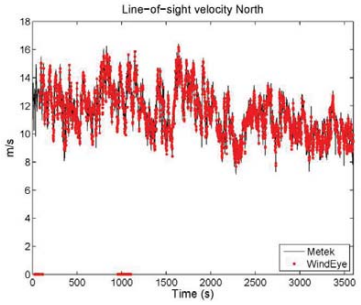

Line-of-sight speed comparison with sonic

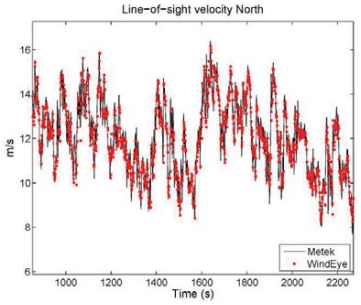

Line-of-sight speed comparison with sonic

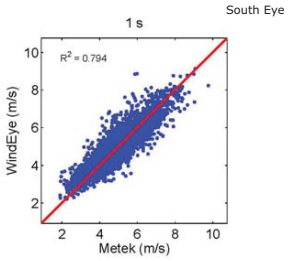

Line-of-sight speed comparison with sonic

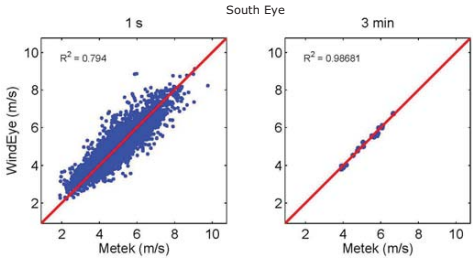

Line-of-sight speed comparison with sonic

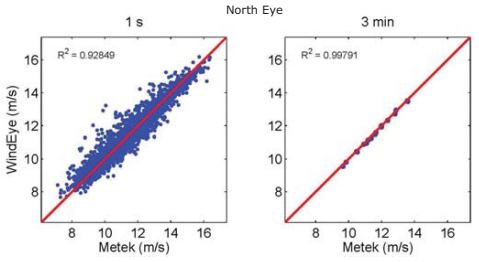

Lidar direction compared with sonic directions

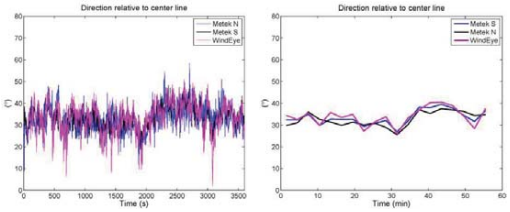

Lidar direction compared with sonic directions

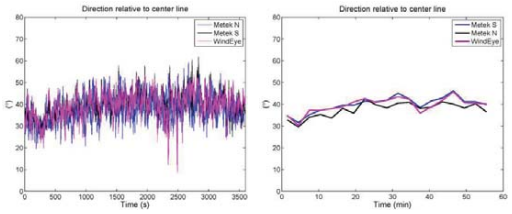

A few of the current WindEye installations

Courtesy Jørgen Korsgaard Jensen, Windar Photonics